Effects of light soaking on the performance and stability of a-Si:H thin-film solar cells

Shriram Muthaiyan Karthikeyen

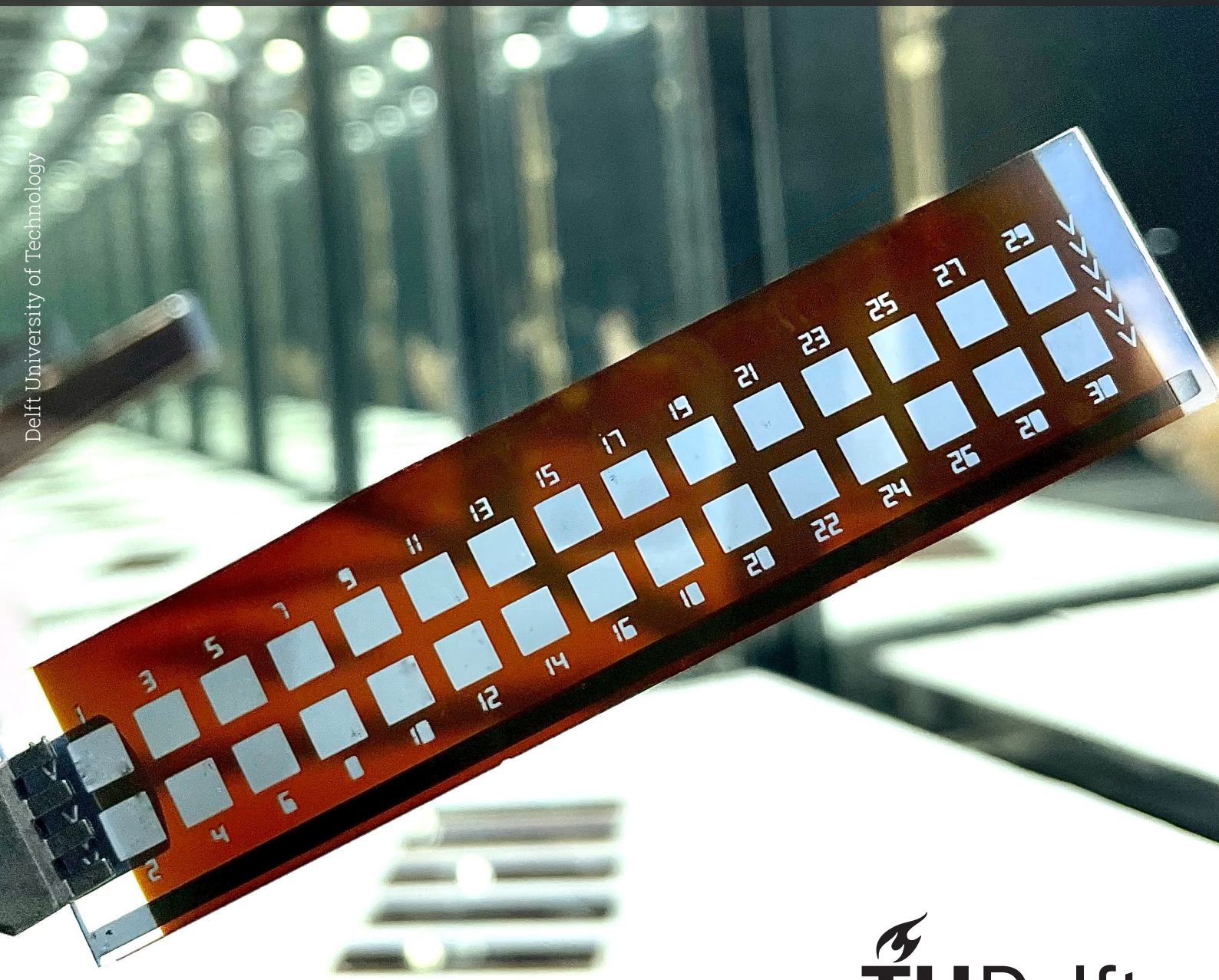

Delft University of Technology

TU Delft

Effects of light soaking on the performance and stability of a-Si:H thin-film solar cells

by

Shriram Muthaiyan Karthikeyen

to obtain the degree of Master of Science
at the Delft University of Technology,
to be defended publicly on Wednesday 16 August, 2023 at 10:30 am.

Student number: 5278635
Project duration: November 2022 – August 2023
Thesis committee:

Prof. dr. ir. Arno Smets,	TU Delft, ESE-PVMD, Supervisor
Dr. ir. René van Swaaij,	TU Delft, ESE-PVMD
Dr. ir. Jianning Dong,	TU Delft, ESE-DCES
Dr. ir. Sreejith Koorthedath Pullayikody,	TU Delft, ESE-PVMD
Ir. Govind Padmakumar,	TU Delft, ESE-PVMD, Daily supervisor

Cover: Photo by author

TU Delft PVMD Delft University of Technology HyET Solar Flexible light weight solar modules EKL Else Kooi Laboratory

Acknowledgement

This thesis marks the end of a beautiful and unforgettable roller coaster ride that I experienced as a masters student at TU Delft. Over the last 2 years, I have gained a lot of knowledge that has helped me grow academically and personally. Words cannot completely express my gratitude to god, the almighty, for showering all the blessings, opportunities, strength and knowledge throughout my life. I would like to take this opportunity to express my deepest gratitude to my family for the love and immense support without which nothing would have been possible. In addition, I want to thank a lot more people who supported me in my journey.

Professor Arno Smets, I am extremely grateful that you were my thesis supervisor. More than a supervisor, you have also been a true inspiration to me. Your passion for solar energy is absolutely astounding, and I truly admire you for the knowledge you possess and your optimistic attitude towards anything. I thoroughly enjoyed our meetings and discussions throughout my thesis and thank you so much for such a wonderful experience.

Govind Padmakumar, I could not have imagined a better daily supervisor than you. I thank you from the bottom of my heart for all your guidance throughout my thesis. I truly enjoyed all the conversations we have had so far and I have certainly learnt a lot from you. I really appreciate you for being so kind and approachable and thank you yet again for your support and encouragement.

I sincerely thank Sreejith for his valuable suggestions and support during my thesis. I would also like to express my gratitude to Paula and Gianluca for their guidance and constructive feedback along the way. Special thanks to Stefaan and Tim for the support they provided at the ESP lab. Furthermore, I would like to thank the HyET Solar team and PVMD research group for all the informative meetings and the EKL team for the lab assistance and maintenance.

Last but not least, I would like to express my heartfelt thanks to all my dear friends, who I consider to be my second family, for the countless memories we have shared over the past two years. In particular, I want to thank Surya, Kartik, Raghav and Sultan for always being there for me. At the same time, I am pleased and grateful for the amazing friends I have made during my thesis period. I specifically want to thank Shloka, Mehdi, Tristan, Matthias, and Mathijs for all the fun filled nerdy lunch breaks, free-coffee breaks, enjoyable parties and hangouts that made my time with everyone of them so memorable.

Shriram Muthaiyan Karthikeyen
Delft, August 2023

Abstract

Thin-film silicon photovoltaic (PV) technology has an enormous potential in the solar power market due to its light weight, flexibility and ease of integration. This enables it to have a wide range of applications like roof top and building integrated installations making it more sustainable. Some of the other key benefits of thin-film silicon PV technology include energy efficient production, less material usage, low temperature coefficient and low manufacturing cost. The relatively low conversion efficiency, however, is the major drawback of thin film silicon solar cells.

Hydrogenated amorphous silicon (a-Si:H) grown by plasma-enhanced chemical vapor deposition (PECVD) is one of the extensively employed light absorbers in thin-film silicon solar cells. However, light-induced degradation (LID) of a-Si:H is one of the biggest limiting factors of this technology. LID is a metastable defect creation phenomenon that decreases the conversion efficiency of the a-Si:H solar cell after prolonged exposure to light. This is known as the Staebler-Wronski effect (SWE). SWE has been a subject of research over the past 4 decades. Despite tremendous efforts, the complete suppression of the LID has not been demonstrated yet. Nevertheless, there has been a great progress in characterisation of the defect creation and also the optimisation of solar cells to minimise the effect of LID.

In this thesis, LID of three single junction a-Si:H thin film solar cells with different qualities of a-Si:H absorber layer namely high bandgap a-Si:H, low bandgap a-Si:H and high/low bandgap a-Si:H are studied. Light soaking experiments were carried out for several hundred hours and the performance of the solar cells was analysed through external quantum efficiency (EQE) and illuminated JV characterisations at regular time intervals. Some of the key findings of the experiments include severe LID of high bandgap a-Si:H absorber layer due to increased defect creation, enhanced recombination at the p/i interface in all of the devices and also a significant relationship between the performance and light soaking temperature. Furthermore, the thermal annealing study revealed that, maximum recovery of the performance parameters can be observed at an annealing temperature of 180 $^{\circ}$C.

Based on the findings of the above mentioned study, additional experiments were carried out to investigate the stability of the devices with different materials as a buffer layer at the p/i interface. The results of the experiments revealed the significance of the buffer layer in the performance of the devices and also its influence on the LID. In addition, the analysis suggests that intrinsic silicon oxide (i-SiO$_X$), intrinsic hydrogenated amorphous silicon (i-a-Si:H), and p-doped hydrogenated amorphous silicon (p-aSi:H) are some of the potential candidates for a buffer layer in an a-Si:H solar cell that could give an improved stabilised performance. Furthermore, the speculation of light induced boron diffusion into the a-Si:H bulk through the buffer layer was tested by another light soaking study to investigate effects of window layer (p) doping on LID. The study found no correlation between the window layer doping and the p/i interface degradation indicating the possibility of a different defect creation mechanism responsible for the enhanced recombination at the p/i interface.

Contents

List of Figures

List of Tables

1 Introduction

It is a widely recognised fact that solar energy, one of the most promising and cleanest types of renewable energy, has experienced exponential expansion in recent decades (2000-2022) and is becoming an established source of electricity [1]. This is mainly harvested using photovoltaic (PV) cells/modules which can be manufactured from a variety of materials. Silicon (Si) being one of the most abundant semiconductor materials on earth, poses a major advantage over other rare earth elements because of its non-toxic nature, which is of utmost importance for sustainable, large scale PV applications and thus being widely used as an absorber material in most of the PV technologies.

1.1. Why thin-film solar cells?

There are two major classifications of PV cell technology—wafer based and thin film that control the global market and each of these classifications consist of several types of PV technologies. Due to high cost, higher efficiency PV technologies like gallium arsenide (GaAs) and multi-junction cells are less popular but perfect for use in space applications and concentrated solar systems. A variety of new PV technologies are also being developed, including perovskite cells, organic solar cells, dye-sensitized solar cells, and quantum dots which are still in their laboratory research stage [2].

Crystalline Silicon (c-Si, first generation PV) solar cells are obtained from thin slices of silicon (wafers) 160–240 µm thick, cut from a single crystal or a block. The type of crystalline cell produced depends on the silicon wafer manufacturing process. The main types of crystalline cells are monocrystalline, polycrystalline or multicrystalline [3]. Being the leader of the PV market for more than 30 years, crystalline silicon PV technology has several advantages over many other technologies like high efficiency (around 22% considering the interdigitated back contact (IBC) technology [4]), longer life span (25 years), non toxic and minimal power losses [5]. However, it also faces some disadvantages like high cost, high temperature coefficient, inflexible structure, poor low light performance.

Thin film solar cell which is the second generation PV technology is made by depositing single or multiple thin layers of PV elements on a glass, plastic, or metal substrate. The film's thickness can range from a few nanometers to tens of micrometers, making it noticeably thinner than its rival, the conventional first-generation c-Si solar cell (which uses wafers that are around 160-240 µm thick) [6]. The three most extensively used thin film solar cells are amorphous silicon (a-Si), cadmium telluride (CdTe), and copper indium gallium selenide (CIGS). All three materials have a direct bandgap, which makes it possible to make very thin films [7]. Among all the thin-film solar cell technologies, the a-Si:H-based cell has high potential as it can be produced on a megawatt scale. It has the advantage of a straightforward and standard manufacturing method for integrated modules on rigid and flexible substrates, despite limited production throughput, low efficiency, stability issues, and costs comparable to crystalline silicon cells [8].

Thin film PV being an emerging technology has several advantages like lower thermal losses at extreme temperatures due to the low-temperature coefficient, high efficiency for most technologies (CdTe, CIGS, and especially GaAs), flexibility and ideal for portable and building integrated photovoltaics (BIPV) applications, cost effective in terms of less material requirement to create PV modules and most importantly much lighter in weight than c-Si PV technology [9].

Even though crystalline silicon solar technology is more widely used, thin-film solar technology has a very bright future. BIPV applications, portable modules, and even high-efficiency space applications with CIGS and GaAs PV modules are now possible [9]. Thin-film technology is still a worthwhile alternative to take into consideration, even if c-Si technology is likely to continue having the highest market share due to its present high rated efficiency, low manufacturing prices, and other benefits. Overall, increasing applications in harsh environments, diffuse lighting, and high temperatures will enable thin film solar cells to thrive in the next decades, despite their declining market share [7].

1.2. Working principle and record devices

1.2.1. Working principle of a solar cell

The photovoltaic effect, or the generation of a potential difference at the junction of two distinct materials in response to electromagnetic radiation, is the basis for the operation of any type of solar cell. The photoelectric effect, in which electrons are released from a material after it has absorbed light with a frequency above a material-dependent threshold frequency, is closely connected to the photovoltaic effect. In 1905, Albert Einstein understood that this effect can be explained by assuming that the light consists of well defined energy quanta, called photons. The energy of such a photon is given by

$$E = h\nu \tag{1.1}$$

where h is Planck's constant and ν is the frequency of the light. The photovoltaic effect can be divided into three basic processes namely

1. Generation of charge carriers due to the absorption of photons in the materials that form a junction.
2. Subsequent separation of the photo-generated charge carriers in the junction.
3. Collection of the photo-generated charge carriers at the terminals of the junction.

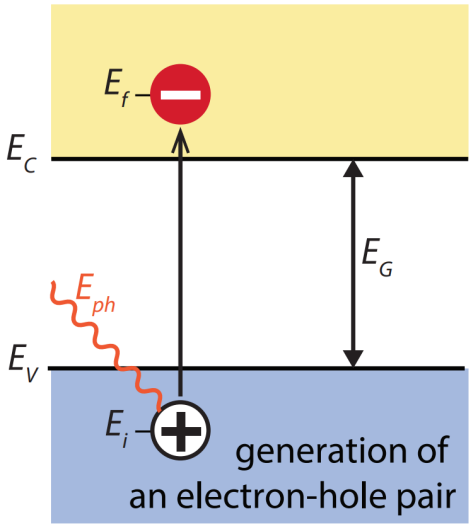

Figure 1.1: Illustration of the absorption of a photon in a semiconductor with bandgap E_G [10]

When a photon is absorbed by a material, its energy is used to excite an electron from a lower energy level E_i to a higher energy level E_f, as shown in figure 1.1. Photons can only be absorbed when the

electron energy levels E_i and E_f are such that their difference, hν = E_f - E_i, equals the photon energy. In an ideal semiconductor, electrons can occupy energy levels above the conduction band edge (E_C) and below the so-called valence band edge (E_V). No allowed energy states that could contain electrons exist between those two bands. As a result, this energy disparity is known as the bandgap (BG), or E_G = E_C - E_V. A photon that has less energy than (E_G) will not be absorbed but will instead pass through an ideal semiconductor unaffected. The creation of a void at E_i occurs when an electron is excited from E_i to E_f. This void, which is also known as a hole, functions like a particle with a positive elementary charge. Thus, as shown in figure 1.2, an electron-hole pair is produced as a result of photon absorption. The photon's radiative energy is transformed into the chemical energy of the electron-hole pair. Then the electron-hole pair will typically combine again, causing the electron to return to its initial energy level E_i. The energy will then either become a photon (radiative recombination) or be transferred to additional electrons, holes, or lattice vibrations (non-radiative recombination), depending on the situation. Semipermeable membranes must be present on both sides of the absorber such that only electrons can flow out through one membrane and only holes can flow out through the other membrane if one wishes to use the energy stored in the electron-hole pair for performing work in an external circuit. These membranes are typically made of n- and p-type materials in solar cells. In order for the electrons and holes in a solar cell to reach the membranes before they recombine, the time it takes for the charge carriers to reach must be shorter than the lifetime of the charge carriers. This requirement caps the absorber's thickness. Finally, electrical contacts are used to extract the charge carriers from the solar cells through an external circuit. The electron hole pair's chemical energy is ultimately transformed into electric energy. At a metal-absorber interface, as shown in figure 1.2, the electrons will combine with holes once they have completed the circuit.

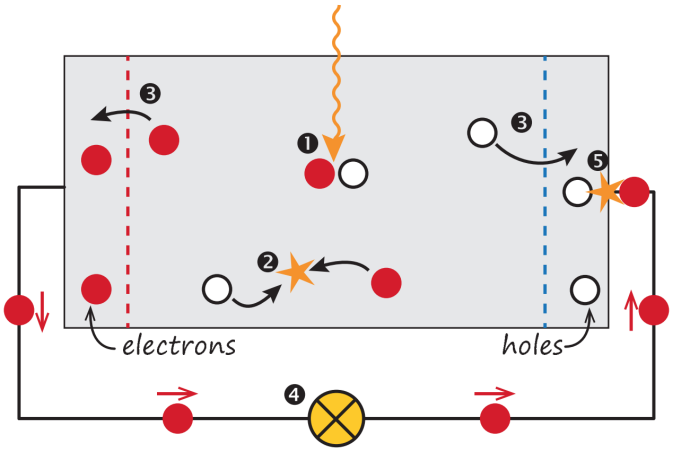

Figure 1.2: A very simple solar cell model representing the generation, separation and collection of the electron-hole pairs [10]

As the working principle of a solar cell is described, further information on the solar cells that are studied in this thesis are now briefly explained. This thesis focuses on the experimental studies made on thin film silicon solar cells consisting of hydrogenated amorphous silicon (a-Si:H) absorber layer. These solar cells are fabricated by depositing thin films on glass or metal substrates using layer by layer deposition. The layers are generally categorised as p-doped layer (p) where the majority carriers are holes, intrinsic layer (i) which is the absorber layer and n-doped layer (n) where the majority carriers are electrons. There are two types of device configurations, superstrate and substrate. In the "superstrate" configuration, the thin films are deposited in the p-i-n sequence onto a transparent material like glass. While the "substrate" configuration can be grown on any type of substrates that could be rigid glass or flexible metal or polymer foil. It bears a reverse, n-i-p, configuration. A transparent conductive oxide (TCO) layer is deposited for better transmission of light and high electrical conductivity, at the top where light enters the device. In addition, the front and back contact layers which are made of highly conductive metals like aluminium and silver are deposited for charge carrier collection at the terminals (refer chapter 2 and 3 for detailed explanations). Finally, the performance of a fully fabricated solar cell is determined based on the external parameters such as open circuit voltage (V_{oc}), short circuit current density (J_{sc}), fill factor (FF) and conversion efficiency (η).

1.2.2. Record devices

Since the invention of thin-film silicon solar cells, development has progressed very well over the years. Having said that, the evolution of technology can be seen in the efficiencies achieved. Some of the state of the art thin film photovoltaic devices with record performance are summarised and tabulated below.

Table 1.1: Summary of state of the art thin film silicon solar cells with record performance

Single junction a-Si:H devices						
Company/Institute	**Year**	**Device configuration**	**Stabilized efficiency (%)**	**V_{oc} (V)**	**J_{sc} (mA/cm^2)**	**FF (%)**
Julich, Germany [11]	2015	Superstrate p-i-n	10.26	0.891	17.2	67
AIST, Japan [12]	2015	Superstrate p-i-n, Triode PECVD	10.22	0.896	16.34	69.8
Mutijunction (micromorph tandem) a-Si:H/nc-Si:H devices						
Company/Institute	**Year**	**Device configuration**	**Stabilized efficiency (%)**	**V_{oc} (V)**	**J_{sc} (mA/cm^2)**	**FF (%)**
TEL Solar AG, Switzerland [13]	2016	Superstrate p-i-n	12.34	1.443	13.75	74
AIST, Japan [12]	2015	Superstrate p-i-n, Triode PECVD	12.69	1.342	13.45	70
TU Delft, Netherlands [14]	2015	Superstrate p-i-n	12.5	1.377	13.9	65

1.3. TU Delft-HyET Solar partnership

High yield Energy Technologies (HyET) Solar is a thin film solar cell company that manufactures industrial scale flexible light weight silicon solar modules which are called the Powerfoils. Powerfoil is a novel thin-film photovoltaic (Thin-Film PV) solar device based on active silicon layers that are both amorphous and micro-crystalline (a-Si/μc-Si), enclosed in widely available, reasonably priced polymer sheets to create a foil that is 0.5 mm thick. This is made by a roll to roll production process which can make up to 30 metre long modules. Powerfoil technology's distinctive characteristics enable applications in both large volume and high value markets, such as solar farms and building integrated PV. Some of its benefits include, inexpensive PV modules, low balance of system cost, high energy yield, maximum coverage of PV modules, enables vertical surfaces, easy-to-clean surface and low maintenance [15].

TU Delft signed a research contract with HyET Solar in 2022 to speed up the introduction of the next generation of solar foil by bringing this vision of the future a significant step closer. This enables the laboratory scale research conducted at TU Delft to quickly reflect on an industrial scale module. The results and the design rules of laboratory scale cells are used to optimise the industrial modules of HyET for an improved performance. This thesis is a part of such an ongoing research towards producing reliable and high efficiency solar cells.

1.4. Research questions

Over the past 4 decades, there has been a lot of improvement and evolution in the amorphpous silicon based thin film solar cell technology in terms of material quality, device architecture and the deposition conditions and techniques. Despite such a great progress, the Staebler Wronski Effect (SWE) has always been an unavoidable hindrance when it comes to improving the performance. The SWE also frequently referred as the light induced degradation (LID) is the decrease in efficiency of the amorphous silicon based solar cells when exposed to light for about 1000 hours after which the efficiency stabilises (refer chapter 3 for detailed explanations). Though this cannot be completely eliminated, the degradation can be mitigated by optimising the device architecture, deposition conditions and materials in order to have an improved stabilised performance. In simple words, there is always room for improvement.

This thesis is a small contribution towards the ongoing research of fabricating a tandem/multi-junction thin film solar cell with record performance. The ultimate purpose of this thesis is to define the design rules of the top cell (a-Si:H) of a tandem device on glass with p-i-n superstrate configuration for improved performance. In order to do so, the stability of a-Si:H has to be studied based on light induced degradation experiments. Lab scale samples of single junction a-Si:H thin film solar cells were fabricated to perform the experiments.

This thesis will answer the following research questions:

1. How does light soaking affect the performance and stability of solar cells with different qualities of a-Si:H absorber layer?
2. To what extent can thermal annealing recover the performance of degraded solar cells with different qualities of a-Si:H absorber layer?
3. What is the significance of buffer layer at the p/i interface and how does it affect the performance and stability of a-Si:H solar cells?
4. Is there a relationship between LID and the window layer doping concentration?

1.5. Thesis outline

This thesis consists of 5 chapters. While this section marks the end of the introductory chapter, the reader will be presented with chapter 2 which gives theoretical information about hydrogenated amorphous silicon and its applications in solar cells which forms the foundation of this thesis. Furthermore, the deposition methods and characterisation techniques used in this thesis are also described in chapter 2. In chapter 3, the reader is introduced to light induced degradation with a background study followed by the methodology employed along with a detailed interpretation of results with some key conclusions which answers the first two research questions of this thesis. Chapter 4 begins with the background study based on one of the conclusions of chapter 3. The experimental procedures are then elaborated followed by another detailed interpretation of the results with some key conclusions to answer the last two research questions of this thesis. Finally, all the key conclusions are drawn in chapter 5 along with recommendations for further research.

2

Fundamentals

This chapter elucidates the core theoretical background of this thesis supported by a literature review. Firstly, the properties of a-Si:H is explained. Secondly, the a-Si:H based devices are described along with illustrations of device architecture. Thirdly, the deposition methods used to fabricate a solar cell are described with schematic diagrams. Finally, the characterisation techniques are explained. It is to be noted that the theoretical explanations in the following subsections are derived from the solar energy book [10] unless stated otherwise.

2.1. Hydrogenated amorphous silicon

Hydrogenated amorphous silicon has played a crucial role for decades already as intrinsic absorber layer with doped layers to build PIN junctions, and to an increasingly important extent in combination with crystalline silicon wafers in heterojunction solar cells [16]. In order to understand design and operation of an a-Si:H solar cell, which is different from a crystalline silicon (c-Si) cell, the material properties of a-Si:H are summarised and compared to the single crystal silicon.

2.1.1. Atomic structure

The atomic structure of a-Si:H can be better understood by considering the crystalline silicon structure. Figure 2.1(a) illustrates the schematic atomic structure of single crystal silicon. The angles between bonds are equal, and each bond has the same length. The coordination number or coordination refers to the total number of bonds that an atom in an atomic structure has with its near neighbors. As a result, all of the Si atoms in single crystal silicon have a coordination number of four, or are fourfold coordinated. The definition of a unit cell allows for the replication of the crystal lattice by making replicas of the unit cell and stacking them next to one another. A structure with long range order is what is used to characterize such a regular atomic arrangement. The actual lattice structure of a single crystal of silicon is represented by a diamond lattice unit cell.

On the contrary, Figure 2.1(b) illustrates the atomic structure of a-Si:H which does not exhibit the structural order over a long range as is the case for single crystal silicon. On a local atomic scale, however, there is a similarity in atomic configuration since most Si atoms have covalent bonds with four of their neighbors. The single crystal silicon shares the same short-range order as the a-Si:H, but the long-range order is absent. On a scale greater than a few atomic distances, the slight variations in bonding angles and lengths between the nearby atoms in a-Si:H result in the complete loss of the locally ordered structure. The resulting atomic structure of a-Si:H is called the continuous random network (CRN). The typical semiconductor concept of the energy state bands, represented by the conduction and valence bands, can still be used because of the short-range order in the CRN of a-Si:H.

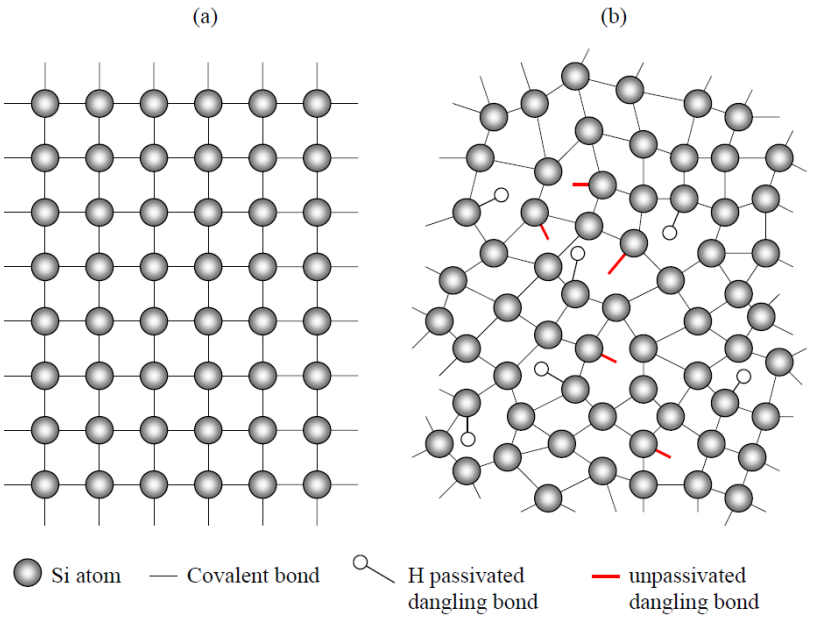

Figure 2.1: Atomic structure of (a) crystalline silicon and (b) hydrogenated amorphous silicon [17]

The wider variations in bonding angles and lengths between the neighboring atoms of a-Si:H result in the so-called weak or strained bonds. In an ideal single crystal silicon, the energy of the covalent bonds is lower than the energy of the weak bonds. As a result, the atomic network can readily develop defects due to the weak bonds. We observe that the concept of a defect is altered with respect to the crystal structure in the CRN. Any atom in a crystal lattice that is out of place creates a defect. An atom cannot be out of place in the continuously random network. A defect in a-Si:H is a coordination defect since an atom's coordination to its neighbors is the only distinct structural trait in a CRN. This occurs when an atom has an excessive number of bonds or too few. The defects in a-Si:H are primarily represented by Si atoms that are covalently connected to just three other Si atoms (threefold coordinated) and have one unpaired electron, known as a "dangling bond (DB)". The defects in a-Si:H are frequently linked to the DBs since this configuration is the predominant defect in a-Si:H.

When amorphous silicon is deposited in such a way that hydrogen can be incorporated in the network (as in the case of glow discharge deposition from silane), then the hydrogen atoms bond with most of the DBs. We say that the DBs are passivated by hydrogen. Hydrogen passivation reduces the dangling bond density from about 10^{21} cm^{-3} in pure a-Si (amorphous silicon that contains no hydrogen) to 10^{15}-10^{16} cm^{-3} in a-Si:H, i.e. less than one dangling bond per million Si atoms. In Figure 2.1(b) some of the defects with unpassivated DBs and with hydrogen passivated DBs are depicted. Device quality a-Si:H contains from 1 to 10 atomic percent of hydrogen. In summary, the short range order in a-Si:H network and the hydrogen passivation of the DBs are responsible for semiconductor properties of amorphous silicon [17].

2.1.2. Hydrogen dilution

In order to passivate defects and create high quality material, hydrogen is used as an additional feed-in gas to the deposition chamber, reducing the proportion of pure silane gas as a result. The hydrogen dilution ratio R (shown in equation 2.1) is defined as the ratio of the gas flow rate of hydrogen gas to silane gas that enters the deposition chamber.

$$R = \frac{[H_2]}{[SiH_4]} \tag{2.1}$$

Higher values of R enable silicon precursors to diffuse for a longer period of time before settling in

the amorphous structure due to the increased hydrogen coverage of the growing surface that is created. As a result, there is a higher chance of forming energetically advantageous bonds, which in turn results in an interatomic network that is less prone to defects and defect creation. Enhancing defect passivation is made possible by the increased hydrogen coverage throughout the thin film deposition process, particularly in the case of DBs in the layer being grown [18].

Diluting the silane flow with hydrogen has several effects on the structure of a-Si:H. It has an impact on the density, hydrogen content, and optical band gap at moderate dilutions. Additionally, it lowers the SWE and improves the material's conductivity: Solar cells that use hydrogen dilution during the deposition of the absorber layer stabilize more quickly and at a higher normalized efficiency than other cells [19]. Microcrystalline silicon begins to form at increasing dilutions, at first as grains in the host material a-Si:H and then as full microcrystalline form. The relationship between R and film thickness is seen in Figure 2.2.

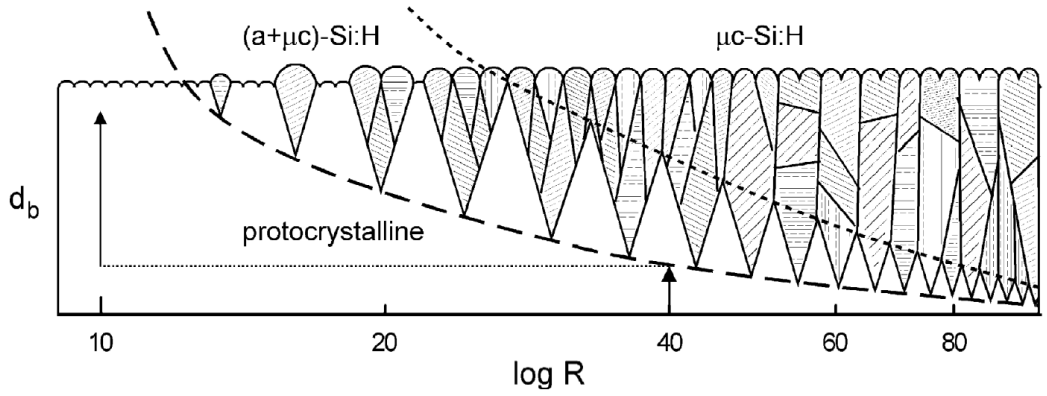

Figure 2.2: The effect of hydrogen dilution ratio (R) and layer thickness (d_b) on the Si material [20]

The substrate temperature, power, and pressure, as well as other deposition parameters like the hydrogen dilution, also affect the material properties of the deposited a-Si:H. On the one hand, hydrogen dilution typically causes a decreased deposition rate, which leads to a lower defect density, but on the other, it causes an industrially unfavorable longer deposition time [20].

2.1.3. Density of energy states

The differing distributions of permissible energy states caused by the different atomic structures between a-Si:H and single crystal silicon are schematically depicted in Figure 2.3. The single crystal silicon's periodic atomic structure produces a range of energy bands, which are the permitted energy states for electrons, and forbidden gaps, sometimes known as band gaps, are the excluded energy ranges. The distribution of the density of states (DOS) for silicon single crystals with a well-defined band gap (E_g) separating the valence band from the conduction band is shown schematically in Figure 2.3(a). The band gap of single crystal silicon is 1.12 eV at ambient temperature. There are no permitted energy levels in the band gap for a perfect crystal.

As seen in Figure 2.3(b), the density of states for a-Si:H is continuous, and there is no clearly defined band gap between the valence band and the conduction band. The energy states of the valence band and the conduction band stretch into the band gap and form regions known as band tail states as a result of the long-range order disorder in the atomic structure of a-Si:H. The energy levels of the electrons that make up the strained bonds in the a-Si:H network are represented by the band tail states. The degree of disorder in a-Si:H material is gauged by the width of the band tails. The band tails are wider when a-Si:H is more disordered.

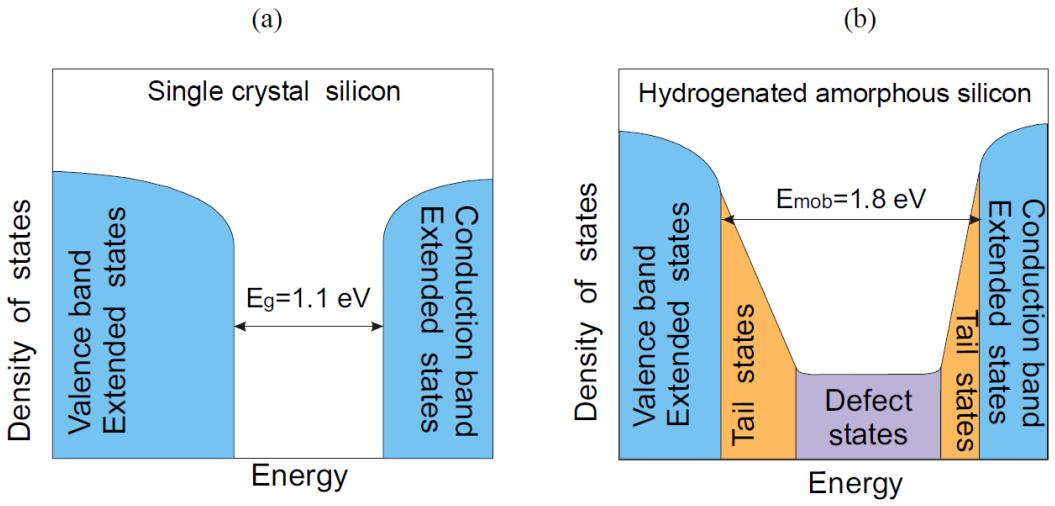

Figure 2.3: Schematic representation of the distribution of density of allowed energy states for electrons for (a) single crystal silicon (b) a-Si:H [17]

In addition, permitted energy levels in the middle region between the valence band and conduction band states are introduced by the DBs. For energy states in which the charge carriers can be thought of as free carriers, the electron and hole wave functions that cover the entire structure are typical. These states are known as extended states since they are not localized. The tail and defect states are referred to as localized states because their wave functions are localized within the structure. As a result, the mobility that distinguishes the movement of carriers through the localized states is significantly decreased. The band gap of a-Si:H is defined by the characteristic of a substantial decline in the mobility of carriers in the localized states. Because there is a significant density of states in this band gap, it is referred to as the mobility gap, or E_{mob}, which is contrary to the traditional definition of the band gap. The valence band and the conduction band mobility edges in a-Si:H are the energy levels that distinguish the extended states from the localized states.

The mobility gap of a-Si:H, which typically measures 1.8 eV, is wider than the band gap of single crystal silicon. The electrical characteristics of a-Si:H are greatly influenced by the localized tail and dangling bond states. The dangling bond states function as highly effective recombination centers and particularly influence the lifespan of the charge carriers, while the tail states operate as trapping centers and increase the space charge in a device [17].

2.1.4. Defects in a-Si:H

The defect states are depicted schematically in figure 2.3 (b) (the purple area). This section introduces the actual shape of the defect density of states which are much more complex. Shockley-Read-Hall recombination is a type of recombination that uses such defects as effective recombination centres. The number of defects directly influences the solar cell's efficiency by affecting the rate of recombination.

A defect in c-Si is defined simply as a deviation from the ideal crystal structure depicted in figure 2.3 (a). Interstitial or vacancies, point, line, and plane defects are a few examples of defects in c-Si. This definition does not apply to a-Si:H because there is no crystal structure to deviate from. It is more helpful to consider a-Si:H defects as deviations from the "ideal amorphous network," which can be imagined as a CRN with all bonds satisfied. Accordingly, all Si atoms are four-fold coordinated, while all H atoms are one-fold coordinated [20]. According to this definition, a defect must locally involve either too few or too many electrons per atom (i.e., it is a coordination defect). But the material is not adequately described from this straightforward viewpoint. Numerous models have been put forth; the following discussion will focus on two of them.

The defect-pool model

The basic principle of defect-pool model (DPM) is that isolated DBs, which are created when weak Si-Si bonds break, are the most common kind of defect. The constant forming and breaking of these bonds, which are in equilibrium, determines the density of defects. Positive (D+), neutral (D0), and negative (D-) charges are the three possible charges for DBs. When a charge carrier can be trapped, which results in a shift in the charge level, a DB acts as a defect. As a result, the electronic density of states for DB-related defects consists of two Gaussian distributions connected to the changes in charge levels (designated as E+/0 and E0/- for the changes in positive and neutral state and neutral and negative state, respectively). They are also referred to as ”defect pools” and are two Gaussian distributions that are thought to be situated on either side of Eg/2 (the midgap energy).

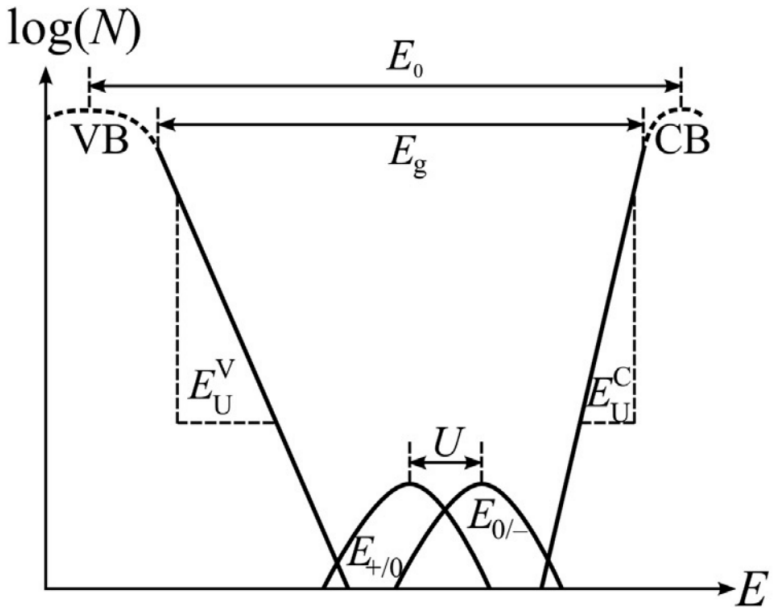

Figure 2.4: Schematic band diagram of a-Si:H in the defect pool model [16]

Disordered network with hydrogenated vacancies (DNHV)

Defects in a-Si:H have been associated with strained bonds and hydrogen that is migrating, but always from a CRN perspective on the nanostructure. However, a number of experimental findings have called into question the CRN’s accuracy in describing the nanostructure. The so-called disordered network with hydrogenated vacancies (DNHV) is an alternative to the CRN [21].

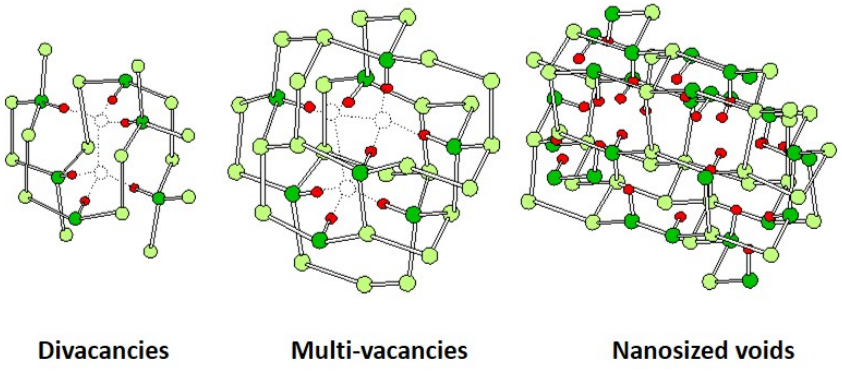

Figure 2.5: Schematic representation of the nanostructures in a-Si:H bulk [22]

Smets et al. [23] suggest a more intricate explanation for a-Si:H, in which there are other imperfections than the dangling bond that deviate from the ideal CRN. These deviations are found in a variety of hydride configurations and can be roughly classified into voids and vacancies. In the DNHV, not only the migration of hydrogen in a-Si:H can be considered, but also the migration of open volume deficiencies, such as divacancies (DVs), multivacancies (MVs), and nanosized voids (NVs), which are surrounded by disordered, CRN-like regions. Figure 2.5 shows a schematic representation of various types of nanostructures in the a-Si:H bulk. In this model, a defect is one of these entities when hydrogen hasn't completely passivated it. This suggests that additional defect distributions, beyond the two suggested by the DPM, may exist in the a-Si:H bandgap [20].

2.1.5. Absorption coefficient spectrum

The absorption coefficient α (cm^{-1}) of a material is defined as a measure for how far into a material light of a certain wavelength can penetrate before it is absorbed, or in other words, how a photon of energy E_{ph} with photon flux density ϕ decreases as a function of the incident photon flux ϕ^0 and the distance x passed in the material. This is given by the Lambert-Beer equation [24]:

$$\Phi\left(x, E_{ph}\right) = \Phi^0\left(0, E_{ph}\right) e^{-\alpha(E_{ph})x} \tag{2.2}$$

Photon energy affects the absorption coefficient. Higher energy photons typically have a higher absorption coefficient. This indicates that red light penetrates a material more deeply than blue light. The absorption coefficient spectrum of the material is the relationship between absorption coefficient and photon energy.

Figure 2.6 shows the absorption coefficient of various materials as a function of photon energy. The absorption coefficient of c-Si is shown for reference. This graph illustrates that a-Si:H absorbs nearly 100 times more solar radiation in the visible range than c-Si. Since the atomic structure of a-Si:H is disordered, it behaves like a direct gap semiconductor, there is a higher absorption. This indicates that, a-Si:H solar cells can have a thickness that is orders of magnitude less than a typical single crystal silicon cell. As a result, manufacturing a-Si:H solar cells uses significantly less material and energy [17].

Another benefit of a-Si:H is that the optical absorption can be greatly altered by alloying with germanium or carbon, while it can be only slightly altered by varying the hydrogen content. Figure 2.6 also displays the absorption coefficient of hydrogenated amorphous silicon germanium (a-SiGe:H) made at Delft University of Technology. The ability to easily alloy a-Si:H allows for the design of solar cell structures in which active layers made of a-Si:H-based materials with various absorption properties can be used [17].

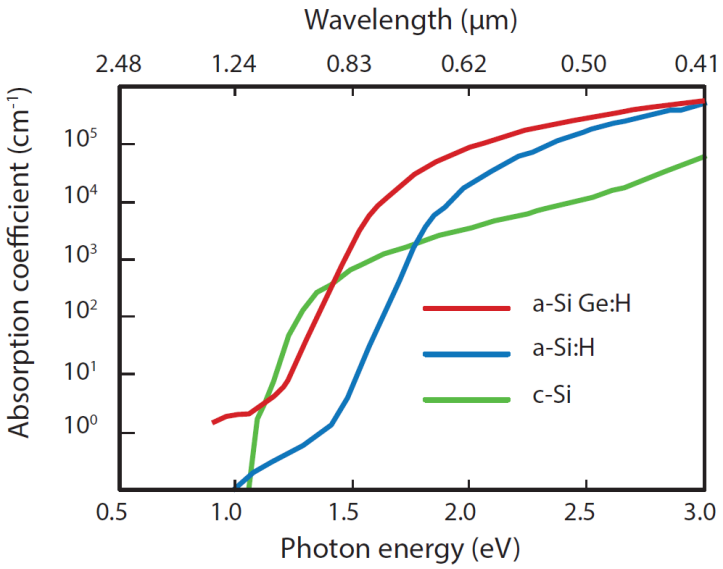

Figure 2.6: Absorption coefficient spectrum of c-Si. a-Si:H and a-Si Ge:H [25]

2.1.6. The Staebler-Wronski effect

The Staebler-Wronski effect (SWE), a novel photoelectronic phenomenon, was first described by D.L. Staebler and C.R. Wronski in 1977. Long-term (on the order of hours) exposure to light reduces the photoconductivity and dark conductivity of a-Si:H. This effect was attributed to an increase of the defect DOS or gap states that act as recombination centres for light excited charge carriers. Additionally, it has been reported that the effect lasts for a while but can be reversed by thermally annealing the material at temperatures over 150 °C [26][27]. Figure 2.7 shows the decrease in conductivity of a-Si:H film as a result of prolonged exposure to light. As a result of such a decrease in conductivity, the overall efficiency of an a-Si:H based solar cell will decrease. At standard test conditions (STC), the degradation process stabilizes after about 1000 hours of light soaking, after which the performance level of the solar cell stabilizes and stays the same for the rest of its lifetime [10].

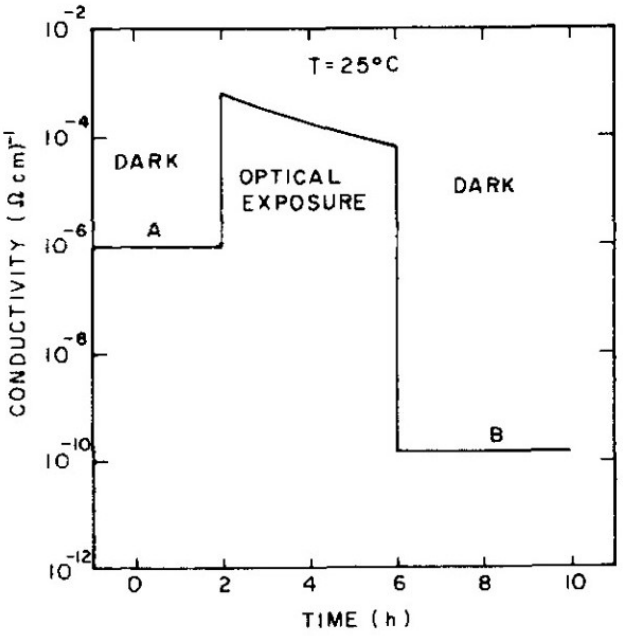

Figure 2.7: Conductivity of a-Si:H film as a function of time showing the degradation as a result of exposure to light [26]

2.2. a-Si:H based solar cells

One of the core functions of a solar cell, as discussed in chapter 1, is to separate photogenerated electron-hole pairs so that they can be collected at the terminals. When charge carriers are created in a crystalline silicon solar cell, they begin to diffuse until the minority carrier reaches the pn-junction, where the electric field causes it to move across.

As a result of the high defect content of doped a-Si:H, a pn-junction cannot be used as a practical separation device due to significantly lower diffusion lengths. A less defect-rich undoped (intrinsic) layer serves as the absorber layer in place of this. There will be a slower rate of recombination of charge carriers produced in this layer. The terminals will be difficult for them to access in the absence of an electric field, though. Thus, a p-doped and an n-doped layer is utilised on the either ends of intrinsic layer for carrier selectivity. Due to the creation of an electric field that extends throughout the entire intrinsic layer and causes the electrons and holes to drift in opposing directions, collection is made possible. Figure 2.8 shows the band diagram of a-Si:H solar cell with p-i-n configuration under open circuit condition. Although drift is the primary mechanism of carrier separation in a-Si:H solar cells, diffusion is noted to have a nonzero contribution.

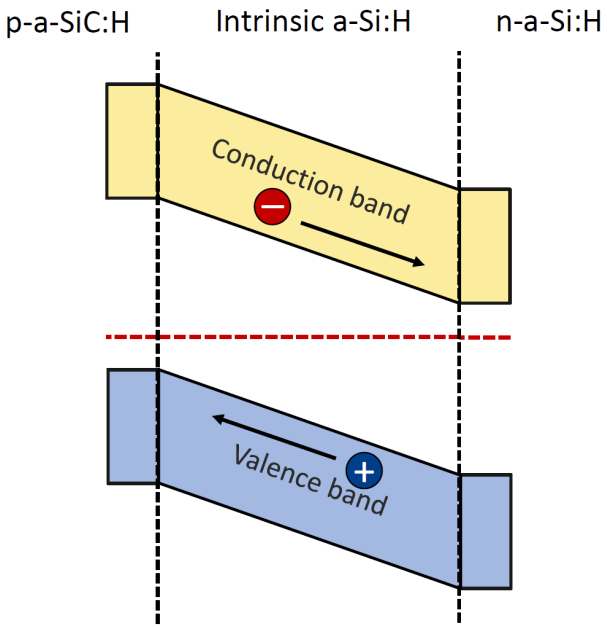

Figure 2.8: Band diagram of a-Si:H solar cell with p-i-n configuration under open circuit condition depicting the charge carrier generation through drift [28]

2.2.1. Single junction devices

An a-Si:H based solar cell with one p-i-n or n-i-p junction is called a single junction device. Figure 2.9 shows a schematic representation of the device architecture of a single junction a-Si:H solar cell. The solar cell is deposited in superstrate configuration, with glass as the superstrate.

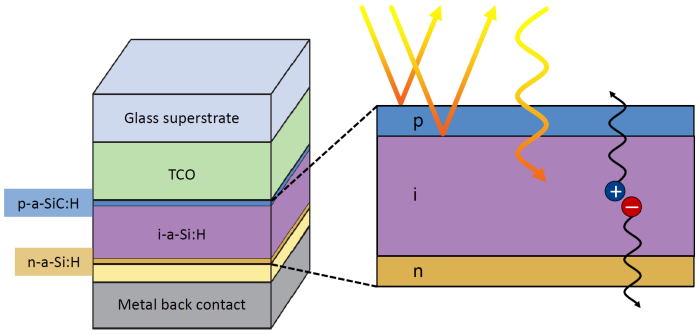

Figure 2.9: Device architecture of a-Si:H based single junction solar cell with superstrate p-i-n configuration [28]

In thin film silicon material, holes have a significantly lower mobility than electrons. Therefore, the p-layer is deposited first. In this situation, more holes can access the p-layer because the generation rate is higher close to it. To enable lateral charge carrier movement to the electrodes, a TCO layer is deposited between the p-layer and glass substrate. The intrinsic absorber layer and the thin n-doped layer are placed after the p-layer. The metal back contact is then deposited, and finally a thin zinc oxide or silicon oxide back reflector is deposited. The doped amorphous silicon layers have an extremely low diffusion length for the majority of its charge carriers due to the high defect density. As a result, unlike conventional solar cells, photogenerated charge carriers in a p-i-n cell's doped layers cannot be separated from one another and collected. As a result, since it does not aid in the creation of a current, light absorption in the doped layers is regarded as parasitic absorption. As a result, a p-i-n cell's doped layers must meet a very specific set of criteria. The reflection at the window layer interfaces should be as little as possible to maximize the amount of light reaching the absorber layer. To achieve this,

the p-doped layer's refractive index should match the geometric mean of the refractive indices of the TCO layer and i-layer. On the other hand, the n-doped layer should reflect the greatest percentage of light back into the absorber layer. To reduce the doped layer's parasitic absorption, the doped layer should, secondly, be transparent to incident light. A doped layer with a high bandgap energy that is transparent to a significant portion of the incident light could be used to achieve this. Additionally, a high bandgap energy benefits the cell's built-in potential, which influences the voltage of the cell. Lastly, the doped layer needs to be sufficiently conductive to allow charge carriers to move through the material and easily reach the electrodes. The doped layer should, in other words, have a sufficient transverse conductivity. A delicate process that has a significant impact on device performance is balancing the optical and electrical properties of the doped layers.

2.2.2. Multi-junction devices

Multi-junction devices are the solar cells that has more than one p-i-n junction. a-Si:H is commonly used in micromorph tandem (double junction) and triple junction devices. An amorphous and nanocrystalline silicon junction makes up a micromorph cell. Figure 2.10 shows a schematic representation of the device architecture and the band diagram of a micromorph tandem cell.

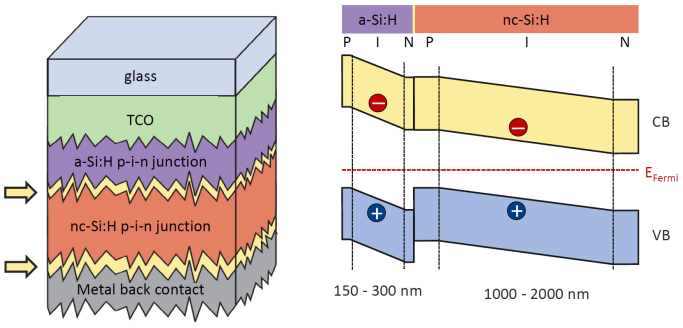

Figure 2.10: Device architecture of a-Si:H based multi-junction solar cell with superstrate p-i-n configuration [28]

Since a-Si:H has the highest bandgap energy, it is used as the top cell. The thin yellow layers represents the intermediate reflective layers (IRL). An IRL is a thin layer, placed between the top and bottom cell, that reflects a fraction of the light back into the top cell. An IRL should have high transverse conductivity, to allow charge carrier movement through the layer, and should be highly transparent to incident light, to minimize parasitic absorption. In a tandem cell, red and infrared light is absorbed by the bottom cell, while short wavelengths of blue and green light are taken up by the top cell. Both holes and electrons produced by the bottom and top cells can be collected on either side of the device. The n-layer of the top cell and the p-layer of the bottom cell must, however, form a tunnel recombination junction in order for the electrons from the top cell and the holes from the bottom cell to recombine. Silicon oxide being a versatile material with tuneable properties, can be made highly transparent and conductive and used as a tunnel recombination junction as well as an intermediate reflective layer.

Current matching in a multi-junction solar cell is crucial in order to obtain maximum current output and best spectral utilization of all sub cells. However, under current matched conditions the best FFs are not obtained. Thus a micromorph tandem is always bottom cell limited to obtain maximum FF. This can be explained with figure 2.11 which represents the current density J plotted against the voltage of a micromorph tandem device. From the schematic, it is immediately clear that the current is bottom cell limited. This is due to the top cell having a current and voltage that is much larger that the bottom cell. It is to be noted that a-Si:H suffers from light induced degradation which results in decreased performance. Thus there is a decrease in current and FF which is represented by the yellow region of the JV curve. The squareness of the JV curve, or in other words the FF is mainly determine by this limiting bottom junction. Now, even after the loss of current due to LID, the tandem is still limited by the bottom cell. This results in a sharp knee of the tandem's JV curve (represented by the dashed line) indicating the highest FF achieved.

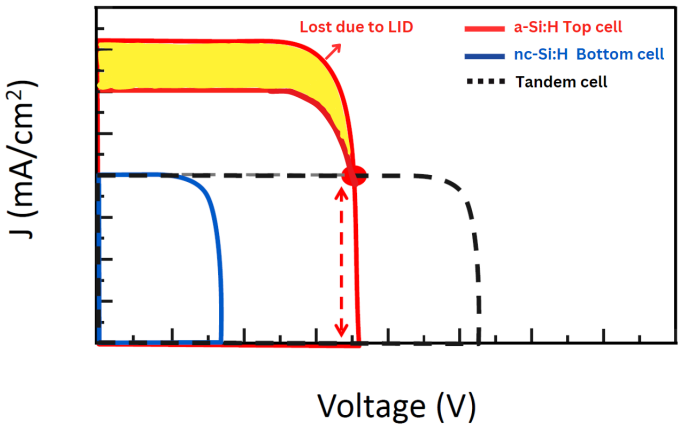

Figure 2.11: Current matching in a multi-junction device

2.3. Deposition methods

The solar cell fabrication involves a series of processing steps. All samples were made on high quality Asahi U type glass strips which are 10 cm long and 2.5 cm wide. These glass strips have predeposited fluorine doped tin oxide which acts as the transparent conductive oxide (TCO) at the front of the device.

2.3.1. PECVD

The a-Si:H solar cell's thin film semiconductor layers are deposited using radio frequency (RF) plasma enhanced chemical vapor deposition (PECVD), which has become a research and industry standard. Figure 2.13 illustrates a schematic representation of the PECVD tool. With this method of deposition, the precursor gas, which contains silicon, hydrogen, and potential doping agents in the right amounts, decomposes to create the desired layers. The plasma's function is to act as an energy source to split the precursor SiH_4 gas molecules apart. This is accomplished through collisions with electrons, which start out in the plasma as secondary electrons and gain energy through acceleration in an electric field. Radicals, which are reactive particles of dissociated SiH_4 molecules, are attached to the surface of the growing film to cause it to grow into an a-Si:H film [17]. The most prevalent radical in the plasma during the deposition of a-Si:H using silane gas is SiH_3, followed by SiH_2, SiH, Si, and H. These gases will diffuse to the grounded electrode and form a weak bond with the substrate's surface. Radicals that have been bound to the surface may combine with other loosely bound precursor radicals to leave the substrate. Growth does not naturally take place in this situation. However, if a radical joins with a DB in the substrate material, strong Si-Si bonds may form and the radical sticks, assisting in the growth of the film. According to the sticking probability, which is correlated with the radical's ability to diffuse across the substrate surface, the radical's likelihood of adhering to the substrate is determined. SiH_3 is more advantageous in this regard than SiH_2, SiH, and SiH, making it a more effective radical for annihilating DBs in the substrate material among the radicals created by the decomposition of silane [18].

This PECVD process was done at the Else Kooi Laboratory, TU Delft using Elettrorava's Amigo, a multi-chamber cluster tool that can deposit intrinsic, p- and n-doped thin-film a-Si and c-Si, Si alloys, and ZnO:Al layers. It consists of 5 ultra-high vacuum (UHV) radio frequency/very high frequency plasma-enhanced chemical vapor deposition (rf/VHF PE-CVD) chambers, a sputtering chamber, a load lock, and a UHV transport chamber with a programmable robotic arm for moving sample holders to and from the processing chambers and load lock.The Amigo enables the manual or automated (based on programmable recipes) creation of single layers on solar cell devices such as glass or c-Si substrates.

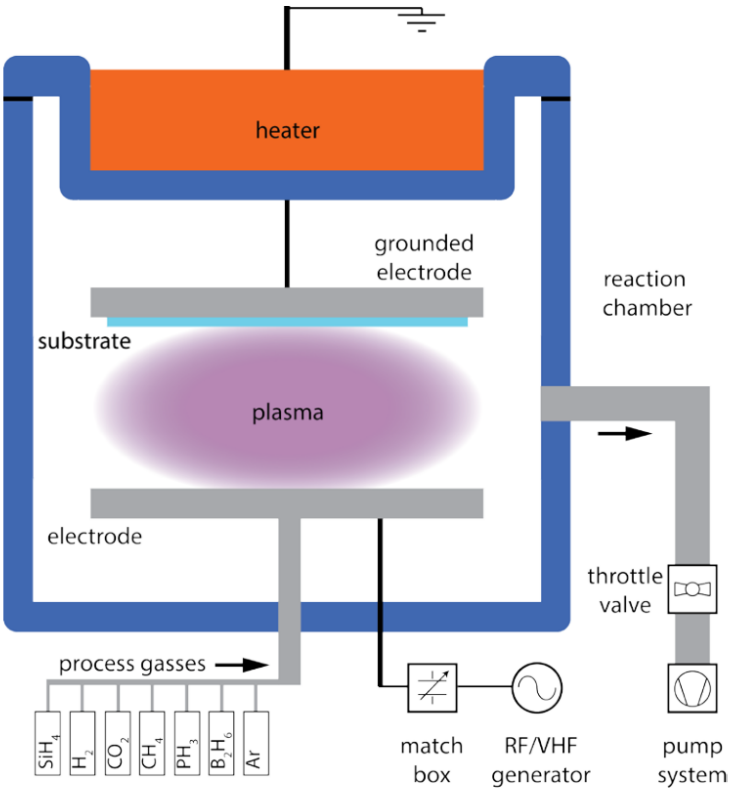

Figure 2.12: Schematic representation of PECVD chamber [29]

2.3.2. RF magnetron sputtering

The Provac PRO500S, created by Provac (which went out of business in 2009), is a physical vapor deposition device that evaporates SiO2, titanium, aluminum, or chromium using an electron beam. Thermal evaporation of silver can be done through resistive heating. An alternating electric field is applied between the material target and substrate by an RF generator. A portion of an inert gas, in this case argon, is ionized as a result. These accelerated positive argon ions strike the target and release species as they exit which are then deposited on the substrate [29]. The electrons are constrained close to the electrode surface in order to increase the ion-current density, which is achieved by applying a magnetic field perpendicular to the electric field. Thus, the term ”magnetron sputtering” refers to the process of sputtering and focusing electrons with the aid of a magnetic field.

This process is done to deposit the metal electrodes that make up the front and back contact of the device. The samples are placed inside a holder with masks which allows the depositions to be done on specific areas of the samples.

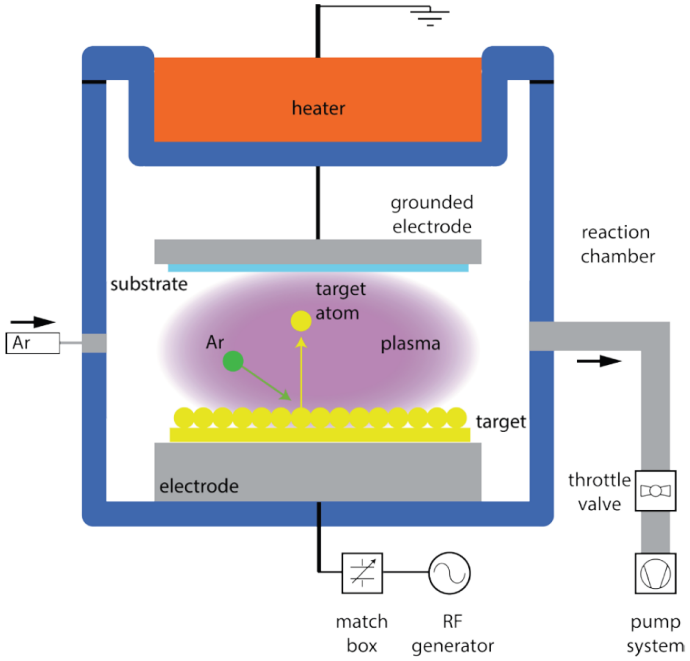

Figure 2.13: Schematic representation of Sputtering process [29]

2.4. Characterisation techniques

In this section, the techniques required to characterise a fully fabricated solar cell are explained.

2.4.1. Illuminated JV measurement

The illuminated JV measurement is done to determine the external parameters of a solar cell based on the power and JV curve obtained. This is done using a class AAA solar simulator called WACOM which operates based on two light sources, a Halogen and a Xenon lamp. With the use of certain filters, the high intensity emission lines in the infrared region is removed from Xenon lamp, and it simulates the AM 1.5 solar spectrum more accurately. The setup consists of a dedicated stage made for glass samples. It consists of 30 probes for back contact and 2 probes for front contact which are controlled by vacuum pump that is attached to the stage. Since one sample contains 30 solar cells of area 0.00016 m2, all the probes are activated at the same time and the IV sweep is done from 0V to 1V for single junction a-Si:H samples. The stage is also directly connected to a cooling unit which maintains the temperature at 25 °C. The whole setup is operated using a computer software which instantly displays the JV curve and the external parameters such as V_{oc}, J_{sc}, FF, η, shunt resistance (R_{sc}) and series resistance (R_{oc}).

2.4.2. External quantum efficiency (EQE) measurement

The external quantum efficiency (EQE) is the fraction of photons incident on the solar cell that create electron-hole pairs in the absorber which are successfully collected. It is wavelength dependent and is usually measured by illuminating the solar cell with monochromatic light of wavelength λ and measuring the photo-current through the solar cell [10]. If the EQE measurement is performed under short circuit conditions, it can be used to determine the J_{sc}. Determining J_{sc} via the EQE has the advantage that it is independent of the spectral shape of the light source used, in contrast to determining the J_{sc} via a J-V measurement.

To determine J_{sc}, the photon flow at a certain wavelength is combined with the EQE at this wavelength, leading to the flow of electrons leaving the solar cell at this wavelength [10]. J_{sc} then is obtained by integrating across all the relevant wavelengths and is shown in the equation 2.3.

$$J_{sc} = -q \int_{\lambda_1}^{\lambda_2} \mathrm{EQE}(\lambda) \Phi_{ph,\lambda}^{AM1.5} \, d\lambda \tag{2.3}$$

A schematic representation of an example of the EQE measurement setup is shown in figure 2.14. A Xenon arc lamp is used as a light source, which goes through a computer-controlled double pass monochromator. The measurement of a dc current cannot be accurate due to noise and lock-in amplifiers are used together with current/voltage amplifiers to have a better signal to noise ratio. The addition of a second reference diode is done in order to correct the measurement by small changes in the intensity of the illumination source (that may happen due to temperature variations, for example) [30]. In addition, the custom EQE setup at the ESP lab, TU Delft has eight bias lights, which are not included in the figure. Bias lights with different intensities at various wavelengths bias the junctions of multi-junction solar cells.

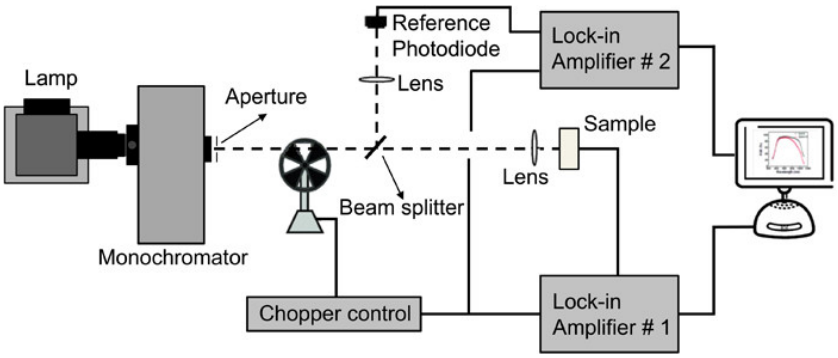

Figure 2.14: Schematic representation of an EQE measurement setup[30]

2.4.3. Reflectance measurement

This measurement is done using a Perkin Elmer spectrometer. The setup consists of several optical elements such as lenses, filters, mirrors and gratings. The optical system can ultimately create two monochromatic beams, one for the sample under test and one for reference. The light sources in the instrument are a tungsten halogen lamp and a deuterium lamp. Together with very precise optical components, the test spectrum ranges from 175 nm all the way up to deep infrared at 3300 nm. The monochromatic beam will enter a chamber, which is called an integrating sphere. The interior of this sphere is coated with Spectralon, which is a highly scattering and reflective material. If light enters the integrating sphere, it will reflect multiple times and scatter in all directions. The electromagnetic field will therefore be homogeneous inside the sphere, making it possible to evaluate the smallest light intensities at a single point on the sphere. Two different detectors are located on the bottom of the sphere, that each measure the light intensity in different wavelength ranges. It is known that when a light is incident on a solar cell, a part of the light gets reflected, a part of it gets absorbed by the layers (parasitic absorption) and a part of it gets transmitted (if it is transparent) which gives three quantities namely, reflectance (R), transmittance (T) and absorptance (A). Thus the relation between these three quantities can be described by the equation (2.2), which means the sum of the total reflection, the transmission and the absorption as a percentage of the incoming light intensity should equal one [31].

$$R + T + A = 1 \tag{2.4}$$

When a solar cell with a fully metallised aluminum or silver back contact, which has a reflectance of almost unity for longer wavelengths, the transmission term can be neglected. This simplifies the relation between reflection and absorption to equation (2.3). It is clear that in order to couple as much light into the solar cell as possible, the reflectance of the solar cell should be minimised.

$$R + A = 1 \tag{2.5}$$

2.4.4. Raman spectroscopy

Raman spectroscopy is a light scattering technique in which a molecule scatters incident light from a high intensity laser light source. The majority of the scattered light is at the same wavelength as the laser source and does not provide valuable information; this is known as rayleigh scattering. However, a little quantity of light is scattered at different wavelengths depending on the chemical structure of the substance, which is known as raman scattering. A raman spectrum has a number of peaks that represent the intensity and wavelength position of the raman scattered light. Each peak corresponds to a specific molecular bond vibration.

The raman measurements are performed with a Renishaw inVia Raman microscope. A raman spectroscopic experiment involves directing a monochromatic (laser) light onto the material of interest and measuring the intensity of the scattered light as a function of wavenumber, while filtering out rayleigh scattering to improve signal quality. The structural properties of the material are determined by the peaks in the resulting raman spectrum. Figure 2.15 illustrates the typical peaks of a-Si:H and c-Si when the raman measurement is performed with a green Argon laser of wavelength of 514 nm.

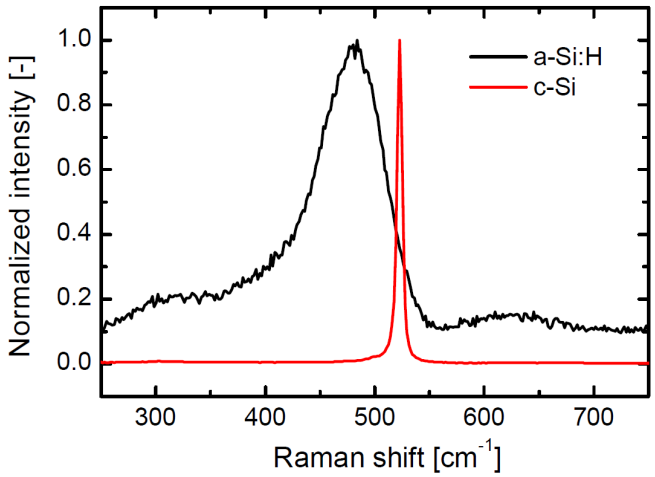

Figure 2.15: Typical raman spectra of a-Si:H and c-Si depicting the change in peak shapes and positions [20]

3

LID study of different qualities of a-Si:H absorber layer

3.1. Introduction

Light induced degradation (LID) of a-Si:H based solar cells have been extensively discussed in the literature over the past 4 decades and the underlying reason for the SWE is still under discussion. However, there have been significant efforts made in characterisation and mitigation of its detrimental effects on thin-film silicon solar cells.

LID in a fully fabricated device can have different origins as it is also dependent on the materials used, thickness of the layers and hydrogen dilution ratio [32] [18]. The effects of light soaking on the stability of various a-Si:H based devices are demonstrated in various research articles [33] [34] [35]. The stabilized efficiencies attained differ depending on the device architecture and deposition conditions. Although the initial efficiencies of such a device may appear to be high, it is crucial for a-Si:H based devices to achieve good stabilised performance. Therefore, a thorough analysis of the devices' stability is required before any optimizations can be made to enhance their stabilised performance.

In this chapter, the LID experiments conducted on TU Delft's unique device architecture of single junction a-Si:H thin film solar cells are discussed in detail. For this study, single junction devices with different qualities of intrinsic a-Si:H absorber layer were fabricated and characterised. Light soaking was carried out at two different temperatures to study the temperature dependence of LID and the stability of the devices. Furthermore, annealing experiments were carried out at various temperatures in order to study and gain insights on the reversal of the light induced meta-stable defects.

3.2. Background study

Ever since the identification of SWE, a significant amount of study that has been conducted over the years and has been published. However, it has still proven to be a highly challenging problem. Academic and industrial studies have made strides toward reducing SWE, but the root causes of this impact remain mostly unknown, and LID is still a concern. This section gives an overview of the progress made so far, towards understanding the SWE.

3.2.1. Proposed theories on SWE

Numerous theories offer explanations at the atomic level, with or without the active participation of mobile hydrogen and hydrogen-silicon bonds. The recombination of charge carriers that occurs during light soaking causes structural defects in all of them. These defects create electronic states near the mid-gap that serve as recombination centres and hinder effective charge collection. Some of the

particularly significant models are the ”weak-bond model” and the ”H-collision model”, which is more consistent with measurements of electron-spin resonance (ESR) [16].

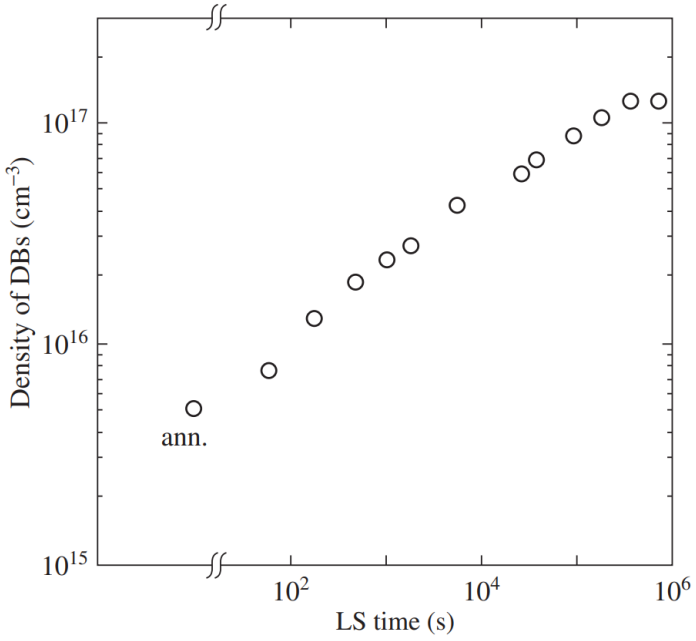

Figure 3.1: Density of dangling bonds (DBs) as a function of light soaking time [36]

The weak-bond model which is also referred as the SJT model proposed by Stutzmann, Jackson and Tsai in 1985 [37] demonstrated that hydrogen stabilizes newly formed dangling bond pairs by ”hopping” from a neighboring position to bind with one of the dangling bonds, showing that the SWE is an intrinsic, bulk effect of a-Si:H. This mechanism clarifies why broken Si-Si bonds do not instantly reform. A defect creation rate proportional to $t^{1/3}$, where t is the illumination time, was also asserted in the paper. In agreement to this paper, Klaver et al. [34] found a similar $t^{1/3}$ dependence for the increase in defect density in the intrinsic layer as a result of light soaking. However, the SJT model had a drawback in that it did not appear to match measurements of electron-spin resonance (ESR). Any localized phenomena, such as local hydrogen hopping close to dangling bonds, should leave a trace in the ESR results, but it did not.

As a consequent outcome, Branz developed the hydrogen collision model (HCM) in 1999 [38]. The HCM suggested that the Si-H bonds in the material are broken by recombination of photogenerated carriers, resulting in mobile hydrogen atoms, rather than attributing the SWE to specific structural changes in the material. When two of these atoms come together, they create a metastable two-H complex, leaving behind two dangling bonds that automatically turn into metastable compounds. Because the presence of the metastable two-H complex is statistically implausible and has not been empirically shown, the HCM is also not a strong contender for explaining the SWE. Figure 3.2 shows the Configuration-coordinate diagram of Staebler Wronski dangling bond creation as per HCM model.

Since there was no consensus on how to describe the flaws in a-Si:H, the complexity of the nanostructure was speculated to be the primary reason [39]. This led to new measurement methods such as Fourier transform photocurrent spectroscopy and Doppler-broadening positron annihilation spectroscopy in the last years where the complexity of a-Si:H can be distinctly seen on a nanostructure level. The nanostructure of a-Si:H is described as a glassy structure that has become to be known as the continuous random structure (CRN). It is explained in [40] that there exists a view where the a-Si:H network is not continuously random which has gained popularity since the 1980s when it was considered that vacancies and voids also likely play a role in an accurate description of the nanostructure. Figure 3.3 shows a new nanoscopic model proposed by Melskens et al. [39]. According to this

model, there could be two types of defects A1 and A2 in the a-Si:H nanostructures during LID. They correspond to large open volume deficiencies and randomly distributed defects respectively. These nanoscopic defect mechanisms takes place during LID where A1 increases moderately with S, which is the size of dominant open volume deficiency. And A2 increases strongly with S. It is also explained that the large open volume deficiencies could be more stable due to the presence of H_2 molecules which do not swiftly recombine with dangling bonds to form Si-H bonds due to the relatively high H-H dissociation energy. Based on this model, Melskens proposed that reducing the nanosized void density while increasing the H passivation degree of small open volume deficiencies as much as possible could make the most stable a-Si:H.

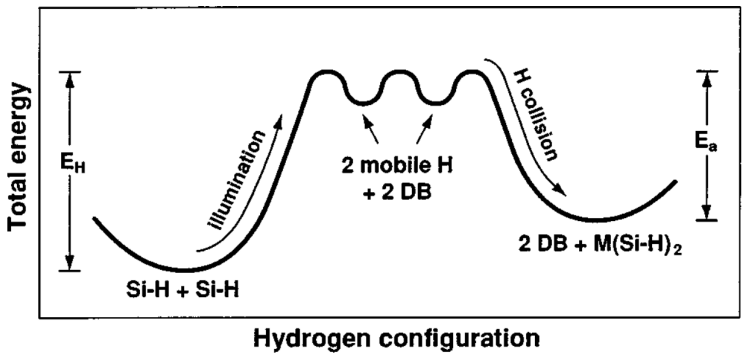

Figure 3.2: Configuration-coordinate diagram of Staebler Wronski DB creation as per HCM model [37]

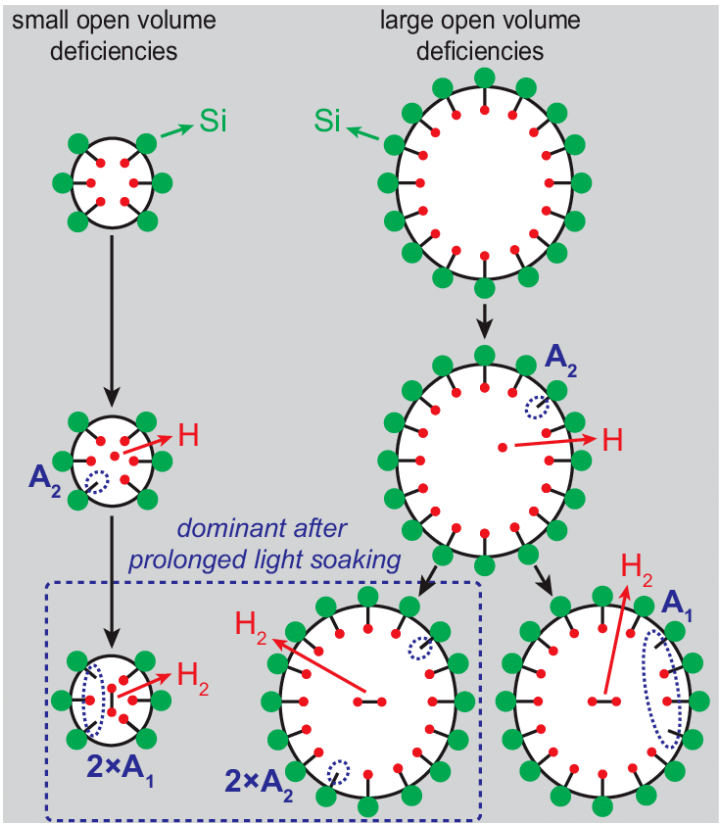

Figure 3.3: Nanoscopic model of LID in a-Si:H [39]

3.2.2. Influence of deposition conditions on LID

Deposition parameters and conditions determine the performance as well as the stability of a-Si:H thin film solar cells. Several results have been reported in literature, demonstrating the influence of thickness and hydrogen dilution on the LID of solar cells [18] [39] [41].

Beginning with thickness, a-Si:H solar cells with increased absorber layer thickness could lead to a higher level of LID in a device. Oppedal [18] found that the degradation of FF and V_{oc} are less influenced by the thickness of the device due to the variation in electric field strength at the interface of p-i-n structure where the band bending is more abrupt for thinner cells pertaining to a stronger electric field. The J_{sc} on the other hand seemed to have a different degradation pattern where the cells with absorber layer thickness more than 300 nm degraded heavily compared to the one with 300 nm absorber layer.

It has been stated that the hydrogen dilution ratio R, also has a significant influence on the LID of solar cells. Guha et al. [41] stated that hydrogen dilution improves order in amorphous material and since SWE is observed in amorphous materials only, it is reasonable to assume that the hydrogen dilution will reduce SWE. Furthermore, Van Elzakker [42] found that the stability of the cells is improved when a-Si:H is deposited with hydrogen diluted silane as compared to the conventional a-Si:H growth with pure silane. This applies only upto a certain value of R (R=20), pertaining to a saturation point after which there was no further improvement or difference between the initial and stabilised efficiencies.

3.2.3. Effects of thermal annealing

Thermal annealing is the process of heating a material at a given temperature for a given amount of time. As mentioned earlier, thermal annealing at about 130-150 °C reverses the creation of light-induced metastable defects in the structure of a-Si:H. Light soaking can provide the necessary amount of energy to cause a defect, while the introduction of a thermal load, i.e. thermal annealing, can overcome the energy barrier and allow the process to be reversed. The annealing temperature and the duration directly affects the rate at which the a-Si:H recovers from SWE. Figure 3.4 shows how the number of dangling bonds decrease after annealing.

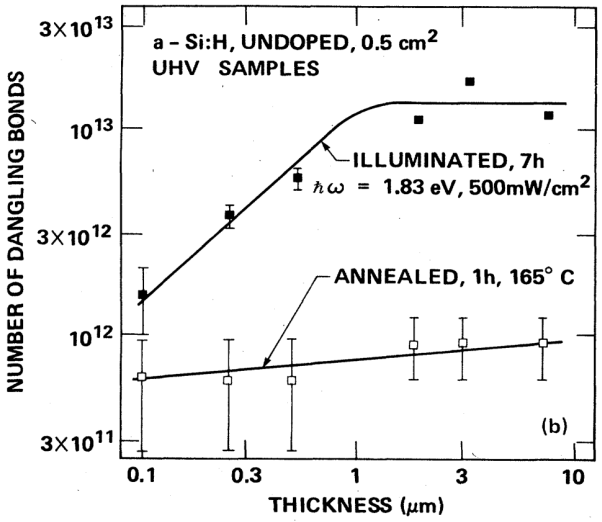

Figure 3.4: Variation of the number of dangling bonds with sample thickness after prolonged illumination and annealing [37]

Thermal annealing and light-induced degradation are considered as two continuously ongoing processes that create and eliminate defects in an equilibrium. As a result, shifting this equilibrium in the direction of defect creation requires raising the activation energy of annealing. Adding more thermal energy to the system causes the equilibrium to shift in favor of defect annealing [18].

Overall, the background study reveals that the exact cause of SWE is still unknown and there is still scope for further research. Recognising that LID varies depending on the deposition conditions and the properties of the a-Si:H material, it will be informative to investigate and compare the degree of LID of solar cells with different absorber layer qualities which has not been explored before.

3.3. Methodology

This section explains the complete methodology employed for the LID study. As the solar cell fabrication process is explained in chapter 2, the device description is first presented by providing sufficient information on the solar cell samples fabricated. Secondly, the initial performance of the samples is interpreted. Thirdly, the light soaking setup is introduced. And finally the design of experiments is explained with a flowchart.

3.3.1. Device configurations

Three samples consisting of 30 solar cells each were fabricated on ASAHI U-type commercial glass strips with predeposited fluorine doped tin oxide (SnO_2:F) which acts as the transparent conductive oxide (TCO) layer [43]. All three samples contain single junction devices with different qualities of a-Si:H. The term quality is used to refer to the a-Si:H absorber layer having either a low bandgap or a high bandgap depending on the deposition conditions (shown in table 3.1). Two out of the three samples have high and low bandgap a-Si:H absorber layers each while the third sample consists of a combination of high and low bandgap a-Si:H absorber layers. The purpose of using this type of configuration is to achieve better performance through increased J_{sc} and V_{oc} thereby attaining a higher fill factor. This is better explained with the interpretation of initial performance in the following section. Spectroscopic ellipsometry (SE) characterisation was used to determine the thickness, refractive index and optical bandgap energies of the samples. The SE measurements were fitted using Cody-Lorentz model and the parameter E_{04} was obtained by calculating the photon energy at which the absorption coefficient equals 10^4 cm^{-1}. In addition, the Tauc-Lorentz model was used to determine tauc bandgap energy E_{tauc}, which is a closer representation of the electrical band gap of the material. For the high bandgap a-Si:H E_{04} = 1.96; E_{tauc} = 1.94 and for low bandgap a-Si:H E_{04} = 1.87; E_{tauc} = 1.85. The refractive index of the high and low bandgap a-Si:H materials at a wavelength of 600 nm (n@600) was found to be 4.38 and 4.23 respectively.

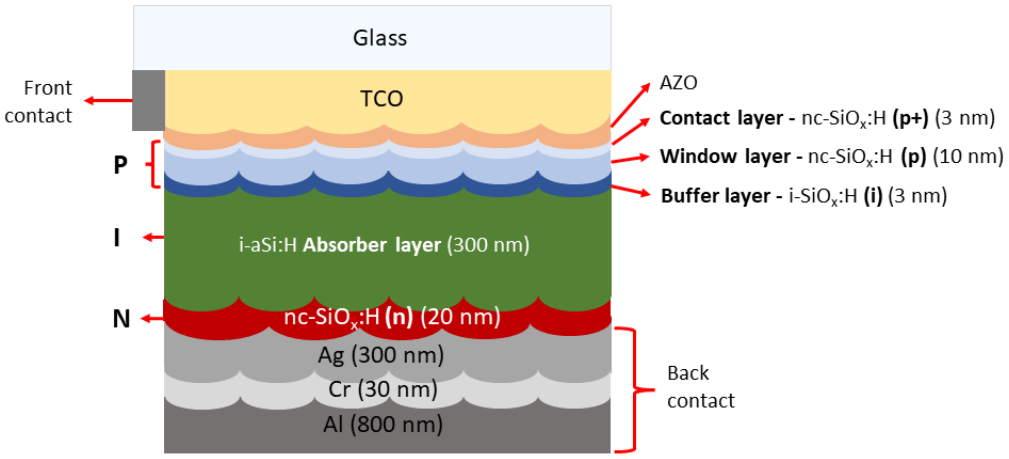

Figure 3.5: Device architecture of a-Si:H single junction solar cell with 1 a-Si:H absorber layer

The device architecture of the samples fabricated for the light soaking experiment is illustrated in figure 3.5 and 3.6. Each of the devices has a superstate p-i-n configuration. A narrow strip of front

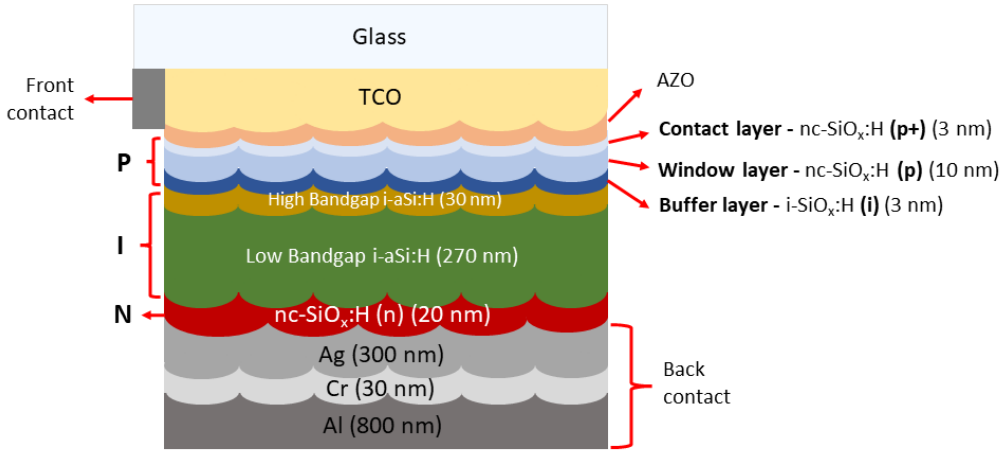

Figure 3.6: Device architecture of a-Si:H single junction solar cell with a combination of 2 a-Si:H absorber layers

contact is deposited on top of TCO layer of the ASAHI glass strips near the edge for charge carrier collection at the front. A triple layer structure is used for the p layer stack. The first layer is called the contact layer which is deposited first with a heavily doped nc-Si:O_X:H (p+). The purpose of a contact layer is to achieve an ohmic contact with the TCO layer so as to reduce the contact resistance which could lead to a higher FF [44]. The thickness of the contact layer is lower so as to have less parasitic absorption. The second layer of the triple p layer stack is called the window layer which is also made of nc-Si:O_X:H (p). This has a good conductivity and high optical bandgap to minimise the parasitic absorption. The large bandgap of the material also leads to better V_{oc} due to the increase in built in voltage of the material [45]. The third layer of the stack is called the buffer layer which lies at the interface between the p doped layers and the intrinsic bulk. The purpose of this layer is to have lesser recombination at the p/i interface (more detailed explanations are given in chapter 4). The intrinsic bulk layer which is 300 nm thick is deposited on top of the p layer stack followed by nc-Si:O_X:H (n) which is used as the n layer for better conductivity and less parasitic absorption at long wavelengths. Then finally, the back contact consisting of silver, chromium and aluminium is deposited. The purpose of such a combination is to attain higher reflection at the back and better conductivity in order to collect the electrons at the rear side of the device.

3.3.2. Initial performance

As the objective of the experimental study is to investigate the effects of light soaking on single junction devices with different qualities of a-Si:H, it is important to interpret the initial performance before proceeding with the light soaking experiments. Since there are 30 solar cells in a sample, the results of only one solar cell which had the best performance in terms of external parameters was chosen and interpreted. Figure 3.7 shows the initial plots of EQE, absorptance and illuminated JV.

The EQE plots show that, up to a wavelength of 550 nm, the spectral response is essentially the same for all three samples. However, it was anticipated to have a better blue response in the sample with high bandgap a-Si:H sample as the optical bandgap is supposed to be larger. This might be the result of inaccurate bandgap grading, which led to a smaller optical bandgap in the high bandgap a-Si:H sample. The high/low bandgap and low bandgap a-Si:H samples exhibit higher EQE than the high bandgap sample beyond 550 nm. The difference in optical bandgap should be the cause of this. The high/low bandgap a-Si:H exhibits a marginally better response at long wavelengths, as can be seen by close inspection. This is clear when examining the corresponding absorptance curves, which show that the high/low bandgap a-Si:H has superior absorptance to the other samples.

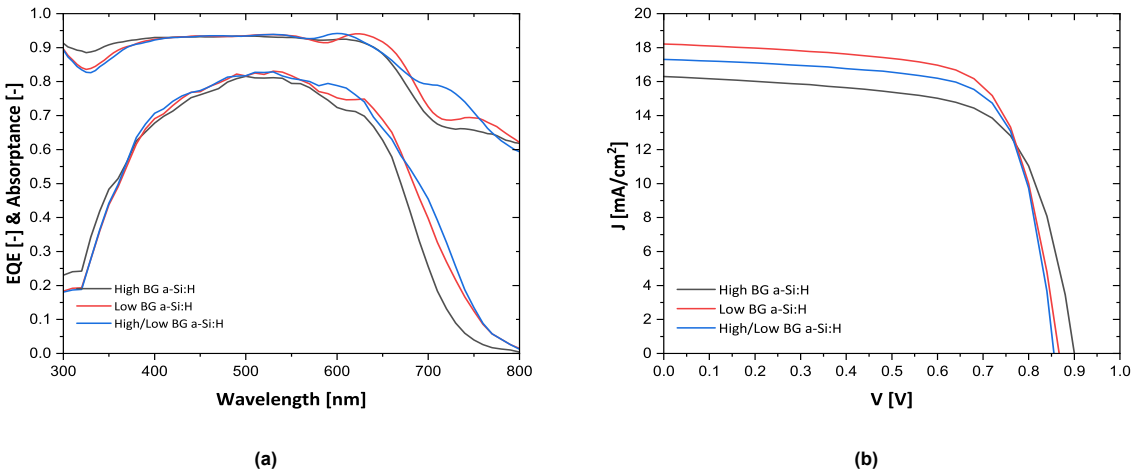

Figure 3.7: EQE, Absorptance and JV comparison of devices with different qualities of a-Si:H absorber layer

From the JV curves in figure 3.7 (b), it is immediately clear that the high BG a-Si:H has the highest V_{oc} which is nearly 0.9 V. This is due to the larger average size of the open volume deficiencies in a-Si:H when deposited at high pressure [22]. For the other two samples the V_{oc} is nearly similar. However, a higher V_{oc} was expected for the high/low BG a-Si:H samples as the thin layer of high bandgap material deposited on top of the low bandgap bulk would give an additional electric field which eventually increases the built in voltage due to band bending. It can be seen that the low BG a-Si:H sample has the highest J_{sc}. This is untrue, though, as the J_{sc} values from the JV characterisation are inaccurate. For greater accuracy and reliability, they are obtained from the EQE characterisation. Therefore, it was discovered that the High/Low BG a-Si:H sample had the highest J_{sc}, followed by the low BG a-Si:H and then the high BG a-Si:H, based on the J_{sc} data obtained from EQE characterisation. The external quantum efficiency results can be used to understand the underlying cause of the variation in J_{sc} of the samples. Furthermore, it was found that the high/low BG a-Si:H sample performed marginally better than the other two samples in terms of FF.

3.3.3. Light soaking

Solar cell samples were subjected to LID using the light-soaking setup designed by the PVMD group at TU Delft. Figure 3.8 shows a photograph of the light soaking setup. The light soaking setup consists of a stage where the samples will be placed for light soaking and a number of metal halide lamps for illumination. The set temperature of the stage is maintained by circulating deionized water with a cooling unit that is tubed to the stage. Mirrors on each of the four sides completely enclose the area between the samples and the lamps. The front side (open) of the setup is closed with a lid that has a mirror on the inside. A high sensitivity spectroradiometer was used to measure the light intensity of lamps, which was determined to be between 700 and 720 W/m^2. This light intensity value complies with IEC 61646, which sets the standards for light-soaking thin film solar cells.

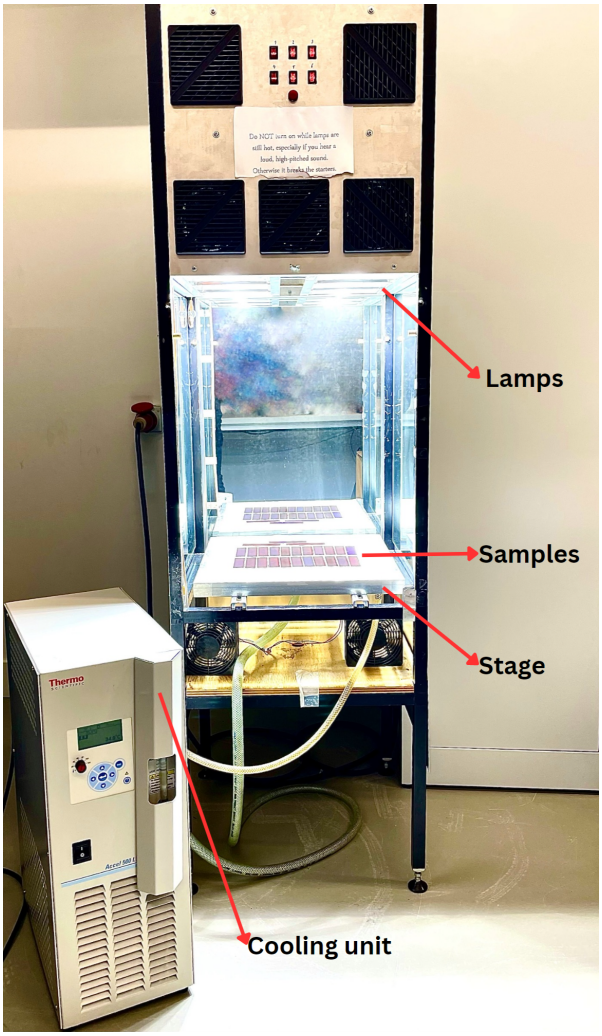

Figure 3.8: Photograph of the light soaking setup. Different components of the setup are denoted by arrows.

3.3.4. Design of experiments

The LID study was conducted based on a series of experiments and thus requires careful attention in order to understand how the results were obtained. Figure B.6 illustrates a flow chart that represents the complete design of experiments employed for this study. Three series of experiments were conducted, and they are denoted in the flowchart by the numbers 1, 2, and 3. The first and third series represents the light soaking experiments and the second series represents the annealing experiment. Firstly, the initial characterisation of the samples was done after annealing the samples at 180 °C for 20 minutes. The initial characterisation includes illuminated JV, EQE and Reflectance measurements. Then the samples were subjected to light soaking at open circuit conditions. In the first series, the light soaking was carried out at 25 °C i.e., the temperature of the samples were maintained at 25 °C. The intermediate data points obtained through EQE and illuminated JV measurements after light soaking are specified in the flow chart. It is to be noted that the light soaking was done upto 600 hours and the time periods are cumulative. The best performing cells that were chosen for characterisation in each of the samples are shown in figure 3.10. After the 600 hours of light soaking and characterisation, the annealing experiments were done at various temperatures starting from 60 °C to 210 °C for a duration of 30 minutes. Finally, another set of initial measurements were done before subjecting the samples to light soaking at 50 °C. For this series of light soaking experiments, different solar cells were selected in each of the samples in order to avoid the shunting of samples due to potential damage of back contacts as a result of repeated probing.

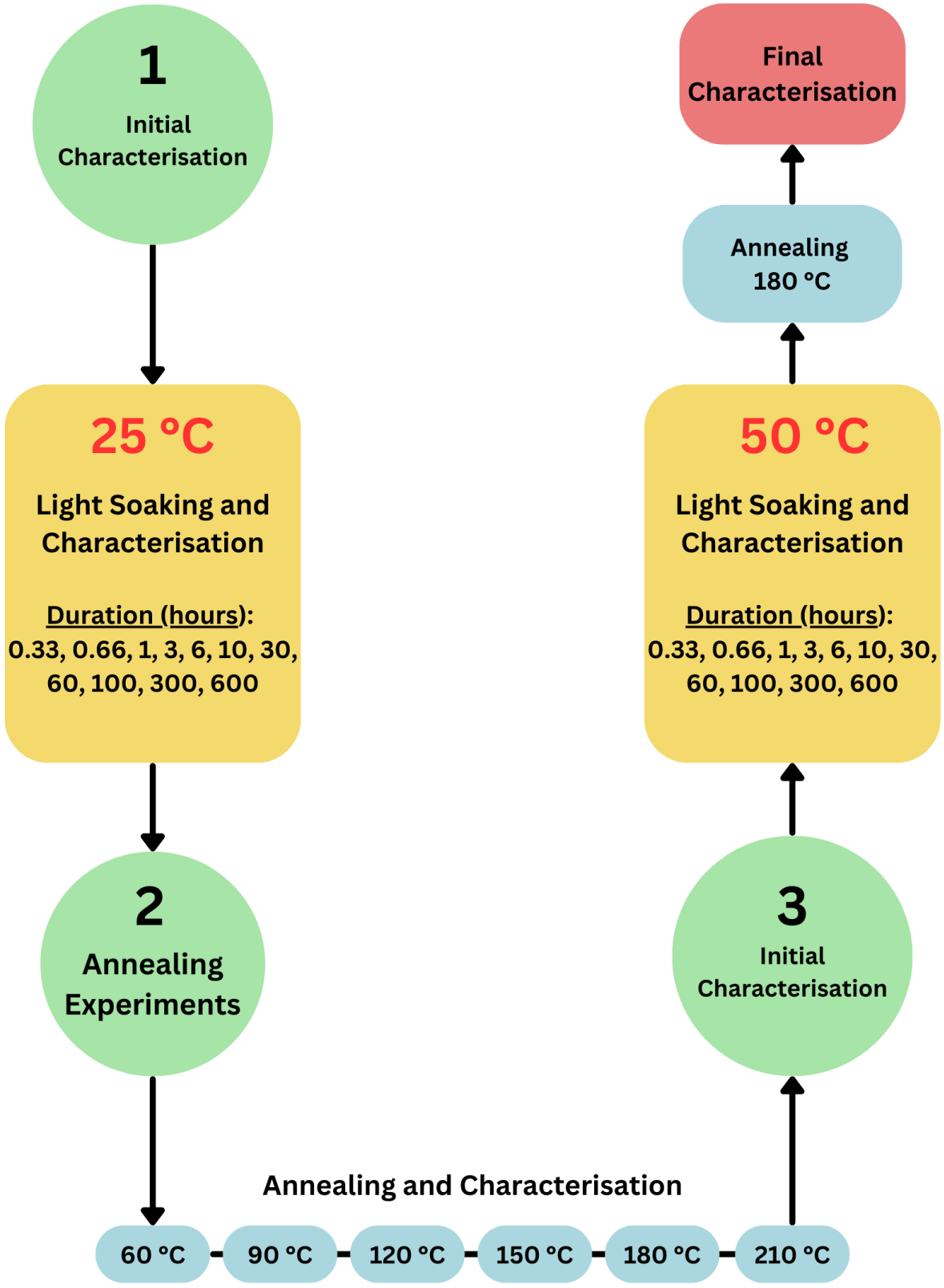

Figure 3.9: Flow chart representing the design of experiments employed for the LID study of devices with different qualities of a-Si:H absorber

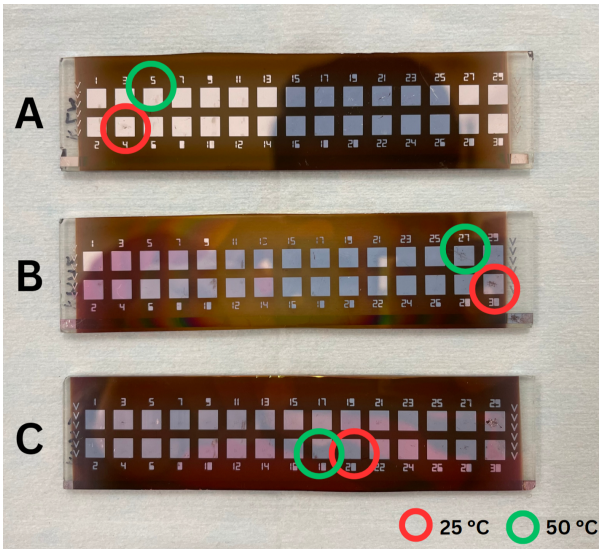

Figure 3.10: Photograph of the samples used for the LID study. 3 different samples were used. A - Low bandgap a-Si:H, B - High bandgap a-Si:H and C - High/Low bandgap a-Si:H. The cells marked with red and green circles represent the ones chosen for characterisation after light soaking at 25 °C and 50 °C respectively

Table 3.1: Processing conditions of the layers deposited for the fabrication of a-Si:H single junction thin film solar cells. The values are obtained from the standard recipes defined for the AMIGO cluster tool

Layer	Power (W)	Pressure (mbar)	Temperature (°C)	Gas	Flow rate (sccm)
AZO	300	2.6	300	Ar	20
nc-SiO_X (p+)	12	2.2	300	SiH_4 B_2H_6 CO_2 H_2	0.8 50 1.2 170
nc-SiO_X (p)	12	2.2	300	SiH_4 B_2H_6 CO_2 H_2	0.8 10 2.2 170
i-SiO_X (buffer)	12	2.2	300	SiH_4 CO_2 H2	0.8 2 170
High Bandgap a-Si:H (i)	9	10	200	SiH_4 H_2	3 200
Low bandgap a-Si:H (i)	2.8	0.7	300	SiH_4 H_2	40 0
nc-SiO_X (n)	11	1.5	300	SiH_4 PH_3 CO_2 H_2	1 10 1.2 100

3.4. Results and Discussion

3.4.1. EQE characterisation

The EQE of the solar cell provides a comprehensive picture of the device's optical response and electric losses. As a result, the external quantum efficiency study illustrates both the absorption of light in a material and the behavior and movement of the light induced charge carriers inside the device.

As mentioned earlier, one sample contains 30 solar cells (also referred as dots) of area 0.000016 m^2 per cell. Due to time constraints and limitations of the equipment, the EQE measurements were done for one chosen dot which had the best initial performance throughout the experiments. The results from the light soaking experiments at 25 °C and 50 °C were plotted and are shown in figure 3.11, 3.12 and 3.13 which corresponds to the samples, low bandgap aSi:H, high bandgap a-Si:H and high/Low bandgap a-Si:H respectively. Only the initial absorptance curves are plotted for all the samples as LID only affects the electrical properties of a material and not optical. In other words, when light is incident on the solar cell, the same amount of photons get absorbed irrespective of the LID but not the same quantity of charge carriers (electron-hole pairs) are collected. This is primarily due to the increase in recombination of the light excited charge carriers that are generated within the cell [35].

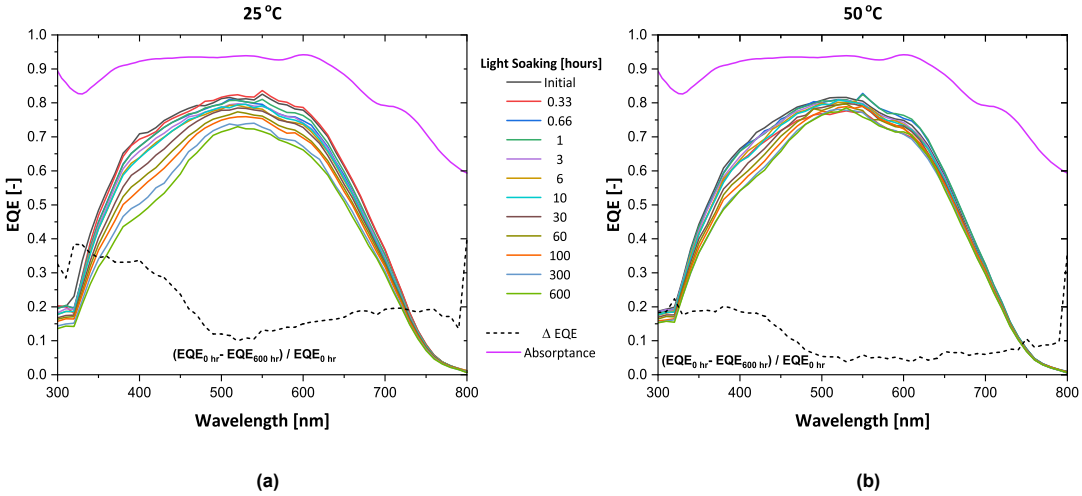

Figure 3.11: EQE plots of low bandgap a-Si:H sample after light soaking at (a) 25 °C and (b) 50 °C

From figure 3.11 (a), it is very evident from the significant drop in EQE that the solar cell had a severe degradation in the short wavelength range (from 350 to 550 nm) when the light soaking was carried out at 25 °C. Beyond 550 nm there is still some decrease in response but is relatively lower compared to the response in the short wavelength. This can be distinctly seen through the dashed curve (Δ EQE) which represents the difference in EQE from initial to 600 hours of light soaking with respect to initial EQE. From figure 3.11 (b), which represents the results of light soaking at 50 °C it can be clearly seen that there is a considerably less overall degradation. Comparing the Δ EQE of figure 3.11 (a) and (b), it can be observed that the EQE lost when the light soaking was carried out at 50 °C is about 50% lower than that of light soaking at 25 °C. This indicates that at a higher temperature there is some active reversal of meta-stable defect creation as the solar cell indirectly goes through an annealing process which results in decreased recombination.

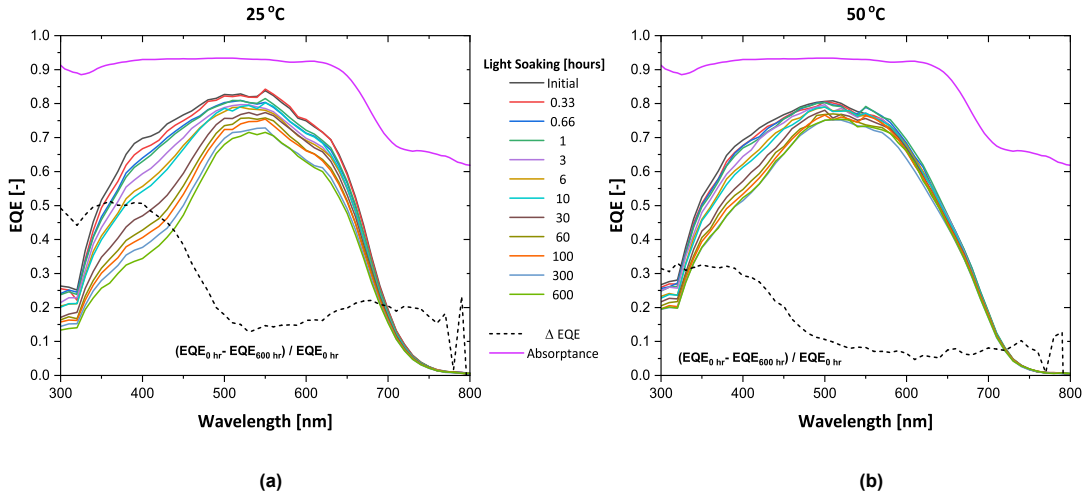

Figure 3.12: EQE plots of high bandgap a-Si:H sample after light soaking at (a) 25 °C and (b) 50 °C

Figure 3.12, represents the EQE plots of the high bandgap a-Si:H sample. It can observed that there is a severe degradation when light soaked at 25 °C compared to 50 °C. Compared to the results of the low bandgap a-Si:H sample, it can be noted that the degradation in the blue region of the high bandgap a-Si:H sample is significantly stronger. This is due to the presence of nanosized voids that makes the material more porous with higher native and metastable defect densities. Taking a closer look at the longer wavelength range (600-700 nm), it can be seen that there is a subtle difference in the shape of the curves between the figure 3.12 (a) and (b). This loss could be a result of the permanent degradation, as the sample had undergone a complete light soaking cycle for 600 hours and a set of annealing experiments (will be explained later in this section) in order to conduct light soaking at 50 °C.

Examining the EQE plots of high/low bandgap sample from figure 3.13, it can be seen that the Δ EQE when light soaked at both 25 °C and 50 °C is certainly lower than the high bandgap sample. Furthermore, these results are comparable to the low bandgap sample. This specific configuration is of great interest as the overall response is better which resulted in higher J_{sc} (refer 3.4.3) and the electrical performance is expected to be better which will be discussed in detail in the coming subsections.

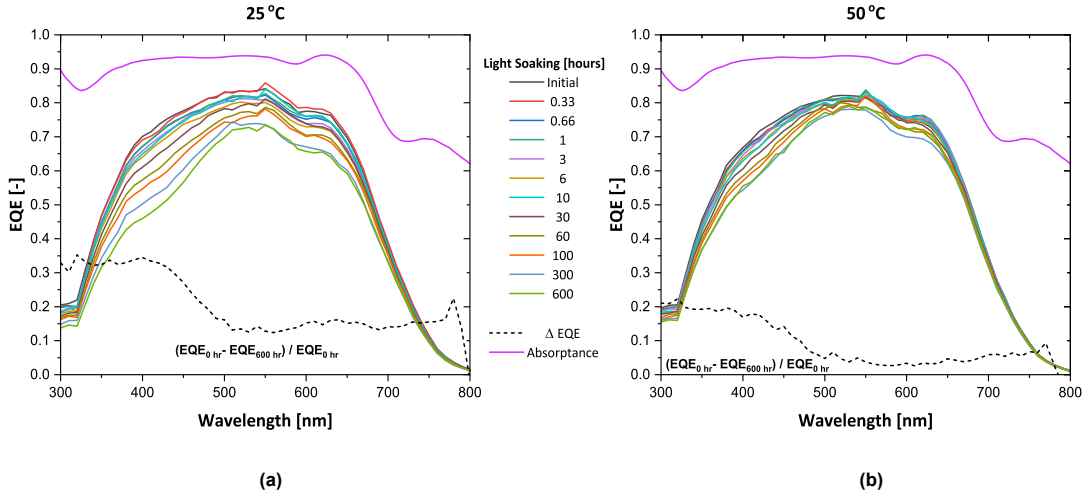

Figure 3.13: EQE plots of high/low bandgap a-Si:H sample after light soaking at (a) 25 °C and (b) 50 °C

When the EQEs of the three samples are compared, it can be seen that the low bandgap a-Si:H and high/low bandgap a-Si:H samples degrade less than the high bandgap sample. As the hydrogen dilution ratio R is zero for low bandgap material, the a-Si:H bulk could have fewer defects/voids compared to high bandgap material. However, compared to the long wavelength region, the degradation of all the

samples in the short wavelength region was relatively severe. It is speculated that this is a problem with the recombination brought on by defects in the p/i interface.

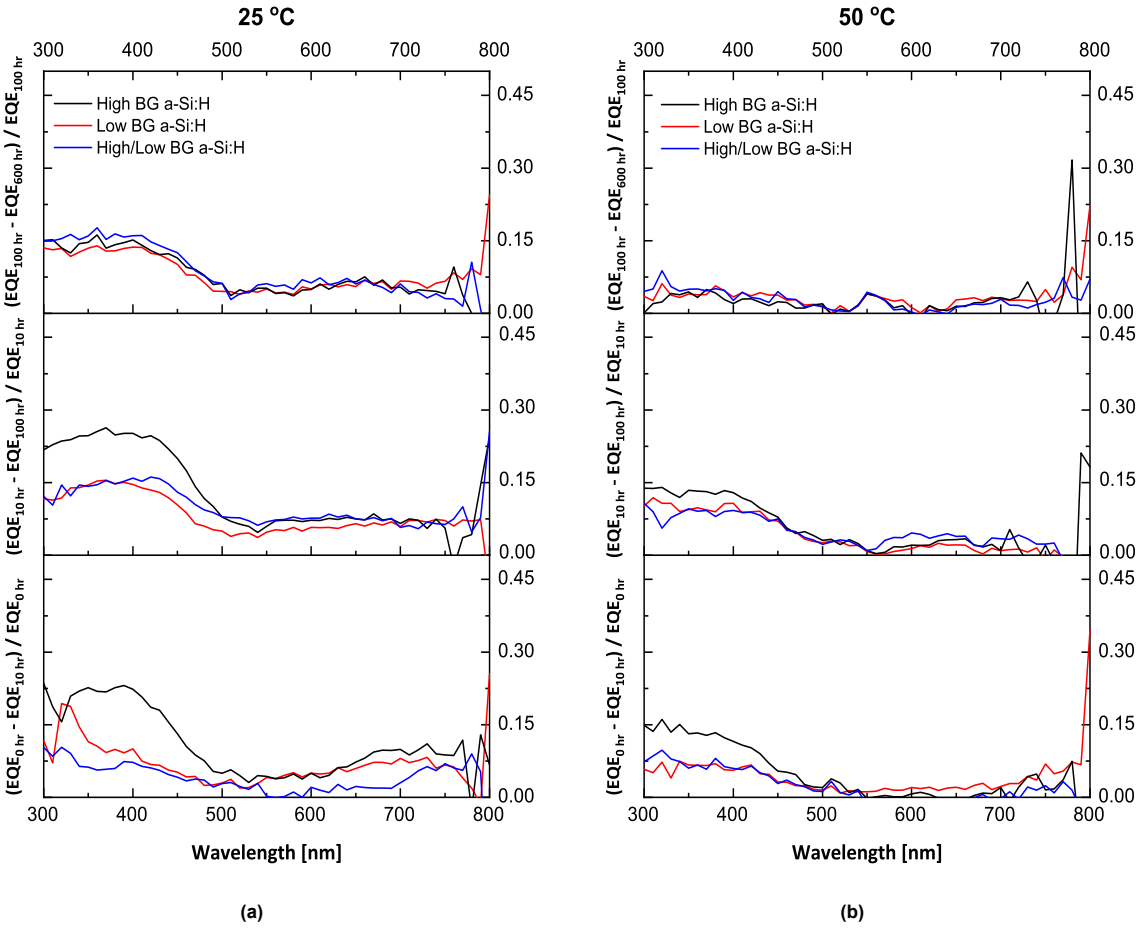

Figure 3.14: Relative difference in EQE between specific time periods of light soaking at (a) 25 °C and (b) 50 °C

Figure 3.14 illustrates the plots that corresponds to relative difference in EQE between two time periods of light soaking. Looking at the plots of 25 °C light soaking results, it can be observed that maximum degradation has occurred between 10 and 100 hours of light soaking where the high BG a-Si:H degraded more than the other samples between 300 nm and 500 nm. This is however not observed in the results obtained from light soaking experiments at 50 °C. Considering the loss of EQE in the first 10 hours, similar difference can be observed where the high bandgap a-Si:H degraded the most followed by low and then high/low bandgap a-Si:H. It is assumed that high nanosized void density in the high bandgap a-Si:H could be the cause of the increased SWE in the first 10 hours. It is also to be noted the relative difference in EQE between 100 and 600 hours of light soaking shows no significant difference between the samples which implies the SWE subsiding to attain saturation.

Overall, it can be clearly inferred that light soaking at a higher temperature is indeed giving a better performance as the degradation is significantly lower compared to the results of light soaking at 25 °C. Furthermore, a closer look at the plots in figure 3.11, 3.12 and 3.13 gives a clear indication of stabilisation in the results of light soaking at 50 °C as the 300 hour and 600 hour curves are superimposed on each other representing a saturation point of degradation. This cannot be observed in the results of light soaking at 25 °C as the degradation appears to continue further.

3.4.2. Illuminated JV characterisation

A solar cell's electrical performance can be greatly understood by using illuminated JV characterisation. This section discusses the illuminated JV characterisation results in relation to the JV curves. The next subsection makes use of separate plots to interpret each of the individual external parameters. Figure 3.15, 3.16 and 3.17 represents the JV curves of low bandgap a-Si:H, high bandgap a-Si:H and high/low bandgap a-Si:H respectively.

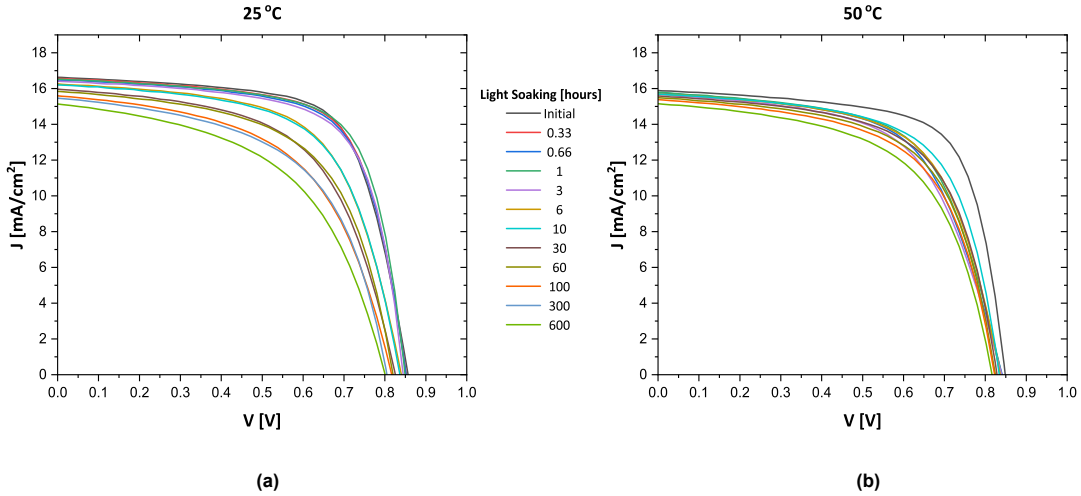

Figure 3.15: Illuminated JV plots of low bandgap a-Si:H sample after light soaking at (a) 25 °C and (b) 50 °C

From figure 3.15, it can be observed that there is a visible difference in the degradation between the results of light soaking at 25 °C and 50 °C where light soaking at 25 °C appears to have severe degradation. As the light soaking duration increases, it can be seen that the knee of the JV curves become more blunt, which represents a decline in FF caused by increased R_{oc} and decreased R_{sc}. There is a J_{sc} reduction of about 0.5 mA/cm^2 when comparing the initial curves of the two graphs. This decline from the initial value is the result of the solar cells' permanent degradation after undergoing a full cycle of light soaking for 600 hours and a series of annealing experiments at various temperatures. Furthermore, it should be noted that the JV plot of 0.66 hours of light soaking is unavailable in figure 3.15 (b). This was due to a measurement error brought on by improper probe contact with the solar cell's back contact, thus considered as an outlier.

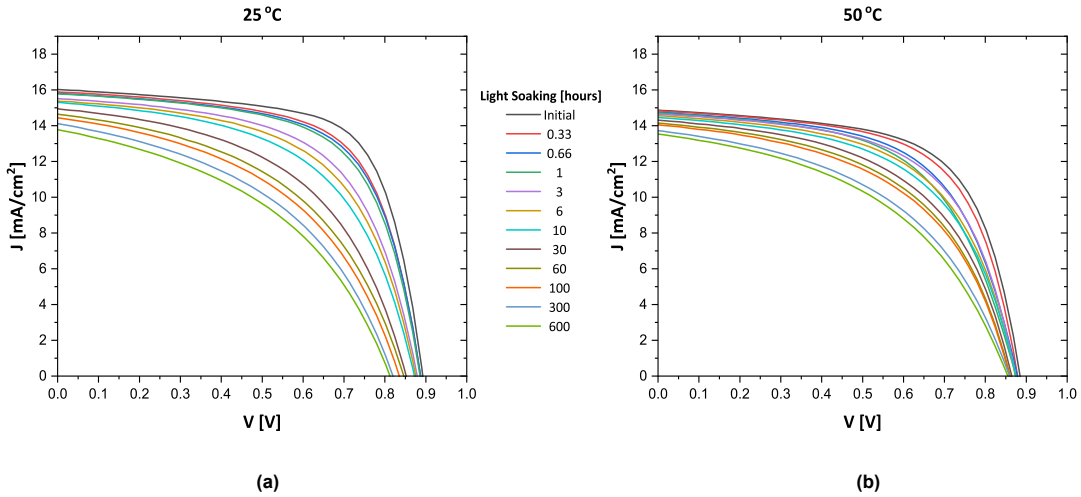

Figure 3.16: Illuminated JV plots of high bandgap a-Si:H sample after light soaking at (a) 25 °C and (b) 50 °C

As expected, the high bandgap a-Si:H sample, which is more defective, exhibits the most severe degradation. Figure 3.16 shows that the FF has significantly decreased regardless of the light soaking

temperature. Furthermore, even in the results of light soaking at 50 °C, the 300 and 600 hour curves are not superimposed indicating the possibility of further degradation when light soaked. It can be observed that the high bandgap sample has also experienced a permanent degradation that resulted in decreased initial performance in the light soaking experiment at 50 °C, similar to what is mentioned for the low bandgap sample. To learn more about the performance of this sample, the external parameters are further examined. The following subsection goes into more detail about each of them.

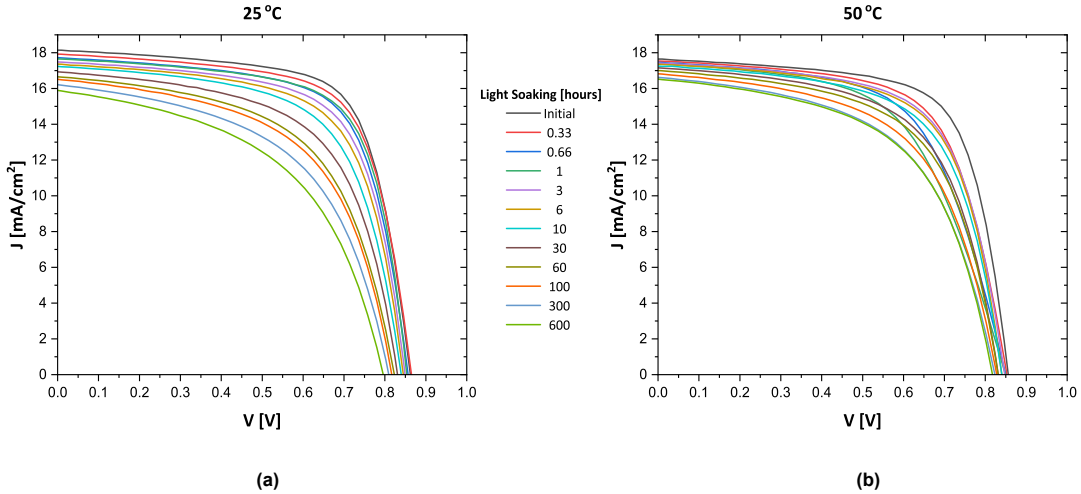

Figure 3.17: Illuminated JV plots of high/low bandgap a-Si:H sample after light soaking at (a) 25 °C and (b) 50 °C

Examining the JV curves of high/low bandgap a-Si:H sample in figure 3.16, it shall be stated that the degradation has been quite significant when light soaked at 25 °C, while it has saturated after 300 hours of light soaking at 50 °C. Furthermore, the trends of 50 °C degradation of high/low bandgap a-Si:H sample are comparable to low bandgap a-Si:H sample. Overall, it can be concluded that light soaking at 50 °C has left the samples less degraded despite the fact that there was permanent degradation after the light soaking experiments at 25 °C.

3.4.3. External parameters

Based on the outcomes of the light soaking experiments at 25 °C and 50 °C, all the external parameters obtained from the JV characterisation are individually plotted and compared side by side. The J_{sc} plots, on the other hand, are based on data obtained from EQE measurements. As a result, the J_{sc} data from EQE was also taken into account while making the efficiency plots. A crucial point to remember is that the J_{sc} data from EQE characterisation is obtained by measuring the EQE of the best performing cell out of the 30 cells in a sample, as opposed to the JV characterisation which is done on all 30 cells. This limits the ability to plot the average data of the best-performing cells along with error bars. However, in order to observe the trends for more reliability, this has been attempted using box plots on the external parameters apart from J_{sc} and efficiency. It was discovered that they largely adhere to the patterns of plots constructed using just one cell (refer appendix A for the box plots).

It should be noted that the LID does not reach saturation in all the external parameter plots. The light soaking, however, is still enough to keep track of the kinetics of light-induced defect formation by analysing the external parameters. The plots that are discussed below has some data points depicted using stars. They represent the data obtained after annealing the samples at 180 °C for 30 minutes.

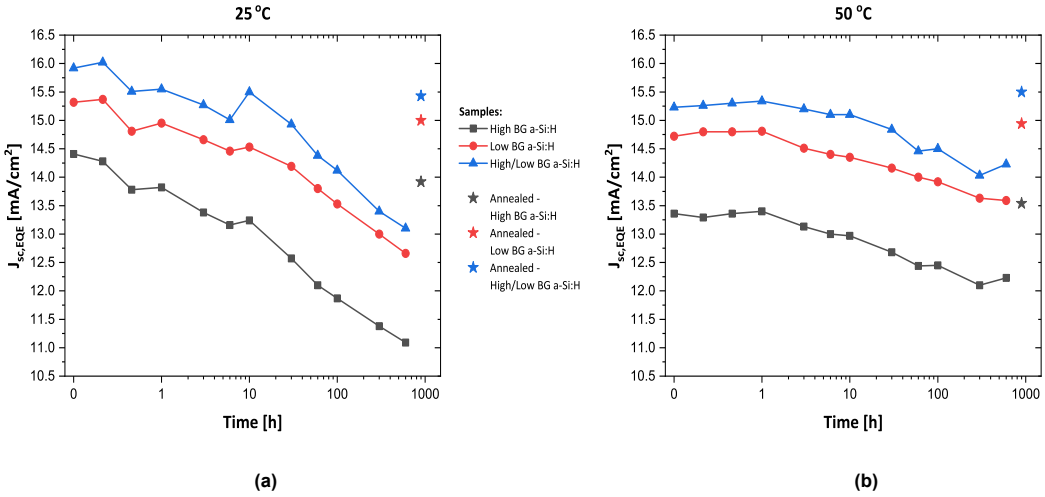

Figure 3.18: J_{sc} plots after light soaking at (a) 25 °C and (b) 50 °C

Figure 3.18 indicates that trends have a higher slope for the J_{sc} plots of light soaking at 25 °C while the slope of the trends is significantly lower at 50 °C. Irrespective of the light soaking temperature, the order of the trends based on the samples remained the same where the high/low bandgap a-Si:H sample performed the best followed by low bandgap and then high bandgap. By taking into account the EQE plots in figure 3.7 it is possible to understand why the high/low bandgap sample performed the best. This sample clearly had the highest absorptance and carrier collection, which resulted in an increased J_{sc}.

Upon inspection of the post annealing data points in the same figure, a complete reversal of the meta-stable defects was not observed as the data points did not reach the initial values. On the contrary, the results of 50 °C light soaking experiments show an improved performance as the post annealing data points are higher than that of the initial values. This might be due to the active creation and reversal of meta-stable defects when light soaked at 50 °C that could have decreased the probability of permanent degradation.

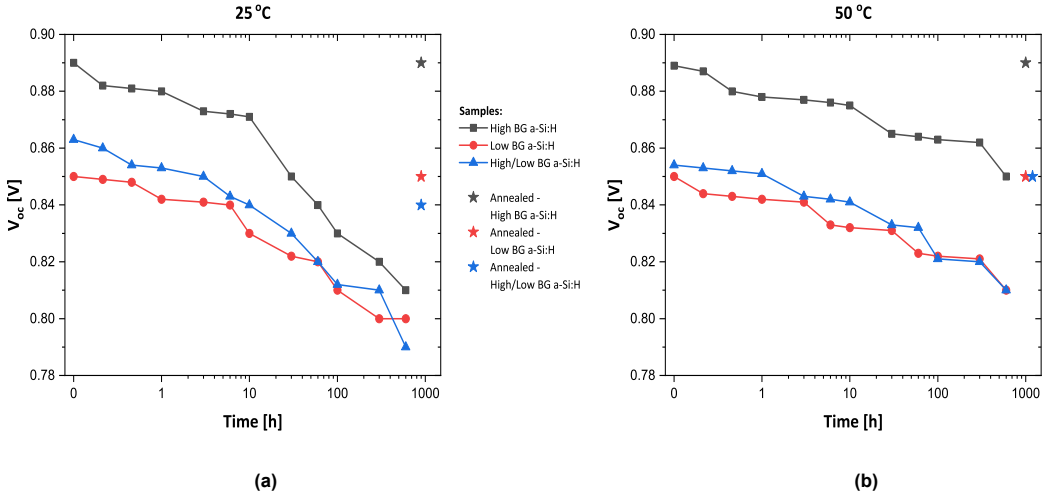

Figure 3.19: V_{oc} plots after light soaking at (a) 25 °C and (b) 50 °C

Similar to the J_{sc} plots, the V_{oc} plots in the figure 3.19 appear to have steeply declining trends at 25°C and relatively better trends at 50°C. The high bandgap a-Si:H has the highest V_{oc} before and after degradation when looking at absolute values. As mentioned before, the increased bandgap caused by the larger average size of open volume deficiencies in a-Si:H [22] is what causes the high V_{oc}. The decrease in V_{oc} of the low bandgap and the high/low bandgap sample does not differ significantly. A

higher initial V_{oc} in the high/low bandgap a-Si:H sample was caused by the incorporation of a thin, high bandgap layer, but after degradation, both samples were close to the same value. Interestingly, it can be seen that the annealing result of both light-soaking experiments show a complete recovery of V_{oc} in the high bandgap sample. The other two samples, however, did not fully recover at 25 °C. This may be a permanent degradation due to multiple annealing characterisations at different temperatures that the samples were subjected to, during the annealing experiments (refer 3.4.5 for more information).

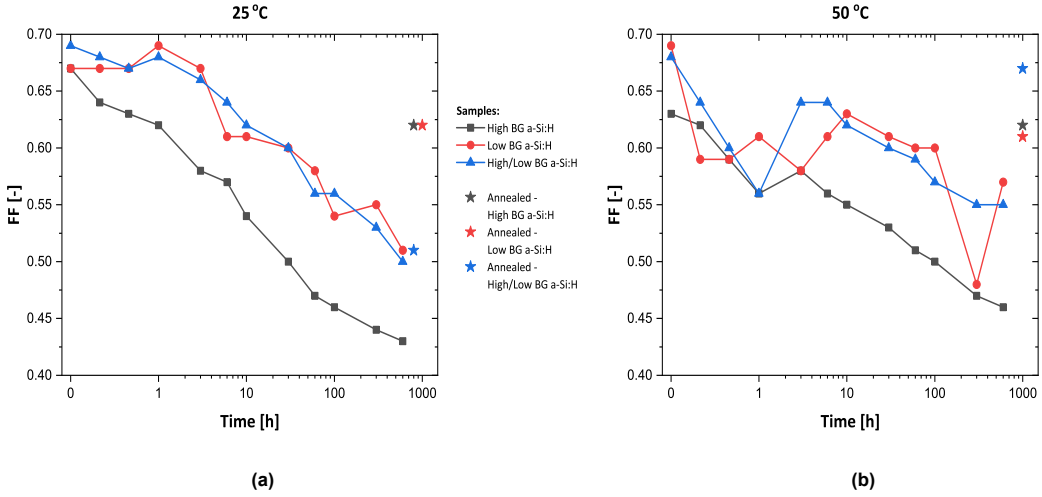

Figure 3.20: FF plots after light soaking at (a) 25 °C and (b) 50 °C

It is immediately apparent from the FF plots in figure 3.20 that the high bandgap sample, which is the most degraded, experienced a more linear decrease in FF over the course of light exposure. This holds true regardless of the temperature of the light soaking. The trends are essentially the same in the other two samples, and they appear entwined in both graphs. This indicates that during light soaking, the high/low bandgap sample experienced an equal amount of defect creation and recombination as the low bandgap sample. Furthermore, there is some inconsistency in some plots especially in the low bandgap sample which is indeed due to some unavoidable measurement errors that happen due to improper contact of the probes during the JV measurement. It is also to be noted that the annealed data of high/low bandgap sample at 25 ° is no longer reliable as the cell was shunted during the annealing experiments. However, the annealing results of a different cell that was used for the light soaking experiments at 50 °C demonstrates that the high/low bandgap sample recovered well compared to the rest.

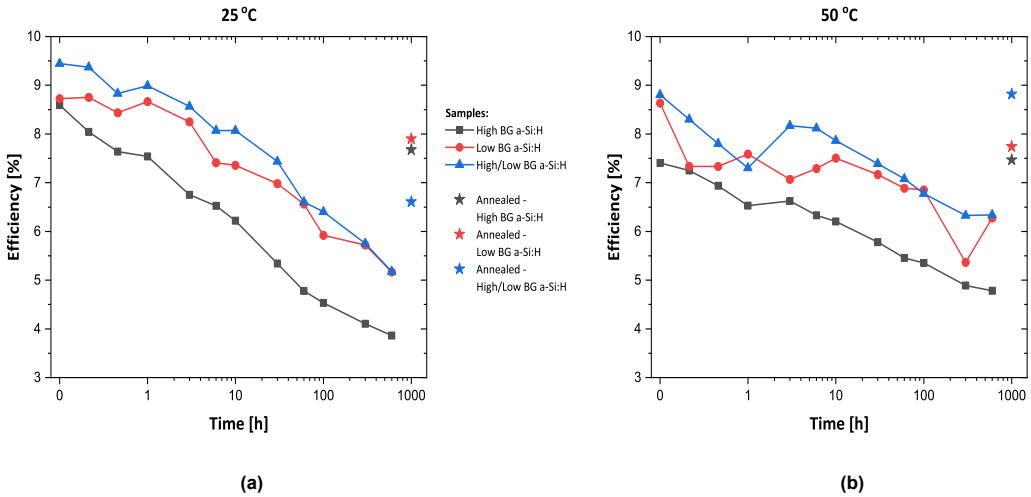

Figure 3.21: η plots after light soaking at (a) 25 °C and (b) 50 °C

Comparing the efficiency plots shown in figure 3.21, trends similar to the FF plots is observed. The results of light soaking experiment at 50 °C shows that the efficiency of high/low bandgap samples stabilised after 300 hours of light soaking at about 6.5%. Though there has been around 2.5% decrease in efficiency, it is still considerably better compared to loss in efficiency of more than 4% at 25 °C light soaking. No concrete comment can be made on the stabilised efficiency of low bandgap sample as the trends seems to be slightly inconsistent.

3.4.4. Series and shunt resistance

The experimental results for the R_{oc} and R_{sc} parameters have also been plotted for each light soaking temperature measurement which are shown in figure 3.22 and 3.23.

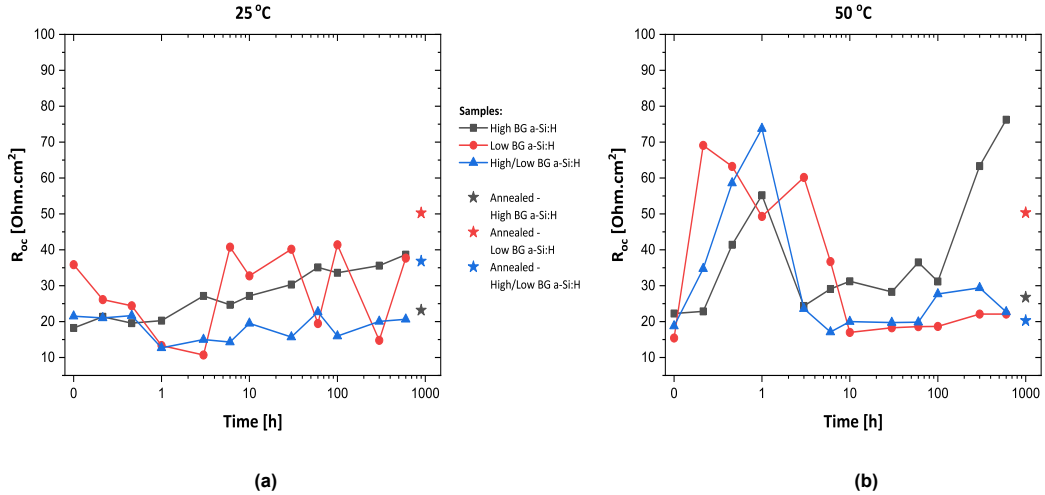

Figure 3.22: R_{oc} plots after light soaking at (a) 25 °C and (b) 50 °C

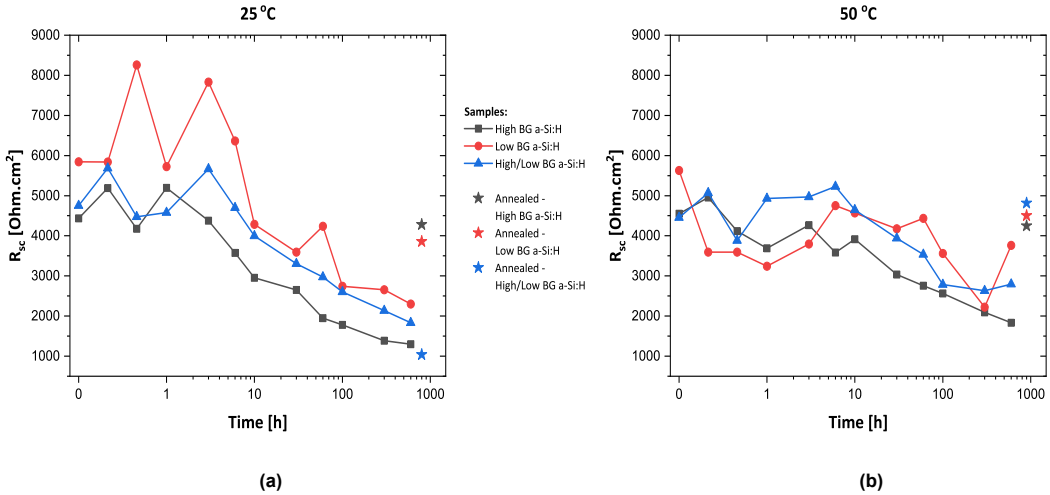

Figure 3.23: R_{sc} plots after light soaking at (a) 25 °C and (b) 50 °C

It is readily apparent that the R_{oc} has increased and R_{sc} has decreased during light soaking, over time. Both are indicators that the degradation is making the JV curve less ideal. Upon examination of the R_{oc} plots, it can be observed that they are quite erratic in some data points. This could be a result of a measurement error or an inaccuracy of inverse slope at the V_{oc} which represents the series resistance being calculated from the JV curve. Thus, the absolute values are not being greatly considered and only the nature of trends are observed for understanding. R_{sc} plots on the other hand seem to be less erratic and also shows a steep declining trends at both light soaking temperatures. This implies that

the decrease in performance of the solar cell due to LID, is more influenced by the shunt resistance than the series resistance.

3.4.5. Annealing study

As described in 3.3.4, the annealing study was done in between the light soaking experiments carried out at two different temperatures. The purpose of this study is to understand the effects of annealing temperature on the reversal of the defect creation due to SWE and determine the temperature at which maximum reversal is observed. In this study, the annealing was done in the dark so that the effects of light soaking is absolutely non existent. For consistency, the annealing duration was maintained at 30 minutes for every annealing temperature. The EQE and illuminated JV measurements were done immediately after each annealing run and the samples were kept inside a vacuum chamber in the dark between the annealing runs to preserve the samples from any changes due to instability or light soaking effects.

EQE and Illuminated JV characterisation

Figure 3.24, 3.25 and 3.26 shows the results of EQE and illuminated JV characterisation obtained after the annealing experiments. It should be noted that the black dotted curve in the graphs represents the state of the sample after light soaking for 600 hours at a temperature of 25 °C. The continuous black curve represents the initial state (before light soaking).

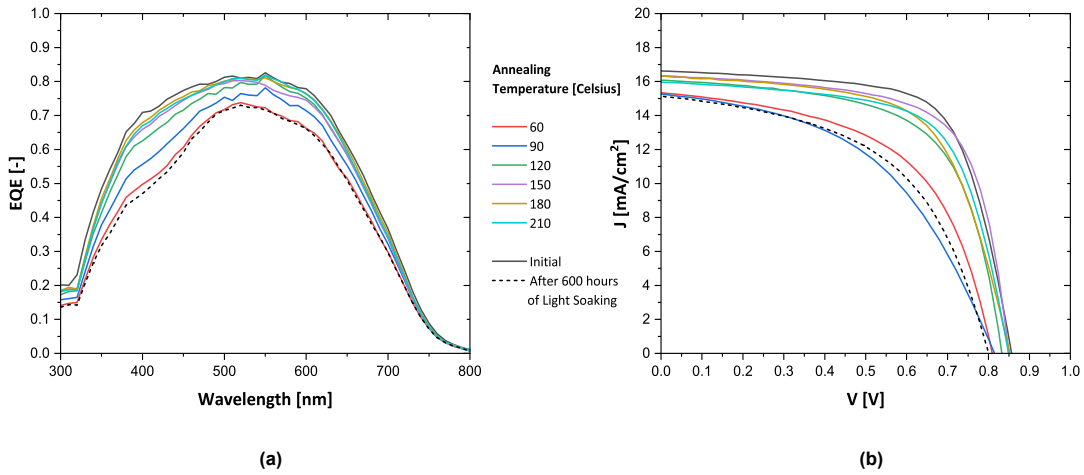

Figure 3.24: (a) EQE plots and (b) illuminated JV plots of low bandgap a-Si:H sample after annealing

Examining the results shown in 3.24 (a), it is found that the evolution of EQE strongly depends on the annealing temperature. As the annealing temperature increases, the recovery of EQE is more prominent. Furthermore, a complete recovery of the EQE is already seen at an annealing temperature of 180 °C. Beyond that there is no further increase in EQE which can be confirmed by taking a look at the EQE curve that corresponds to 210 °C. This implies that the low bandgap a-Si:H material does not contain irreversible defects. Now, considering the JV plots in 3.24 (b), it can be seen that there is a drastic improvement in the performance after annealing at 120 °C and then 150 °C. Beyond that there is only slight recovery. This is quite comparable as the results of the EQE also show that major recovery took place around 150 °C.

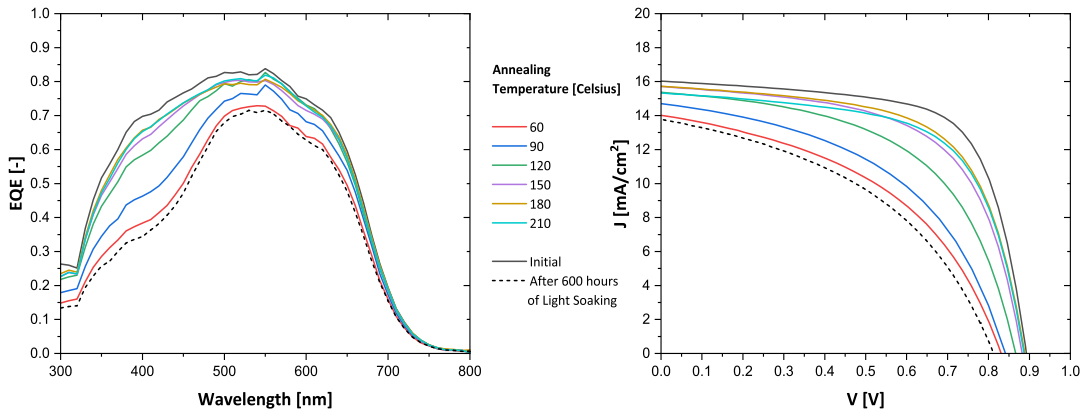

(a) EQE results **(b)** Illuminated JV results

Figure 3.25: (a) EQE plots and (b) illuminated JV plots of high bandgap a-Si:H sample after annealing

From figure 3.25 (a), it is evident that the EQE of high bandgap a-Si:H sample did not completely recover which implies that there are some defects that were irreversible through thermal annealing or it can also be called a permanent degradation. Furthermore, it can be stated that maximum recovery occurred at 180 °C after which it saturated when annealed at a temperature of 210 °C. Similar pattern is observed in the illuminated JV results.

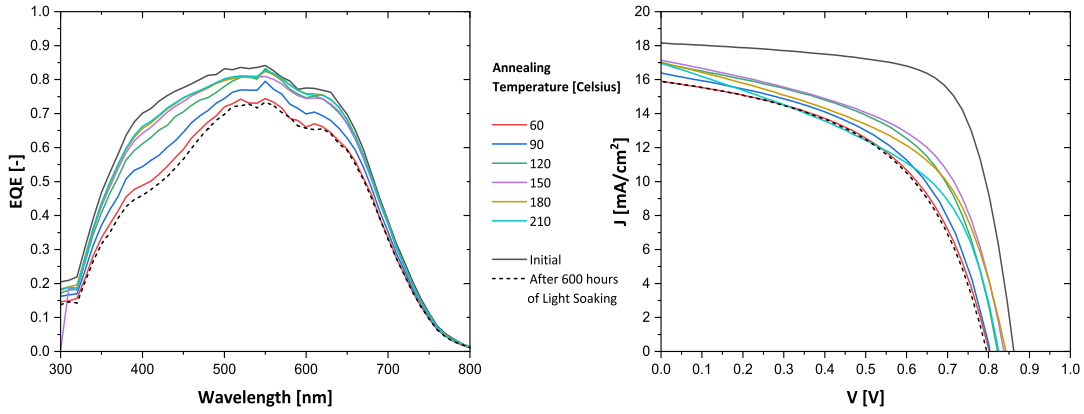

(a) EQE results **(b)** Illuminated JV results

Figure 3.26: (a) EQE plots and (b) illuminated JV plots of high/low bandgap a-Si:H sample after annealing

The EQE results of the high/low bandgap a-Si:H in figure 3.26 shows a similar recovery pattern to high bandgap a-Si:H with some permanent degradation. However, the JV plots of high/low bandgap a-Si:H sample are not reliable beyond annealing at 150 °C as the cell was shunted in the middle of the experiments. The contradictory results with respect to the recovery observed between EQE and JV results could be due to the fact that the EQE is a representation of the charge carrier collection which is not interrupted while the electrical performance is affected due to very low shunt resistance. Overall, it can be inferred from the EQE results of all samples that most of the defect creation can be reversed through thermal annealing while losing some performance due to the permanent degradation.

External parameters

The recovery of performance can be better analysed by looking at the plots of each of the external parameters to understand the temperature dependence of the reversal of SWE. Starting with the J_{sc} plots in figure 3.27, it can seen that there is a significant increase in J_{sc} of all three samples when annealed at 120 °C after which there is a gradual increase and then a saturation at 210 °C. This shows that most of reversal of defect creation occurs between 60 °C and 120 °C.

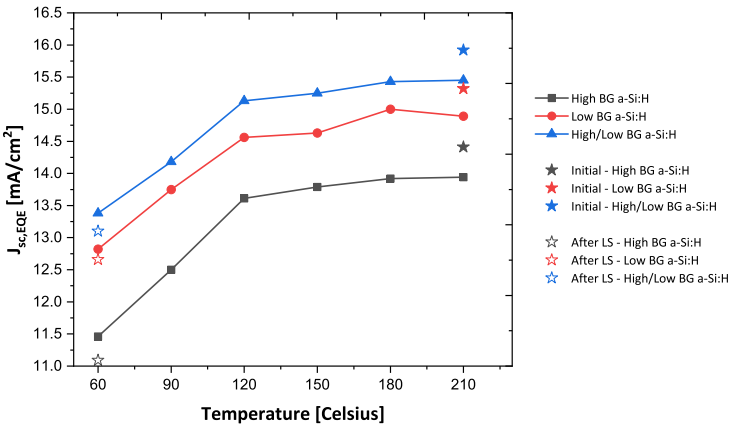

Figure 3.27: J_{sc} plots after annealing experiments

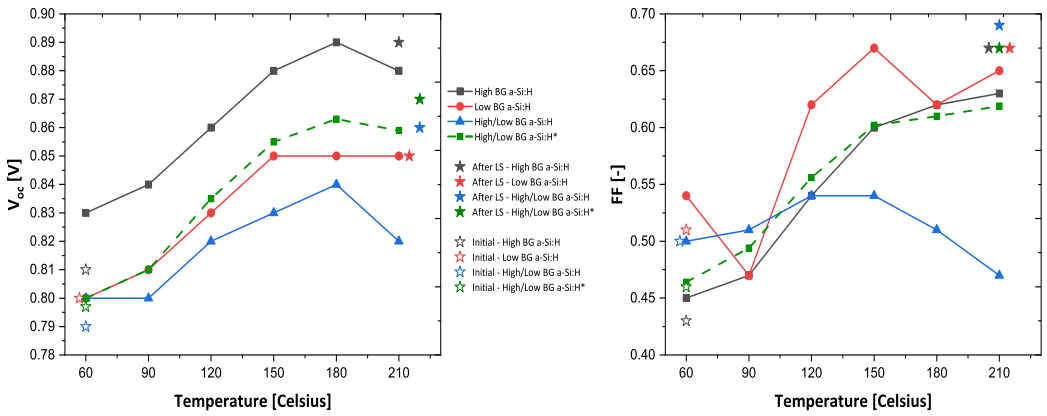

(a) V_{oc} plots **(b)** FF plots

Figure 3.28: V_{oc} and FF plots after after annealing experiments.
High/Low BG a-Si:H* correspond to the plots of a different non-shunted cell

A sharp increase in V_{oc} and FF is seen up to an annealing temperature of 150 °C and even 180 °C in some plots when analyzing the results shown in figure 3.28. This cannot be compared to the J_{sc} results, where the recovery slows down after 120°C of annealing. This might be a result of recovery of the defect formation at the p/i interface which suggests less recombination and a improved V_{oc}. It is important to note that a second plot (a green dotted line) has been added to the graphs to represent the outcomes of a different cell (cell 8) in the sample. This can be viewed as an extrapolation of the data for the high/low bandgap a-Si:H sample, as that sample was shunted in the middle of the annealing experiments. Despite not taking the absolute value into account, understanding can be gained by examining trends. Another important point to note is that there is a decrease in V_{oc} and FF after annealing at a temperature of 210 °C. This is due to the annealing temperature being higher than the deposition temperature itself, which has negatively affected the performance of the solar cells.

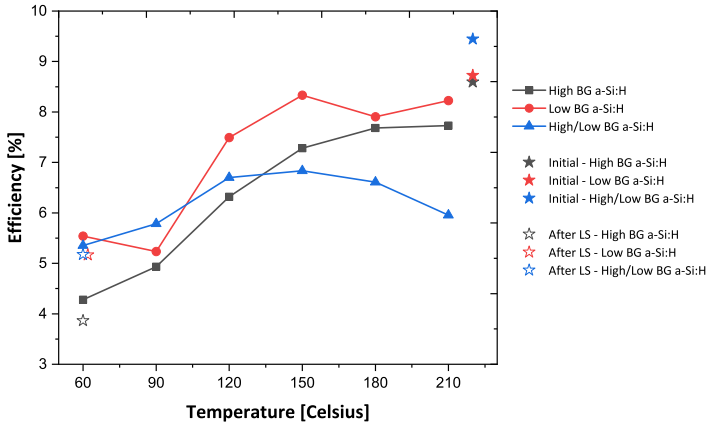

Figure 3.29: η plots after annealing experiments

The efficiency plots shown in figure 3.29 indicates that there is some permanent degradation in low BG a-Si:H and high BG a-Si:H sample. It is to be noted that the high BG sample being more defective has lost 1% in terms of absolute value while the low BG a-Si:H sample has lost <0.5%. Furthermore, the efficiency graph does not contain the extra green dashed curve (cell 8) that was used as an extrapolation for high/low bandgap a-Si:H sample. This is because the efficiency was determined using the J_{sc} from EQE, which was only measured for one of the sample's 30 cells. As a result, the efficiency could not be determined because there was no J_{sc} data for cell 8.

Series and shunt resistance

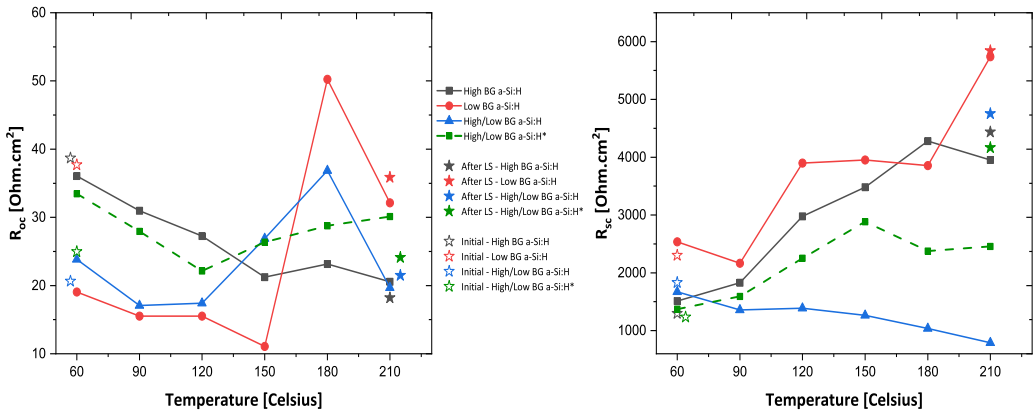

(a) R_{oc} plots **(b)** R_{sc} plots

Figure 3.30: R_{oc} and R_{sc} plots after annealing experiments.
High/Low BG a-Si:H* correspond to the plots of a different non-shunted cell

From figure 3.30, it is apparent that there is a declining trend for series resistance and an inclining trend for shunt resistance as the annealing temperature is increased from 60 to 150 °C beyond which the trends become inconsistent. No firm conclusions can be drawn based on these plots due to inconsistencies. However, there is some evidence of recovery that can be seen through the trends.

3.4.6. Raman spectroscopy analysis

Two raman spectroscopy measurements of the solar cell samples were performed in this study. First measurement was done during the initial characterisation i.e., as deposited. And the second measurement at the end of light soaking experiments. This measurement at the end of the light soaking experiments is considered here as a representation of the solar cells after a permanent degradation. The results of the measurements were analysed by fitting gaussian distributions. All the intensity values are normalised between 0 and 1. The extended range (1800-2300 cm^{-1}) of the raman spectra is only discussed as it gives information about the stretching modes. Figure 3.31 shows the normalised raman spectra of high bandgap a-Si:H, low bandgap a-Si:H and high/low bandgap a-Si:H samples in the 'as deposited state' (initial) and after permanent degradation.

Raman spectroscopy can provide information on open volume deficiencies ranging in size from divacancies to multivacancies to nanosized voids existing in the a-Si:H nanostructure by analyzing the silicon-hydride (Si-H) stretching modes. Literature shows that the Si-H stretching modes in a-Si:H can have 3 vibration modes. The characteristic vibration frequencies (ω) of the modes are known as the low stretching mode (LSM, ω: 1980–2010 cm^{-1}) indicating the presence of monohydrides, the high stretching mode (HSM, ω: 2075–2099 cm^{-1}) representing the nanosized voids, defect density and the middle stretching mode (MSM, ω: 2034–2040 cm^{-1}) that represents the presence of hydrogenated multi-vacancies that is responsible for increased bandgap in a-Si:H.

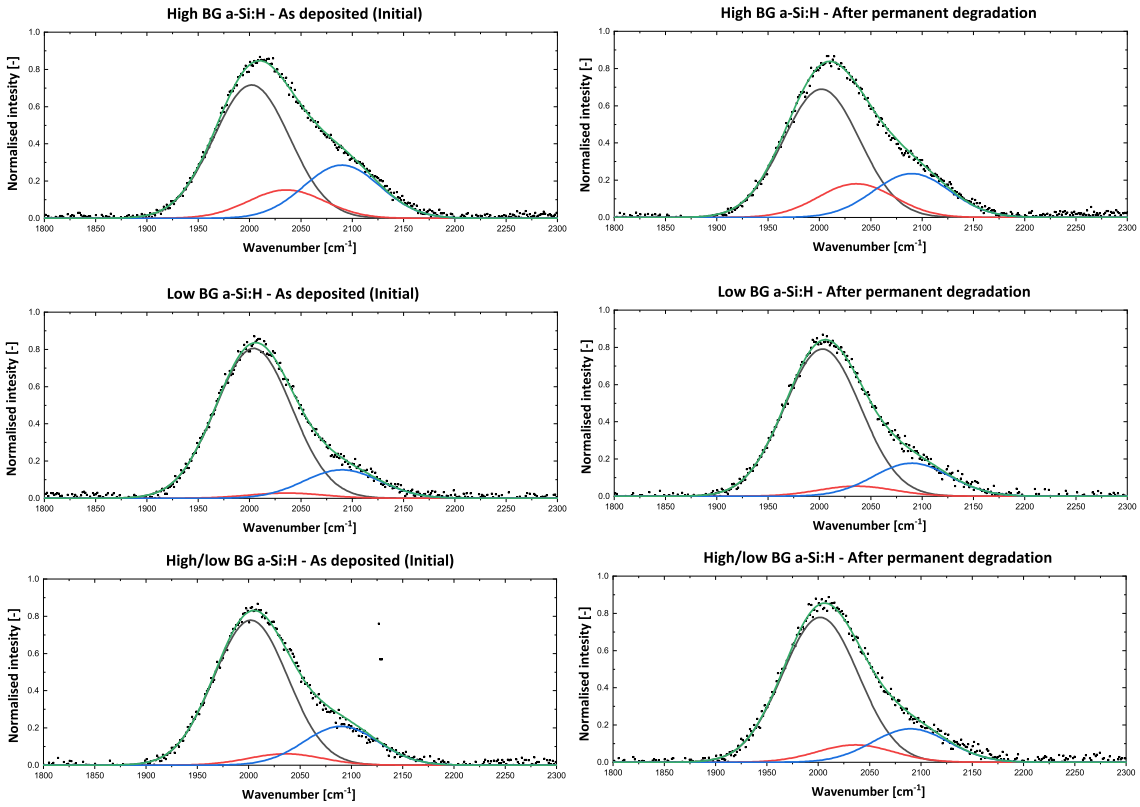

Figure 3.31: Normalised raman spectra of the solar cell samples with different qualities of a-Si:H absorber layer. Graphs on the left illustrate the initial results (as deposited). Graphs on the right illustrate the results after permanent degradation

Starting with the high bandgap a-Si:H material, the high initial MSM shift indicates the high bandgap energy of the material. Smets et al. [46] illustrated that the volumetric compressive nature of the a-Si:H matrix as a function of density and nano sized voids determines the absorptive nature and bandgap energy of the material. This must be influencing the high bandgap a-Si:H material used in this study

leading to increased bandgap. When the initial and degraded states are compared, it appears that there is a slight increase in the MSM indicating the increase in hydrogenated vacancies. Similarly, the high/low bandgap a-Si:H material also had a slight increase in MSM after permanent degradation. Furthermore, the nano sized void and defect density appears to have decreased after permanent degradation as there is a decreased HSM for both high bandgap a-Si:H and high/low bandgap a-Si:H materials. Now considering the low bandgap a-Si:H material, there is no significant difference in the stretching modes when comparing the initial and degraded states. However, very slight difference in the stretching modes could be within the limits of the error margin in the fits. As the HSM is also present in low bandgap a-Si:H material, the presence of of nanosized voids can be confirmed. From the low MSM of low bandgap a-Si:H, it is inferred that the presence of hydrogenated muti-vacancies are very minimal in the material.

Overall, it can be inferred that there is some realignment of the Si-H bonds in the a-Si:H matrix after prolonged LID, leading to permanent degradation. It was also found that increased hydrogenated multi-vacancies and decreased nanosized void and defect density in the a-Si:H bulk could have an influence in the permanent degradation of the bulk with any degree of high bandgap a-Si:H in it.

3.5. Conclusions

Based on the findings and discussions of the LID study, a number of significant conclusions can be drawn. First of all, there is a direct relationship between LID and the light soaking temperature where the degradation is stronger at low temperature (25 °C) and weaker at high temperature (in this study, it is 50 °C). This suggests that when the light soaking is done at a higher temperature, there is an active recovery of the defect creation which signifies the annealing effect.

From the EQE results, it can be inferred that there is a stronger degradation at short wavelength which implies that there could be more recombination at the front i.e., p/i interface of the device. When comparing the results of each of the samples, a significant difference in the degree of degradation can be observed. The high bandgap a-Si:H degraded the most while the degradation was comparable for low and high/low bandgap a-Si:H samples with the latter being slightly better than the former. This is due to the increased nanosized void density in the high bandgap a-Si:H bulk which degrades more when exposed to light.

The analysis of the illuminated JV characterisation-based output graphs has also demonstrated that the performance of the solar cells with low and high/low bandgap a-Si:H absorber layers was comparable, with the high/low bandgap material having the highest stabilised J_{sc} as well as the initial efficiency. This demonstrates that using a combination of high and low bandgap materials in the absorber layer has a good chance of improving stabilized efficiency. Furthermore, it was discovered that the trends of the external parameter plots indicate a gradual decline in performance during the first 10 hours of light soaking, as opposed to the concept of fast degradation, which denotes a steeply declining trend during the first 10 hours of light soaking.

According to the outcomes of the annealing study, solar cells with high and high/low bandgap a-Si:H exhibit some permanent degradation that may be caused by a high density of nanosized voids in the material. However, solar cells with low bandgap a-Si:H absorber layers are capable of attaining a complete recovery of EQE. Additionally, it was discovered that annealing at temperatures between 90 °C and 150 °C results in major recovery, whereas 180 °C results in maximum recovery.

As the degradation is stronger in the short wavelength region, it is speculated that the diffusion of boron from the p doped window layer into the a-Si:H bulk could be the dominant mechanism behind the degradation. This shall be understood by examining the stability of the buffer layer at the p-i interface under light soaking condition. A separate study has been made on the same which is be presented in chapter 4.

4

The p/i interface degradation study

4.1. Introduction

For thin-film silicon solar cells to achieve high-efficiency, excellent interface control has been thought to be of utmost importance. In both hydrogenated amorphous (a-Si:H) and nanocrystalline (nc-Si:H) silicon solar cells, the V_{oc} is typically governed by the doped layers, the mobility gap of the intrinsic material, and its bulk properties, as well as by the relative amount of recombination at the p-i interface region. Additionally, this interface may serve as a barrier against boron cross-contamination in the p-i-n configuration. Previous studies show that implementing a buffer layer at the p/i interface i.e., between the p doped layer and the intrinsic bulk layer significantly enhances the V_{oc} and conversion efficiency of the a-Si:H based solar cells [47] [48] [49]. The overall LID of an a-Si:H cell is greatly influenced by this buffer layer highlighting the significance of optimizing this interface for the stabilized state [50].

From the results of the LID study in chapter 3, it was inferred that light soaking significantly decreases the blue response due to the increased recombination at the p/i interface despite the presence of a buffer layer (i-SiO_X). This induces the need to study the significance and the stability of the buffer layer at the p/i interface through light soaking experiments.

In this chapter, single junction a-Si:H solar cell samples with buffer layers of different materials were fabricated, light soaked and characterised to examine the performance and stability of the devices. These light soaking experiments gave better insights on the significance of the material that is used as a buffer layer at the p/i interface. Additionally, the hypothesis of boron diffusion through the buffer layer into the intrinsic bulk was examined through the LID experiments of single junction a-Si:H samples with window layers deposited with 3 different B_2H_6 flow rates.

4.2. Background study

This section gives a brief overview of the background information available on the buffer layer and boron diffusion through a literature review.

4.2.1. Buffer layers and LID

i-SiO_X is reported as the best suited buffer layer to reduce the detrimental effects of localized defective regions in a-Si:H or nc-Si:H solar cells thereby increasing the V_{oc} and high stabilized efficiencies. Furthermore, the wide bandgap of i-SiO_X buffer can compensate for the band offset and lessen the back-diffusion of electrons in the p-layer for an a-Si:H cell [50]. Bugnon et al. [50] demonstrated that SiOx buffer layer can act as an efficient barrier to boron cross contamination at the p/i interface in a-Si:H solar cells thereby giving high performances and lower LID.

Matsui et al. [12] illustrated that adding an undoped a-Si:H buffer layer to single junction a-Si:H solar cells can boost the initial V_{oc} and also stabilised conversion efficiency obtained after light soaking. The a-Si:H buffer layer had a high hydrogen dilution (R = 100) and the optimal thickness of the buffer layer was found to be between 5 nm and 10 nm.

4.2.2. Boron diffusion

Boron diffusion or the boron tailing effect into the intrinsic bulk of a-Si:H solar cells can be described as the reduced charge carrier collection specifically in the blue part of the spectrum. It has been stated that this effect limits the performance of the devices that are deposited at a temperature above 200 °C. However, for enhanced current density the deposition temperature should be as high as possible, but boron tailing gets detrimental above 200 °C [51]. According to a study made by Stuckelberger et al. [51], the defect formation in the p/i interface activated by thermal energy and local energy deposition from plasma species, in combination with irreversible hydrogen effusion (in case of p type a-Si:H) is the cause of boron tailing characteristics. In case of nc-Si:H i layer growth, recombination centers were found to be created at the p/i interface due to enhanced boron diffusion at a deposition temperature above 250 °C [52].

Based on the background investigation, it is clear that a buffer layer has influence on the performance a-Si:H based solar cells. In addition, it can be observed that the significance of buffer layer on LID is also associated with the boron diffusion at the p/i interface. However, due to the limited availability of literature, there is a necessity for additional experimental studies to fully comprehend and interpret the impact of buffer layer materials and the effect of boron diffusion on the LID of a-Si:H based solar cells. Therefore, an experimental study is attempted in this chapter by observing the LID of a-Si:H single junction thin film solar cells with different buffer layers. Another separate light soaking study is additionally employed to analyse the impact of window layer doping on LID which is presented in 4.4.2.

4.3. Methodology

This section describes the methodology employed to study the degradation at the p/i interface through light soaking experiments. Firstly, the device configuration is described with the deposition conditions and a schematic of device architecture. And finally, the design of experiments is explained with a flow chart.

4.3.1. Device configuration

Single junction a-Si:H solar cell samples with superstrate p-i-n configuration consisting of 30 cells (dots) each were fabricated on ASAHI U-type commercial glass strips with predeposited SnO_2:F which acts as the transparent conductive oxide (TCO) layer. The device architecture of the samples fabricated for this study is illustrated in figure 4.1. A low bandgap a-Si:H material was used as the absorber layer for all the samples. Two sets of samples were fabricated. The first set consists of 6 devices with 5 different buffer layers each namely i-SiO_X, intrinsic hydrogenated amorphous silicon made in p chamber (i-a-Si:H), p doped hydrogenated amorphous silicon (p-aSi:H), p doped hydrogenated nanocrystalline silicon (p-ncSi:H) and p doped hydrogenated nanocrystalline silicon oxide (p-ncSiO_X:H) and the last sample being buffer-less. The second set of samples contains 3 devices with different B_2H_6 flow rates of the window (p) layer such as 10 sccm, 20 sccm and 30 sccm while having the (i-SiO_X) buffer across all 3 devices. The deposition conditions of the layers are shown in table 4.1.

Table 4.1: Processing conditions of the materials used to deposit the a-Si:H single junction p-i-n solar cell samples for the p/i interface degradation study

Layer	Power (W)	Pressure (mbar)	Temperature (°C)	Gas	Flow rate (sccm)
AZO	300	2.6	300	Ar	20
nc-SiO_X:H (p+)	12	2.2	300	SiH_4 B_2H_6 CO_2 H_2	0.8 50 1.2 170
nc-SiO_X:H (p)	12	2.2	300	SiH_4 B_2H_6 CO_2 H_2	0.8 10 2.2 170
i-SiO_X (buffer)	12	2.2	300	SiH_4 CO_2 H_2	0.8 2 170
i-aSi:H (buffer)	4	0.6	300	SiH_4 H_2	40 0
p-a-Si:H (buffer)	4	0.6	300	SiH_4 B_2H_6	40 10
p-nc-Si:H (buffer)	35	2.2	300	SiH_4 B_2H_6 H_2	0.8 20 170
p-nc-SiO_X:H (buffer)	12	2.2	300	SiH_4 B_2H_6 CO_2 H_2	0.8 10 2.2 170
Low bandgap a-Si:H (i)	2.8	0.7	300	SiH_4 H_2	40 0
nc-SiO_X:H (n)	11	1.5	300	SiH_4 PH_3 CO_2 H_2	1 10 1.2 100

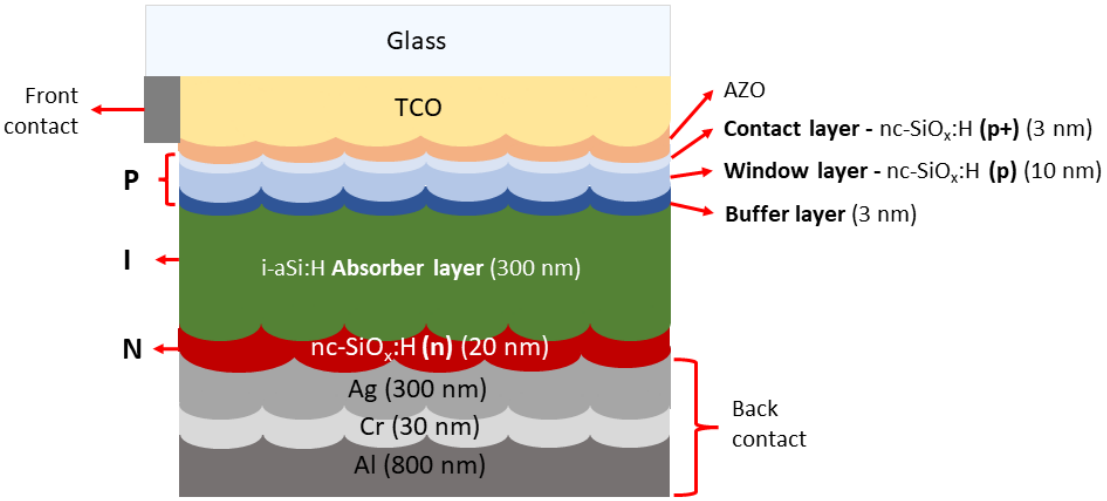

Figure 4.1: Device architecture of a-Si:H single junction solar cells used for p/i interface degradation study

4.3.2. Design of experiments

As described in the above section, two batches of samples were fabricated and subjected to light soaking. Individual investigation was done on each batch of the samples while the design of experiments is the same and straightforward for both and is depicted in a flow chart shown in figure 4.2. The initial characterisation of the samples was done after annealing the samples at 180 °C for 30 minutes. The initial characterisation includes illuminated JV, EQE and Reflectance measurements. Then the samples were subjected to light soaking at open circuit conditions at a temperature of 50 °C i.e., the temperature of the samples were maintained at 50 °C. EQE and illuminated JV measurements were performed at regular time intervals while light soaking for about 600 hours and the time periods of the data points are cumulative. Finally, the samples were annealed at 180 °C for 30 minutes to observe the reversal of the defect creation.

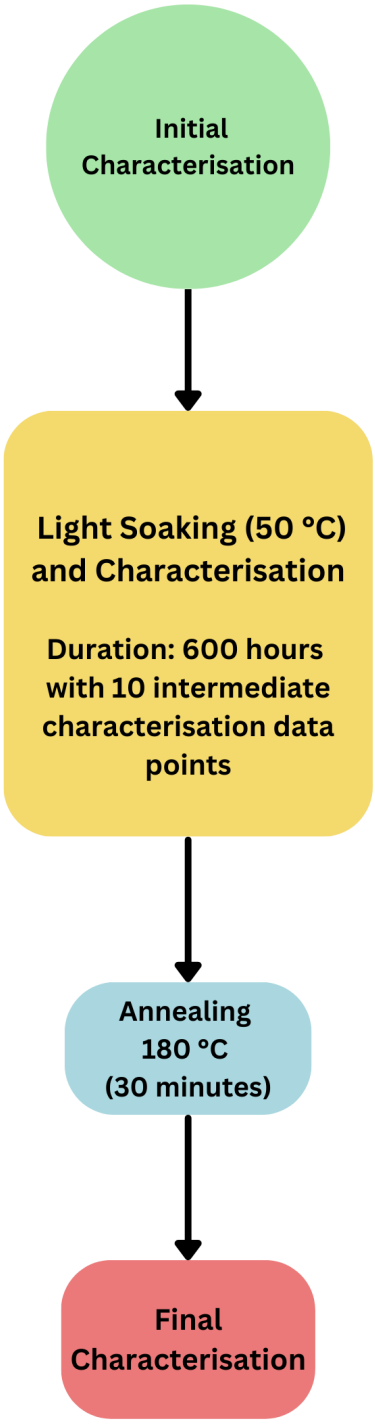

Figure 4.2: Flow chart of the design of experiments used for the p/i interface degradation study

4.4. Results and Discussion

The results and discussions of the light soaking experiments are presented in two different subsections. Firstly, the results of light soaking experiments of the samples with various buffer layers is examined and then finally the light soaking results of the samples with various window layer B_2H_6 flow rates are interpreted. It should be noted that many of the solar cells in the samples were shunted due to unanticipated events, so the characterisation was only done for one selected dot that had the best initial performance throughout the experiments.

4.4.1. Effects of buffer layer on LID

EQE characterisation

The EQE plots after light soaking 6 solar cells consisting of different buffer layer materials each were plotted against wavelength and the graphs are presented in figure 4.3. When comparing the loss in blue response of all the samples in figure 4.4, it is immediately clear that the sample with no buffer layer has the lowest response. This implies that there is an increased recombination at the p/i interface due to the absence of buffer layer.

With reference to the sample without buffer layer, similar degradation trends of EQE are observed in the sample with p-ncSi:H buffer layer. The overall degradation in p-ncSi:H is however slightly lower than the sample with no buffer which explains the significance of the buffer layer. This shall be further justified by analysing the external parameters where the performance of the sample with p-ncSi:H buffer is better than the one without buffer.

From figure 4.4, considering the samples with p-a-Si:H and p-ncSiO$_X$:H buffer, it can be observed that the degradation in the short wavelength region is comparable but the degradation in the long wavelength region is much higher than the rest of the samples. It could be a result of enhanced recombination in the bulk. It can be stated that the buffer layer has no influence on the degradation in the long wavelength region, however, the exact reason for such observation is unknown.

Examining the graphs in figure 4.3, it can be seen that the sample with i-SiO$_X$ buffer has a better initial blue response than the one with i-a-Si:H. This could be due to the defective nature of i-a-Si:H and also weak electric field at the p/i interface. Furthermore, the ΔEQE plots in figure 4.4 shows that the sample with i-SiO$_X$ buffer degraded more in the short wavelength region with little or no degradation beyond 700 nm. The sample with i-a-Si:H buffer on the other hand degraded the least in the short wavelength region compared to any other sample. The influence of this on the electrical performance is discussed by means of external parameters in the following subsections.

Since the EQE plots of 380 and 660 hours of light soaking are superimposed on one another, it is evident that the degradation has reached its saturation point in the samples with the i-SiO$_X$ and i-a-Si:H buffer layer. The EQE for the remaining samples appears to have slightly decreased after 380 hours, indicating that there may still be ongoing degradation. Most of the defect creations in all the samples were reversible which was observed through the recovery of EQE after thermal annealing at 180 °C. (refer Appendix B for the plots).

Overall, it can be stated that the samples that degraded the least in terms of EQE are the ones with i-SiO$_X$ and i-a-Si:H buffer layers. The solar cells with p doped buffer layers had severe degradation in the short wavelength region. This could be because of the buffer layers which acted as an extended p layer has led to a higher boron diffusion which has increased the recombination at the p/i interface. Similarly, Rech et al. [47] stated that the electric field in the intrinsic layer could possibly be influenced by the buffer layer and it was suggested that the buffer layer should not act as an extended p layer.

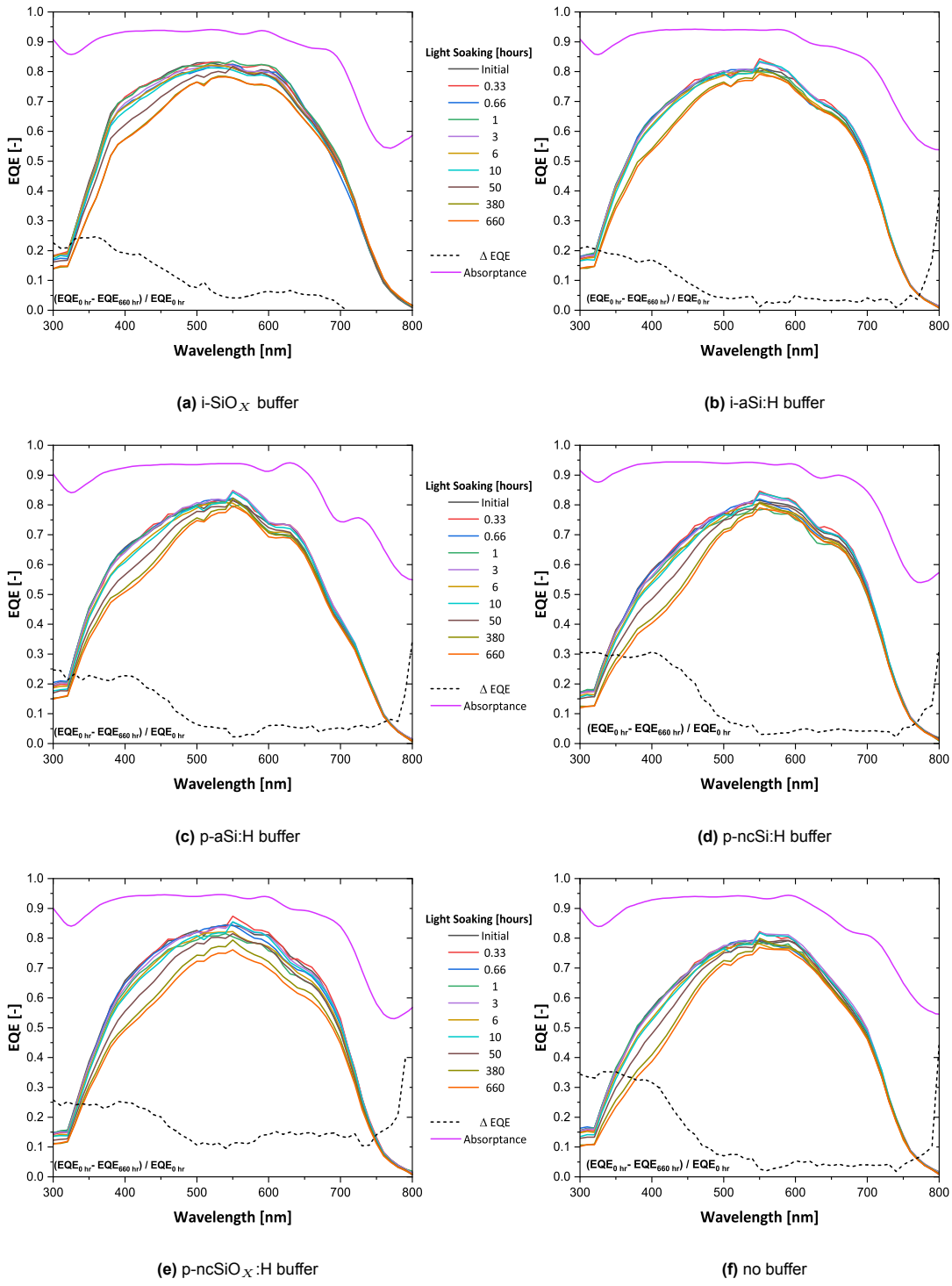

(a) i-SiO$_X$ buffer

(b) i-aSi:H buffer

(c) p-aSi:H buffer

(d) p-ncSi:H buffer

(e) p-ncSiO$_X$:H buffer

(f) no buffer

Figure 4.3: EQE and Absorptance plots of single junction a-Si:H solar cells with different buffer layers after light soaking. Buffer layers: (a) i-SiO$_X$, (b) i-a-Si:H, (c) p-aSi:H (d) p-ncSi:H (e) p-ncSiO$_X$:H and (f) no buffer

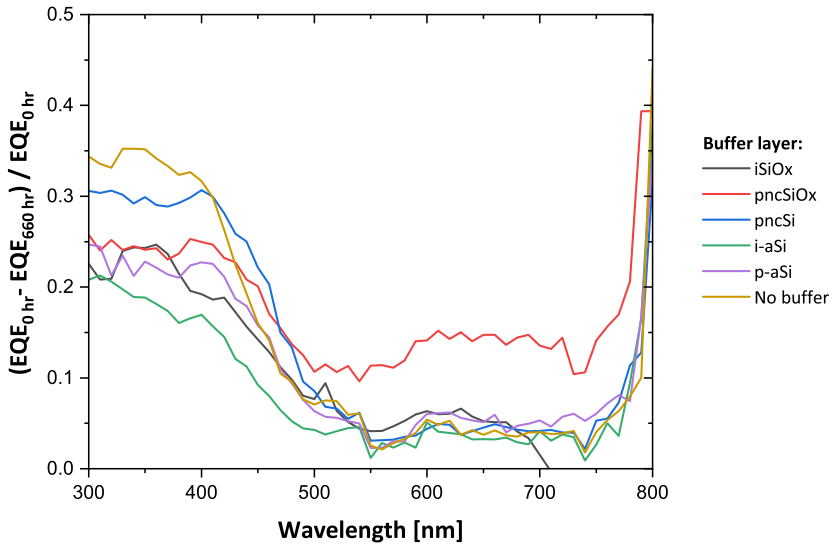

Figure 4.4: ΔEQE plots of single junction a-Si:H samples with different buffer layers after light soaking

Illuminated JV characterisation

The illuminated JV plots after light soaking 6 different solar cells consisting of different buffer layer materials each are presented in figure 4.5. As mentioned in the previous chapter,R_{oc} and R_{sc} values obtained from the illuminated JV measurement are not greatly reliable, thus the JV curves are shown as an overview in this section which can be utilised to observe the trends.

When comparing the results of all samples, it is evident that the solar cell with p-ncSiO$_X$:H buffer has degraded the most which can be observed in the JV curve that corresponds to 660 hours of light soaking. Significant increase in R_{oc} and drastic decrease in R_{sc} has affected the FF of the cell to a greater extent. This can be explained by the increased recombination at the p/i interface due to boron diffusion as the p-ncSiO$_X$:H buffer is acting as an extend p layer. It is to be noted that despite the low initial performance, the degradation in the sample with no buffer is found to be lower than the sample with p-ncSiO$_X$:H. This suggests that an extended p layer can have detrimental effects on the performance of the solar cells under light soaking conditions. Overall, it shall be inferred that the R_{oc} has increased and R_{sc} has decreased which eventually affected the FF of all the samples. Further interpretations on the absolute values of the external parameters are made in the following subsections.

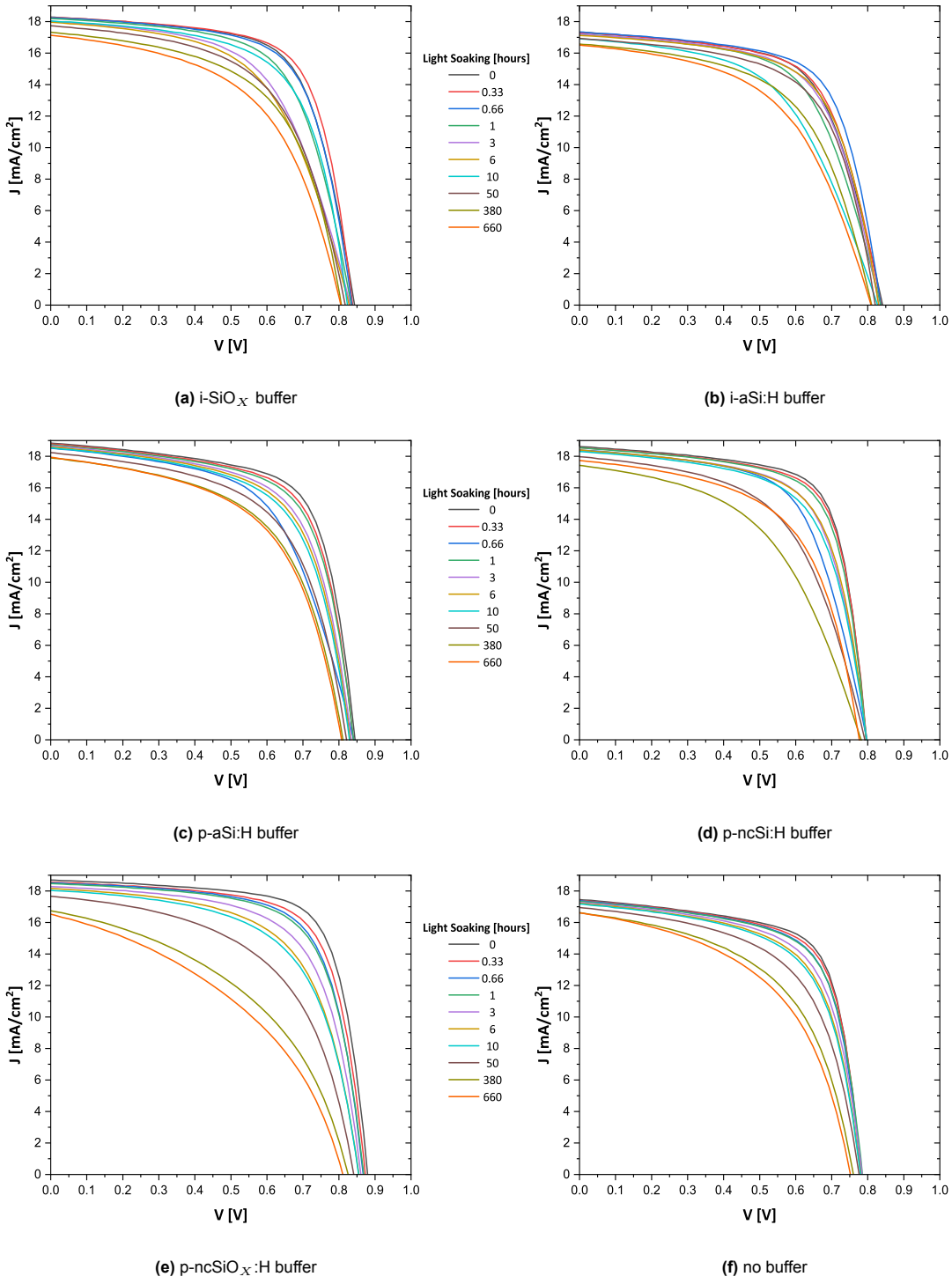

(a) i-SiO$_X$ buffer

(b) i-aSi:H buffer

(c) p-aSi:H buffer

(d) p-ncSi:H buffer

(e) p-ncSiO$_X$:H buffer

(f) no buffer

Figure 4.5: Illuminated JV plots of single junction a-Si:H solar cells with different buffer layers after light soaking. Buffer layers: (a) i-SiO$_X$, (b) i-a-Si:H, (c) p-aSi:H (d) p-ncSi:H (e) p-ncSiO$_X$:H and (f) no buffer

External parameters

Figure 4.6 and 4.7 depicts the change in external parameters i.e., J_{sc}, V_{oc}, FF and η after light soaking.

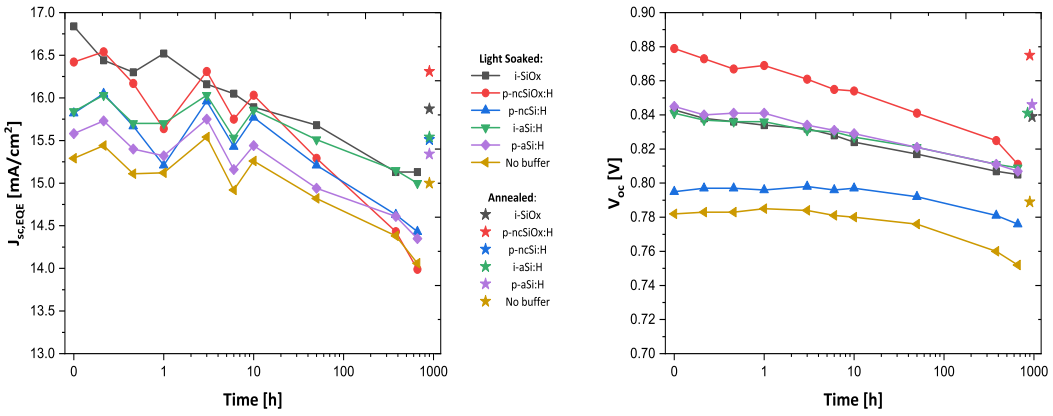

(a) J_{sc} plots **(b)** V_{oc} plots

Figure 4.6: J_{sc} and V_{oc} variation of single junction a-Si:H samples with different buffer layers after light soaking

From figure 4.6 (a), the degradation appears to be more severe in the solar cell with p-ncSiO$_X$:H buffer layer. This is indeed in line with the observations made in the previous sections. Apart from that sample, the rest of the samples have similar degradation trends which are gradually declining in the first 10 hours of light soaking and significantly decreasing beyond 10 hours of light soaking. Similar degradation trends of J_{sc} were observed in the previous chapter. This is assumed to be due to the light induced activation of recombination centres through boron diffusion after the first 10 hours of light soaking.

The values of J_{sc} after 660 hours of light soaking shows that the samples with i-SiO$_X$ and i-a-Si:H buffer layers are giving relatively higher performance compared to the samples with doped and no buffer layer. When comparing the initial values, the sample with i-SiO$_X$ buffer is significantly higher than the one with i-a-Si:H. Though the reason behind such a severe degradation of the sample with i-SiO$_X$ in the first 10 hours of light soaking is unknown, it can be assumed that there is an irresistible boron diffusion despite the presence of i-SiO$_X$ buffer which needs to be studied further. While i-a-Si:H buffer seems to be relatively stable in the first 10 hours, it is assumed that the dangling bonds in the material could aid in trapping of boron to a certain extent after which the diffusion is irresistible. Examining the data points after thermal annealing, it can be clearly observed that most of the samples did not have a complete recovery while the sample with p-ncSiO$_X$:H buffer layer had the highest J_{sc} recovery.

From the trends of the V_{oc} plots shown in figure 4.7 (b), it is immediately clear that the solar cell with p-ncSiO$_X$:H buffer layer had the highest initial V_{oc} due to high dopant concentration and bandgap of the p layer stack. However, after 660 hours of light soaking it has reached the same value of V_{oc} as the samples with i-SiO$_X$, i-a-Si:H and p-aSi:H buffer layers. Furthermore, the declining V_{oc} trends of the samples with i-SiO$_X$, i-a-Si:H and p-a-Si:H buffer layers shows that the internal electric field at the p/i interface gets affected due to LID as the boron diffusion takes place.

It is important to note that V_{oc} plots of the sample with no buffer has the lowest initial value and shows no sign of degradation in the first 10 hours of light exposure and a gradual decrease beyond that. This is due to the absence of the buffer layer which lacks an additional electric field at the p/i interface which boosts the built in voltage. Furthermore, the results of thermal annealing at 180 °C shows a complete recovery of V_{oc} in most of the samples. It should be noted that the post annealing data point of the sample with p-ncSi:H is unavailable as the cell got shunted after annealing.

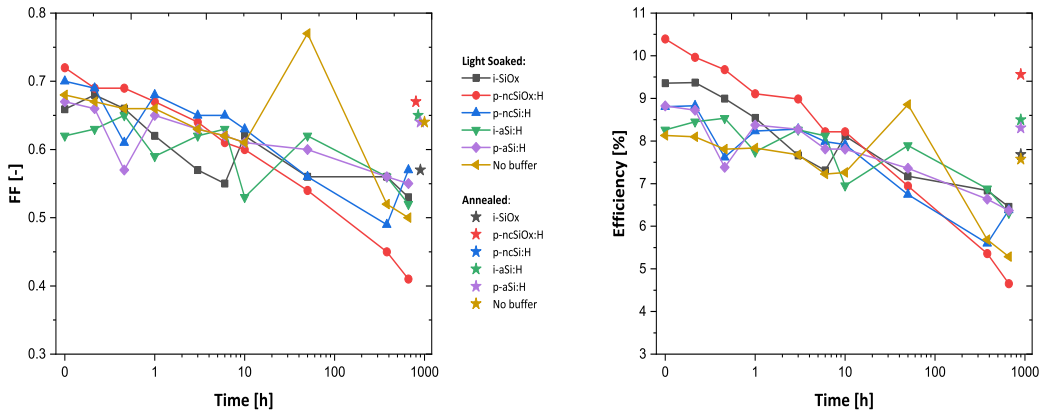

(a) FF plots **(b)** η plots

Figure 4.7: FF and η variation of single junction a-Si:H samples with different buffer layers after light soaking

The FF and η plots shown in figure 4.7 appears to have similar trends for all the samples as the V_{oc} and J_{sc}. There are some inconsistencies and outliers in the trends due to measurement errors which are to be ignored. Nevertheless, most of the plots show a common declining trend where most of the trends are intertwined with each other. Though no specific statements can be made, the samples with i-a-Si:H, p-aSi:H and i-SiO_X buffer layers which were the most discussed, appears to have a relatively higher efficiency after 660 hours of light soaking while the sample with p-ncSiO_X:H buffer layer degraded the most and has a linear declining trend.

According to the findings of the aforementioned study, a buffer layer present at the p/i interface definitely contributes to a solar cell's initial and stabilized performance when compared to a solar cell lacking a buffer layer. Devices with three different buffer layers: i-SiO_X, i-a-Si:H, and p-aSi:H were found to have comparable performance in the degraded state despite having a relatively good initial performance. This limits the ability to draw any firm conclusions. As a result, it can be said that i-SiO_X, i-a-Si:H, and p-aSi:H are potential candidates for a buffer layer that need to be further studied.

4.4.2. Effects of window layer (p) doping on LID

In this subsection the outcomes of the light soaking experiments conducted on 3 different single junction a-Si:H samples with a window p layer B_2H_6 flow rate of 10 sccm, 20 sccm and 30 sccm respectively are discussed.

EQE and Illuminated JV characterisation

When comparing the EQE results of all 3 samples in figure 4.8, it is notable that there is no significant difference in the degradation trend of the samples. However looking at the ΔEQE plots in figure 4.9, it can be observed that the sample with the highest B_2H_6 flow rate of 30 sccm had a slightly higher degradation in short wavelength region. This reduction in the EQE can be due to the thicker window layer obtained as result of high diborane concentration. After thermal annealing at 180 °C for 30 minutes, major recovery was observed while noting that there was also some permanent degradation. (refer appendix B.1.2 for the EQE plots). The evolution of the illuminated JV plots are also in line with the EQE plots for all three samples which implies no significant degradation with respect to the changing window layer B_2H_6 flow rates. Further inspection is done by interpreting the external parameter plots in the following subsection.

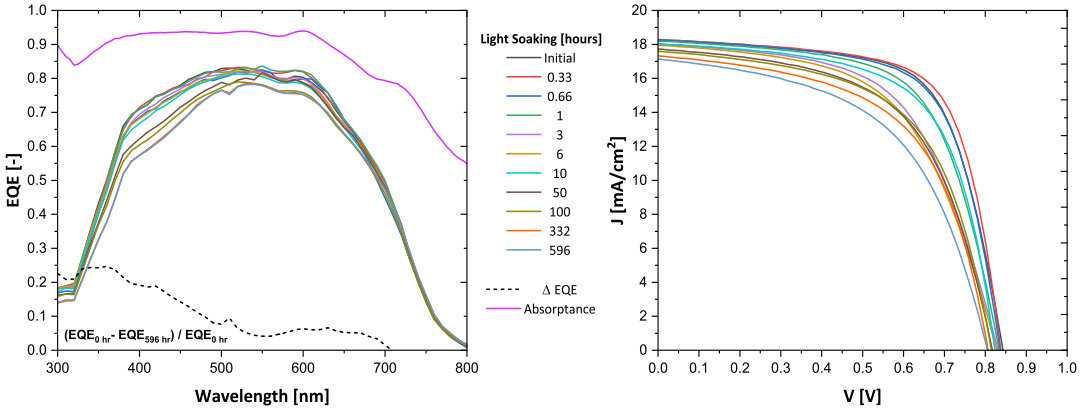

(a) EQE: B_2H_6 - 10 sccm

(b) JV: B_2H_6 - 10 sccm

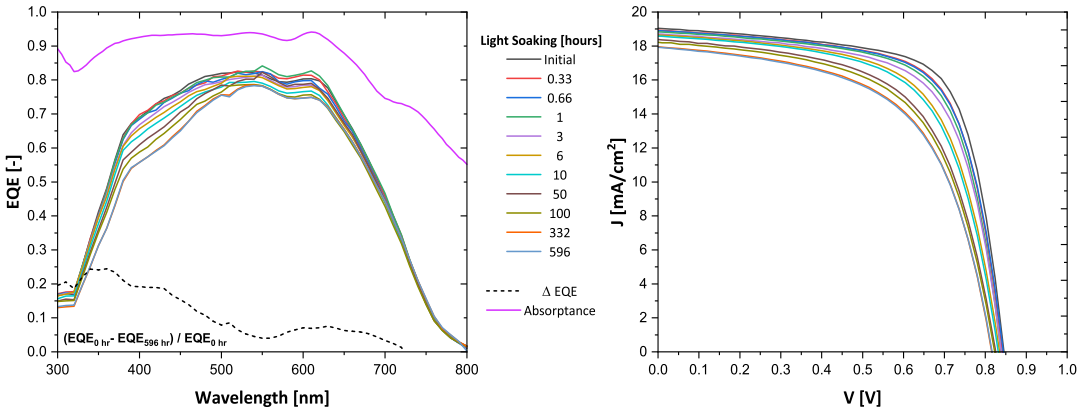

(c) EQE: B_2H_6 - 20 sccm

(d) JV: B_2H_6 - 20 sccm

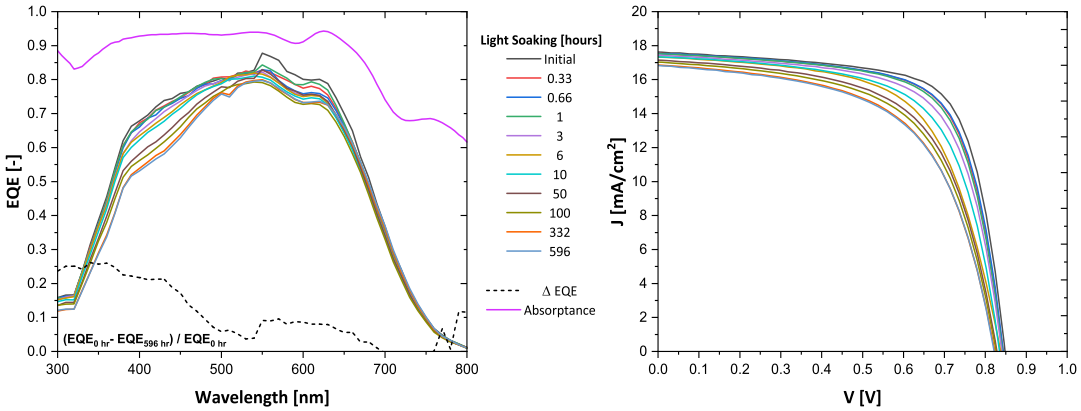

(e) EQE: B_2H_6 - 30 sccm

(f) JV: B_2H_6 - 30 sccm

Figure 4.8: EQE and illuminated JV plots of single junction a-Si:H samples with a window layer B_2H_6 flowrate of (a) 10 sccm, (b) 20 sccm and (c) 30 sccm after light soaking

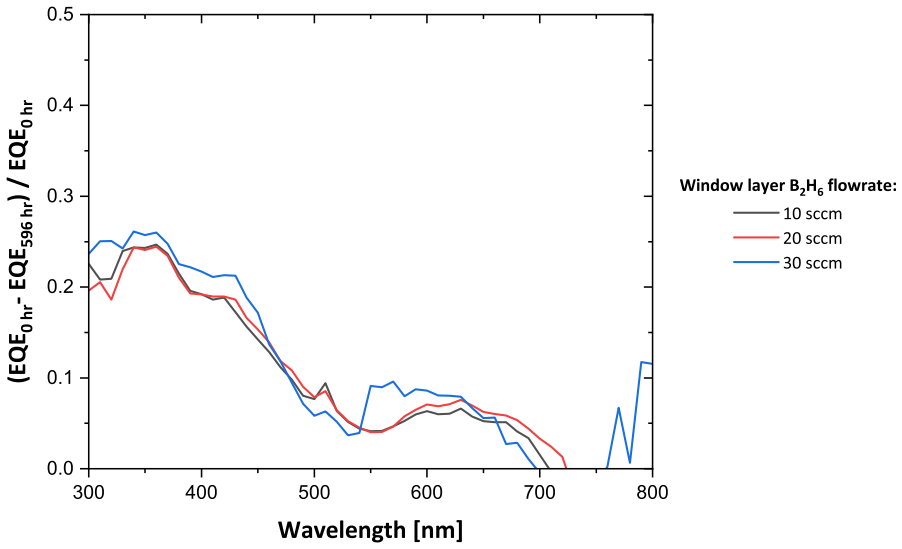

Figure 4.9: ΔEQE plots of single junction a-Si:H samples with different window layer B_2H_6 flow-rates after light soaking

External parameters

Figure 4.6 and 4.7 depicts the change in external parameters i.e., J_{sc}, V_{oc}, FF and η after light soaking.

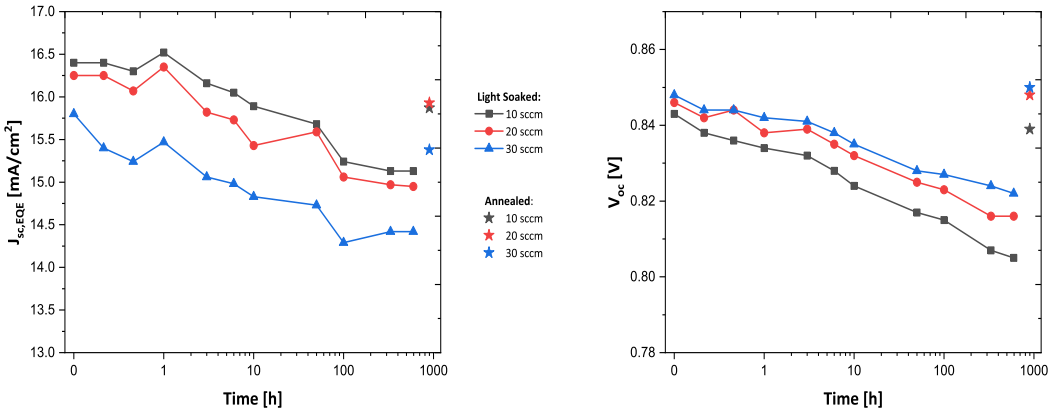

(a) J_{sc} plots

(b) V_{oc} plots

Figure 4.10: J_{sc} and V_{oc} variation of single junction a-Si:H samples with different window layer B_2H_6 flow-rates after light soaking

From the J_{sc} plots, similar trends with some marginal difference can be observed for the samples with 10 sccm and 20 sccm B_2H_6 flow rates. However, the sample with 30 sccm B_2H_6 flow rate has a lower initial value which could be a result of parasitic absorption due to a thicker p layer obtained from high B_2H_6 concentration. It is clear from the annealing results that none of the samples had a full recovery of J_{sc}, which denotes permanent degradation. The V_{oc} plots on the other hand show a reverse order of the trends observed in the J_{sc} plots. While the differences are still marginal, the sample with 30 sccm B_2H_6 flow-rate had the lowest degradation which could be a result of high internal electric field due to high doping concentration of the window p layer.

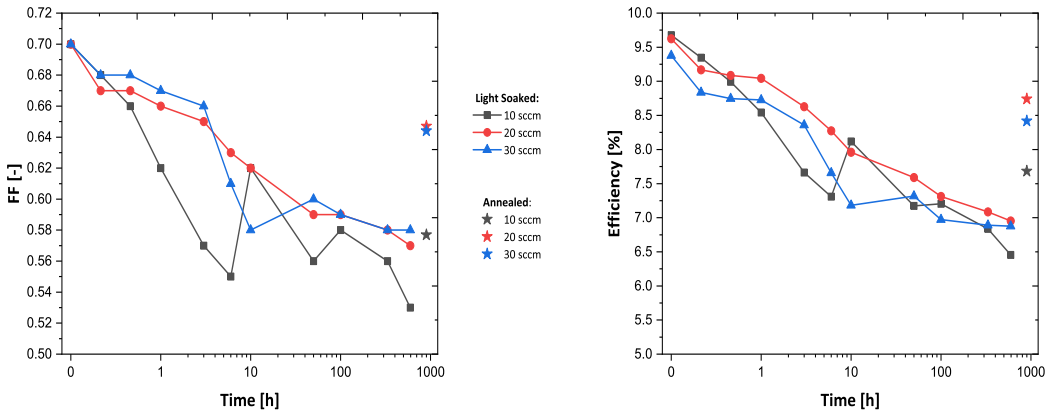

(a) J_{sc} plots **(b)** V_{oc} plots

Figure 4.11: FF and η variation of single junction a-Si:H samples with different window layer B_2H_6 flow-rates after light soaking

The FF and η plots in figure 4.11 also display similar declining trends for all the samples. According to the FF plots, it can be seen that all samples have the same initial value, but the samples with B_2H_6 flow rates of 20 sccm and 30 sccm appear to be superior to those with 10 sccm. It should be noted, however, that some inconsistency in the trend of the sample with 10 sccm B_2H_6 is caused by measurement errors. The η plots show extremely marginal difference in the initial as well as the degraded values which indicates that the change in B_2H_6 flow rate of the window layer has no significant impact on the efficiency after LID. Furthermore, the results after annealing at 180 °C shows that none of the samples had a complete recovery which indicates a permanent degradation. Such a permanent degradation is speculated to be a result of partial shunting or irreversible boron diffusion but the exact reason is unknown.

4.5. Conclusions

According to the outcomes of experiments on the effects of buffer layer on LID, it is inferred that implementing a buffer layer at the p/i interface can have a significant influence on the initial as well as stabilised performance of a-Si:H solar cells. Additionally, it was also found that the type of material that is used as a buffer layer also has an influence on the initial and stabilised performance of the device. However, no firm conclusion could be drawn on the material that gives the best stabilised performance. This was due to various reasons such as inconsistencies in the trends, lack of error bars (due to numerous shunted cells in all the samples) and also the observation of marginal difference in performance of the solar cells. Therefore, it can only be stated that i-SiO_X, i-a-Si:H, and p-aSi:H are some of the potential candidates for a buffer layer in an a-Si:H solar cell that could improve the stabilised performance.

Based on the results of the experiments on the effects of window layer (p) doping on LID, it was found that there is no sign of correlation between the doping concentration of the window (p) layer and LID due to boron diffusion through the p/i interface. Therefore, the recombination at the p/i interface might be a result of some other defect creation mechanism.

5

Conclusions and Recommendations

5.1. Conclusions

Several substantial conclusions were drawn based on the findings of the experimental studies conducted in this thesis. Following is a list of conclusions, which are categorized according to the research questions posed in the introduction.

1. **How does light soaking affect the performance and stability of solar cells with different qualities of a-Si:H absorber layer?**

   Based on the findings of EQE and illuminated JV characterisation, it was concluded that the absorber layer with high bandgap a-Si:H material degraded the most while the degree of degradation of low bandgap and high/low bandgap a-Si:H material was comparable with the latter being slightly lower than the former. Such an observation was due to the high nanosized void density in the high bandgap a-Si:H material which has proven to have strong LID. Despite the comparable performance observed in the solar cell with low bandgap a-Si:H and high/low bandgap a-Si:H absorber layers, it is worth noting that the high/low bandgap a-Si:H solar cell, however, had the highest stabilized J_{sc} and initial efficiency. This indicates that further optimisation of the high/low bandgap absorber layer could increase the chance of attaining improved stabilised efficiency.

   Furthermore, the EQE characterisation results revealed that there is a stronger degradation at the short wavelength range (350-500 nm) irrespective of the quality of a-Si:H absorber layer. This was a result of increased recombination at the p/i interface of the solar cell.

   Additionally, it was discovered that there is a direct correlation between the degradation and the light soaking temperature as the light soaking experiments were carried out at two different temperatures, 25 °C and 50 °C. The degradation was found to be weaker due to the active recovery of defect creation (annealing effect) when light soaked at 50 °C.

2. **To what extent can thermal annealing recover the performance of degraded solar cells with different qualities of a-Si:H absorber layer?**

   The EQE results of the annealing study show that solar cells with high bandgap a-Si:H and high/low bandgap exhibit some permanent degradation, which may be brought on by a high density of nano sized voids in the material. Solar cells with low bandgap a-Si:H absorber layers can, however, achieve a full recovery of EQE. Further investigations revealed that major recovery occurs during annealing at temperatures between 90°C and 150°C, while maximum recovery occurs at 180°C.

3. **What is the significance of buffer layer at the p/i interface and how does it affect the performance and stability of a-Si:H solar cells?**

   It has been demonstrated from the light soaking study that adding a buffer layer to the p/i interface can have a significant impact on the initial as well as stabilized performance of a-Si:H solar cells. Additionally, it was discovered that the buffer layer's material selection has an impact on both initial and stabilized performance of the solar cells. However, the material that offers the best stabilised performance could not be chosen due to inconsistency in trends of the resulting plots. Therefore, it is only possible to state that i-SiO_X, i-a-Si:H, and p-aSi:H are some of the potential candidates for a buffer layer in an a-Si:H solar cell that could possibly improve the stabilized performance.

4. **Is there a relationship between LID and the window layer doping concentration?**

   According to the findings of the light soaking experiments, there is no indication of a correlation between the doping concentration of the window (p) layer and LID. This makes the hypothesis of boron diffusion originating from window (p) layer to be invalid. Furthermore, it is speculated that the increased recombination at the p/i interface could also be caused by another defect creation mechanism which is still unknown.

5.2. Recommendations

Numerous significant findings were obtained from the experiments performed in this thesis. However, there is always scope for improvement. Many more concrete conclusions may have been drawn if the data had been free of uncertainty. Therefore, the following recommendations are provided to improve the reliability and precision of the results and also for further research openings.

To begin with, eliminating the shunting issue of the solar cell samples considerably improves data dependability. There are two different viewpoints on how the cells were getting shunted. On the one hand, it could be owing to a fault in the measuring setup, where the probes are scratching the solar cell's back contact. On the other hand, it could be due to impurities in the deposition that cause cell shunting later on. Solving such problems could greatly improve the accuracy of the results as the error bars can be included in the graphs.

In order to have better insights on recombination in the solar cells, the EQE measurements can be performed under reverse bias conditions.

With respect to the LID study of different qualities of a-Si:H, the solar cell with a combination of high and low bandgap a-Si:H material as absorber layer appeared to be promising. More insights can be acquired by further optimisation to achieve better stabilised efficiency.

As the trends of the external parameter plots appear to contradict the patterns which define the fast and slow degradation regimes, more insights on the variation in the pattern can be obtained by conducting further studies on solar cells with different materials as p doped layer.

Considering the findings of the study on the effect of buffer layer on LID, a better conclusion may be reached by varying the thickness of the buffer layer and studying the performance of the solar cells under light soaking conditions.

Bibliography

[1] J. Jaeger, *Explaining the exponential growth of renewable energy*, Sep. 2021. [Online]. Available: https://www.wri.org/insights/growth-renewable-energy-sector-explained.

[2] *Types of photovoltaic cells - Energy Education — energyeducation.ca*, [Accessed 02-Jun-2023]. [Online]. Available: https://energyeducation.ca/encyclopedia/Types_of_photovoltaic_cells#cite_note-peake-3.

[3] M. Casini, *Smart buildings: Advanced materials and nanotechnology to improve energy-efficiency and environmental performance*. Woodhead Publishing, 2016.

[4] J. Svarc, *Most efficient solar panels 2023*, Jun. 2023. [Online]. Available: https://www.cleanenergyreviews.info/blog/most-efficient-solar-panels.

[5] C. Solar, *Which Photovoltaic Cells Are Best? 7 Reasons to Pick Thin Film and C-Si - Coastal Solar — coastalsolar.com*, [Accessed 02-Jun-2023]. [Online]. Available: https://coastalsolar.com/photovoltaic-cells-pros-cons-crystalline-thin-film-solar-panels/.

[6] E. T. Efaz, M. M. Rhaman, S. Al Imam, *et al.*, "A review of primary technologies of thin-film solar cells," *Engineering Research Express*, vol. 3, no. 3, p. 032 001, 2021.

[7] T. D. Lee and A. U. Ebong, "A review of thin film solar cell technologies and challenges," *Renewable and Sustainable Energy Reviews*, vol. 70, pp. 1286–1297, 2017.

[8] K. Chopra, P. Paulson, and V. Dutta, "Thin-film solar cells: An overview," *Progress in Photovoltaics: Research and applications*, vol. 12, no. 2-3, pp. 69–92, 2004.

[9] *Thin-Film Solar Panels: An In-Depth Guide | Types, Pros & Cons — solarmagazine.com*, [Accessed 05-Jun-2023]. [Online]. Available: https://solarmagazine.com/solar-panels/thin-film-solar-panels/.

[10] A. H. Smets, K. Jäger, O. Isabella, R. A. Swaaij, and M. Zeman, *Solar Energy: The physics and engineering of photovoltaic conversion, technologies and systems*. UIT Cambridge, 2015.

[11] A. Lambertz, F. Finger, R. E. Schropp, U. Rau, and V. Smirnov, "Preparation and measurement of highly efficient a-si: H single junction solar cells and the advantages of μc-siox: H n-layers," *Progress in Photovoltaics: Research and Applications*, vol. 23, no. 8, pp. 939–948, 2015.

[12] T. Matsui, K. Maejima, A. Bidiville, *et al.*, "High-efficiency thin-film silicon solar cells realized by integrating stable a-si: H absorbers into improved device design," *Japanese Journal of Applied Physics*, vol. 54, no. 8S1, 08KB10, 2015.

[13] J. S. Cashmore, M. Apolloni, A. Braga, *et al.*, "Record 12.34% stabilized conversion efficiency in a large area thin-film silicon tandem (micromorph™) module," *Progress in Photovoltaics: Research and Applications*, vol. 23, no. 11, pp. 1441–1447, 2015.

[14] H. Tan, E. Moulin, F. T. Si, *et al.*, "Highly transparent modulated surface textured front electrodes for high-efficiency multijunction thin-film silicon solar cells," *Progress in Photovoltaics: Research and Applications*, vol. 23, no. 8, pp. 949–963, 2015.

[15] H. Solar, *HyET Group | HyET Solar — hyetsolar.com*, [Accessed 05-Jun-2023]. [Online]. Available: https://www.hyetsolar.com/.

[16] M. Stuckelberger, R. Biron, N. Wyrsch, F.-J. Haug, and C. Ballif, "Progress in solar cells from hydrogenated amorphous silicon," *Renewable and Sustainable Energy Reviews*, vol. 76, pp. 1497–1523, 2017.

[17] M. Zeman. "Solar cells." (2016), [Online]. Available: https://ocw.tudelft.nl/wp-content/uploads/Solar-Cells-R5-CH7_Thin_film_Si_solar_cells.pdf.

[18] K. S. Oppedal, "A study of the staebler-wronski effect and amorphous silicon solar cells," 2013.

[19] L. Yang and L.-F. Chen, “The effect of h2 dilution on the stability of a-si: H based solar cells,” *MRS Online Proceedings Library (OPL)*, vol. 336, 1994.

[20] M. Schouten, “The nanostructure of hydrogenated amorphous silicon, examined by means of thermal annealing and light soaking,” 2013.

[21] J. Melskens, S. W. Eijt, M. Schouten, *et al.*, “Migration of open volume deficiencies in hydrogenated amorphous silicon during annealing,” *IEEE Journal of Photovoltaics*, vol. 7, no. 2, pp. 421–429, 2017.

[22] M. Fischer, H. Tan, J. Melskens, R. Vasudevan, M. Zeman, and A. H. Smets, “High pressure processing of hydrogenated amorphous silicon solar cells: Relation between nanostructure and high open-circuit voltage,” *Applied Physics Letters*, vol. 106, no. 4, p. 043 905, 2015.

[23] A. Smets and M. Van De Sanden, “Relation of the si□ h stretching frequency to the nanostructural si□ h bulk environment,” *Physical Review B*, vol. 76, no. 7, p. 073 202, 2007.

[24] R. E. Schropp, M. Zeman, *et al.*, *Amorphous and microcrystalline silicon solar cells: modeling, materials and device technology*. Springer, 1998, vol. 8.

[25] A. Smets. “Pv2x solar energy engineering: Photovoltaic technologies.” (2017), [Online]. Available: `https://delftxdownloads.tudelft.nl/PV2x/4.1.1/PV2x_2017_4.1.1_Amorphous_silicon-slides.pdf`.

[26] 1. L. Staebler and C. Wronski, “Reversible conductivity changes in discharge-produced amorphous si,” *Applied physics letters*, vol. 31, no. 4, pp. 292–294, 1977.

[27] D. Staebler and C. R. Wronski, “Optically induced conductivity changes in discharge-produced hydrogenated amorphous silicon,” *Journal of Applied Physics*, vol. 51, no. 6, pp. 3262–3268, 1980.

[28] A. Smets, “Photovoltaic technologies course, lecture slides,” 2023.

[29] P. Babál, “Doped nanocrystalline silicon oxide for use as (intermediate) reflecting layers in thin-film silicon solar cells,” 2014.

[30] P. Hierrezuelo-Cardet, A. F. Palechor-Ocampo, J. Caram, *et al.*, “External quantum efficiency measurements used to study the stability of differently deposited perovskite solar cells,” *Journal of Applied Physics*, vol. 127, no. 23, p. 235 501, 2020.

[31] R. Van Swaaij, “Photovoltaic technologies course, lecture slides,” 2023.

[32] M. Stuckelberger, “Hydrogenated amorphous silicon: Impact of process conditions on material properties and solar cell efficiency,” *Ecole Polytechnique Federale de Lausanne: Neuchâtel, Switzerland*, 2014.

[33] T. Matsui, H. Sai, K. Saito, and M. Kondo, “High-efficiency thin-film silicon solar cells with improved light-soaking stability,” *Progress in Photovoltaics: Research and Applications*, vol. 21, no. 6, pp. 1363–1369, 2013.

[34] A. Klaver and R. Van Swaaij, “Modeling of light-induced degradation of amorphous silicon solar cells,” *Solar Energy Materials and Solar Cells*, vol. 92, no. 1, pp. 50–60, 2008.

[35] Á. Caballero Lorenzo, “Optimization of hydrogenated amorphous silicon for its use in different photovoltaic technologies,” 2016.

[36] T. Shimizu, “Staebler-wronski effect in hydrogenated amorphous silicon and related alloy films,” *Japanese journal of applied physics*, vol. 43, no. 6R, p. 3257, 2004.

[37] 7. Stutzmann, W. Jackson, and C. Tsai, “Light-induced metastable defects in hydrogenated amorphous silicon: A systematic study,” *Physical Review B*, vol. 32, no. 1, p. 23, 1985.

[38] H. M. Branz, “Hydrogen collision model: Quantitative description of metastability in amorphous silicon,” *Physical Review B*, vol. 59, no. 8, p. 5498, 1999.

[39] J. Melskens, “Hydrogenated amorphous silicon: Nanostructure and defects,” 2015.

[40] J. Melskens, N. J. Podraza, and M. E. Stuckelberger, “Infrared optical properties: Hydrogen bonding and stability,” in *The World Scientific Reference of Amorphous Marterials: Structure, Properties, Modeling and Main Applications: Volume 3 Structure, Properties, and Applications of Tetrahedrally Bonded Thin-Film Amorphous Semiconductors*, World Scientific, 2021, pp. 85–128.

[41] S. Guha, J. Yang, A. Banerjee, B. Yan, and K. Lord, “High quality amorphous silicon materials and cells grown with hydrogen dilution,” *Solar energy materials and solar cells*, vol. 78, no. 1-4, pp. 329–347, 2003.

[42] G. van Elzakker, “Hydrogenated amorphous silicon solar cells deposited from silane diluted with hydrogen,” 2010.

[43] J. Wienke, B. Van Der Zanden, M. Tijssen, and M. Zeman, “Performance of spray-deposited zno: In layers as front electrodes in thin-film silicon solar cells,” *Solar Energy Materials and Solar Cells*, vol. 92, no. 8, pp. 884–890, 2008.

[44] P.-K. Chang, F.-J. Tsai, C.-H. Lu, C.-H. Yeh, N.-F. Wang, and M.-P. Houng, “Improvement of azo/pa-sic: H contact by the p-μc-si: H insertion layer and its application to a-si: H solar cells,” *Solid-state electronics*, vol. 72, pp. 48–51, 2012.

[45] H. Tan, P. Babal, M. Zeman, and A. H. Smets, “Wide bandgap p-type nanocrystalline silicon oxide as window layer for high performance thin-film silicon multi-junction solar cells,” *Solar Energy Materials and Solar Cells*, vol. 132, pp. 597–605, 2015.

[46] A. H. Smets, M. A. Wank, B. Vet, *et al.*, “The relation between the bandgap and the anisotropic nature of hydrogenated amorphous silicon,” *IEEE Journal of Photovoltaics*, vol. 2, no. 2, pp. 94–98, 2012.

[47] B. Rech, C. Beneking, and H. Wagner, “Improvement in stabilized efficiency of a-si: H solar cells through optimized p/i-interface layers,” *Solar Energy Materials and Solar Cells*, vol. 41, pp. 475–483, 1996.

[48] A. Belfar and H. Ait-Kaci, “Effect of incorporating p-type hydrogenated nanocrystalline silicon buffer layer on amorphous silicon n–i–p solar cell performances,” *Thin Solid Films*, vol. 525, pp. 167–171, 2012.

[49] R. Arya, A. Catalano, and R. Oswald, “Amorphous silicon p-i-n solar cells with graded interface,” *Applied physics letters*, vol. 49, no. 17, pp. 1089–1091, 1986.

[50] G. Bugnon, G. Parascandolo, S. Hänni, *et al.*, “Silicon oxide buffer layer at the p–i interface in amorphous and microcrystalline silicon solar cells,” *Solar energy materials and solar cells*, vol. 120, pp. 143–150, 2014.

[51] M. Stuckelberger, B.-S. Park, G. Bugnon, *et al.*, “The boron-tailing myth in hydrogenated amorphous silicon solar cells,” *Applied Physics Letters*, vol. 107, no. 20, 2015.

[52] T. Matsui, T. Fujibayashi, Y. Nasuno, *et al.*, “Impurity diffusion effect on p/i interface properties of pin junction microcrystalline silicon solar cells,” in *3rd World Conference onPhotovoltaic Energy Conversion, 2003. Proceedings of*, IEEE, vol. 2, 2003, pp. 1831–1834.

A

Appendix: LID study of different qualities of a-Si:H absorber layer

A.1. Box plots: 25 °C vs 50 °C

A.1.1. Open circuit voltage

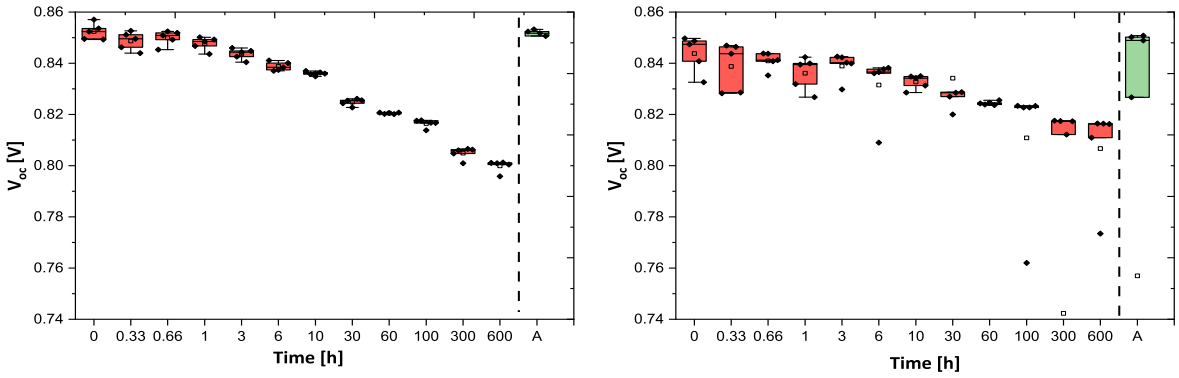

(a) 25 °C **(b)** 50 °C

Figure A.1: Open circuit voltage (V_{oc}) plots of low bandgap a-Si:H sample after light soaking at 25 °C and 50 °C

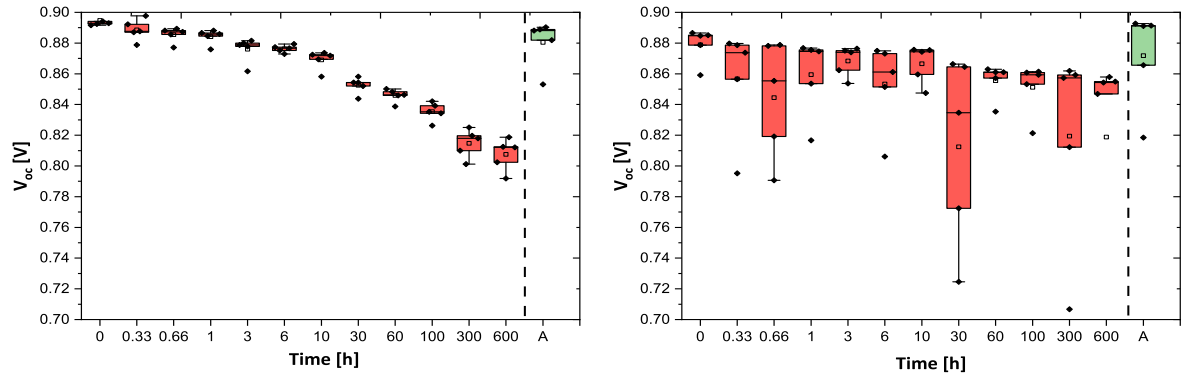

(a) 25 °C **(b)** 50 °C

Figure A.2: Open circuit voltage (V_{oc}) plots of high bandgap a-Si:H sample after light soaking at 25 °C and 50 °C

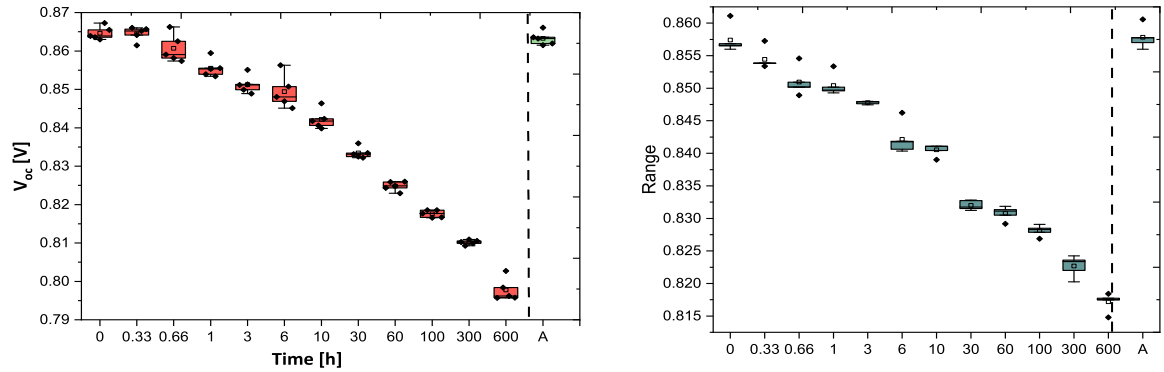

(a) 25 °C **(b)** 50 °C

Figure A.3: Open circuit voltage (V_{oc}) plots of high/low bandgap a-Si:H sample after light soaking at 25 °C and 50 °C

A.1.2. Fill factor

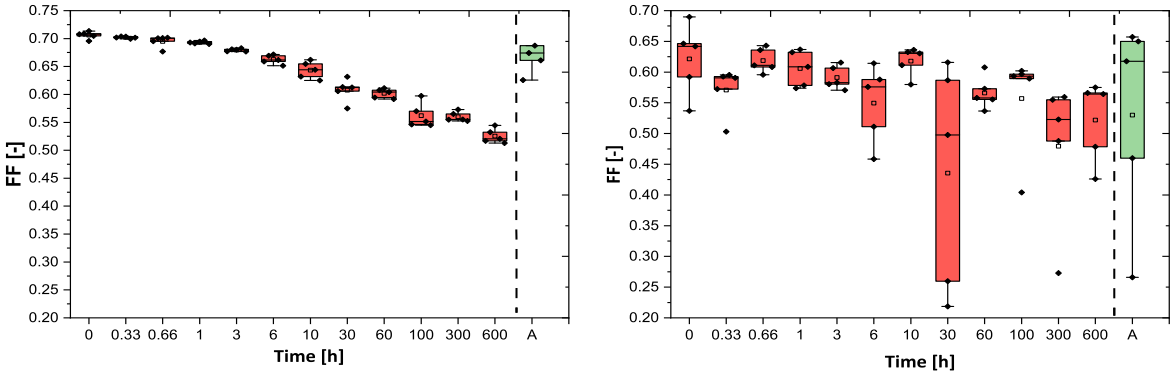

(a) 25 °C **(b)** 50 °C

Figure A.4: Fill factor (FF) plots of low bandgap a-Si:H sample after light soaking at 25 °C and 50 °C

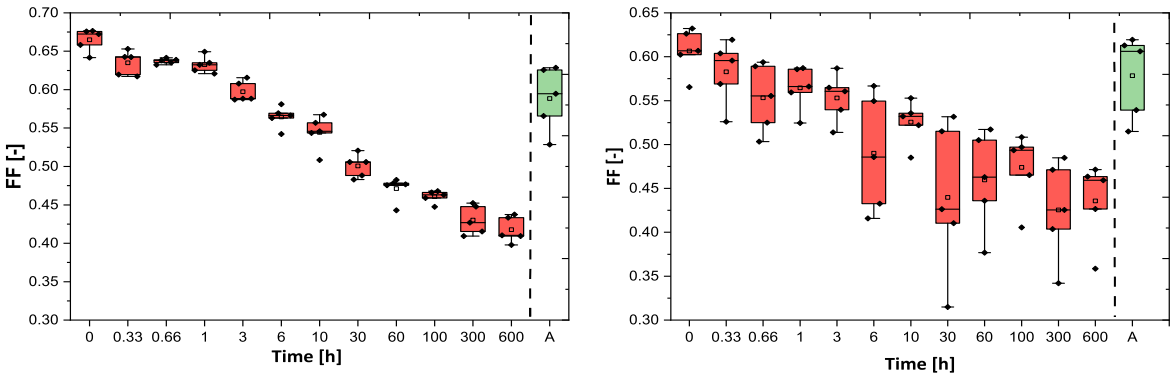

(a) 25 °C **(b)** 50 °C

Figure A.5: Fill factor (FF) plots of high bandgap a-Si:H sample after light soaking at 25 °C and 50 °C

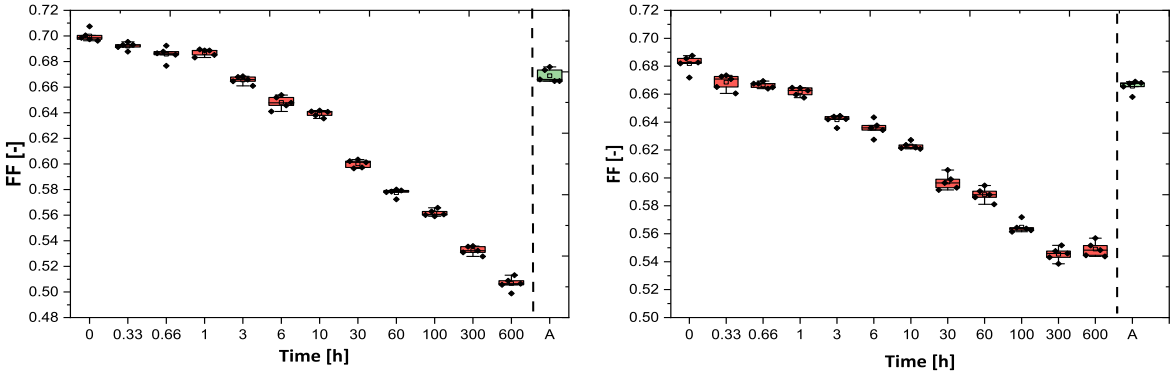

(a) 25 °C **(b)** 50 °C

Figure A.6: Fill factor (FF) plots of high/low bandgap a-Si:H sample after light soaking at 25 °C and 50 °C

A.1.3. Series resistance

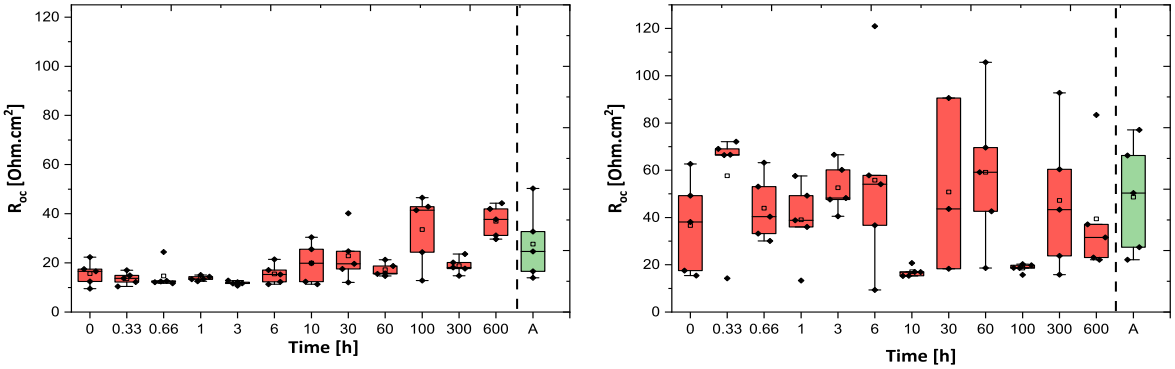

(a) 25 °C **(b)** 50 °C

Figure A.7: Series resistance (R_{oc}) plots of low bandgap a-Si:H sample after light soaking at 25 °C and 50 °C

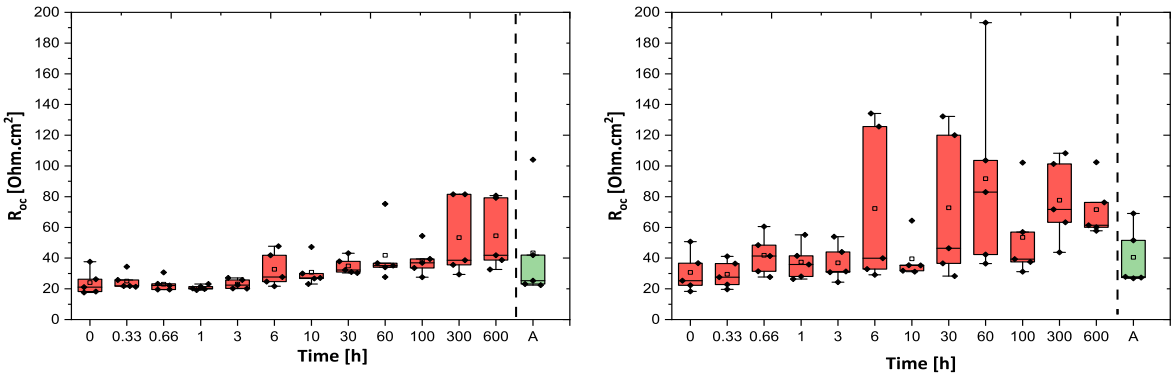

(a) 25 °C **(b)** 50 °C

Figure A.8: Series resistance (R_{oc}) plots of high bandgap a-Si:H sample after light soaking at 25 °C and 50 °C

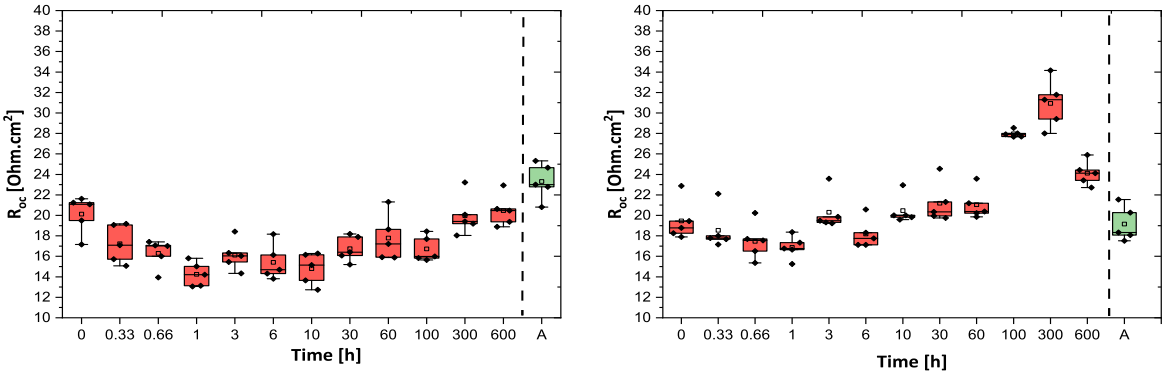

(a) 25 °C **(b)** 50 °C

Figure A.9: Series resistance (R_{oc}) plots of high/low bandgap a-Si:H sample after light soaking at 25 °C and 50 °C

A.1.4. Shunt resistance

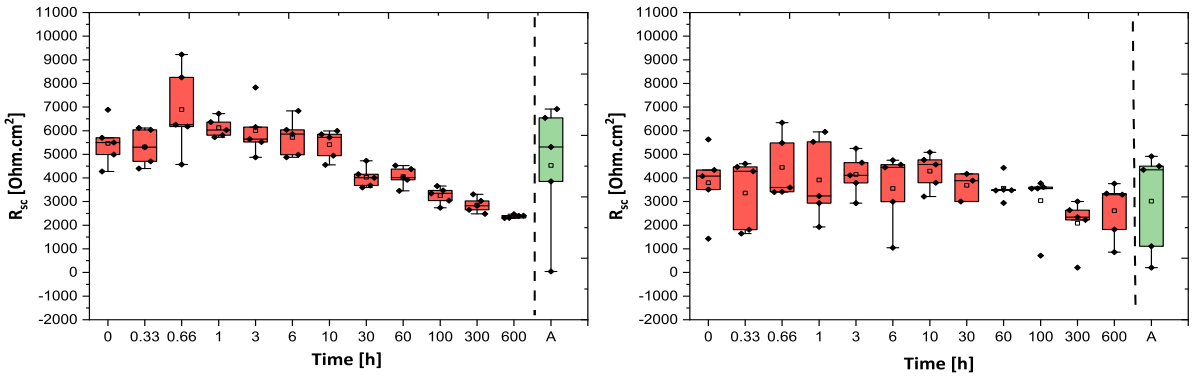

(a) 25 °C **(b)** 50 °C

Figure A.10: Shunt resistance (R_{sc}) plots of low bandgap a-Si:H sample after light soaking at 25 °C and 50 °C

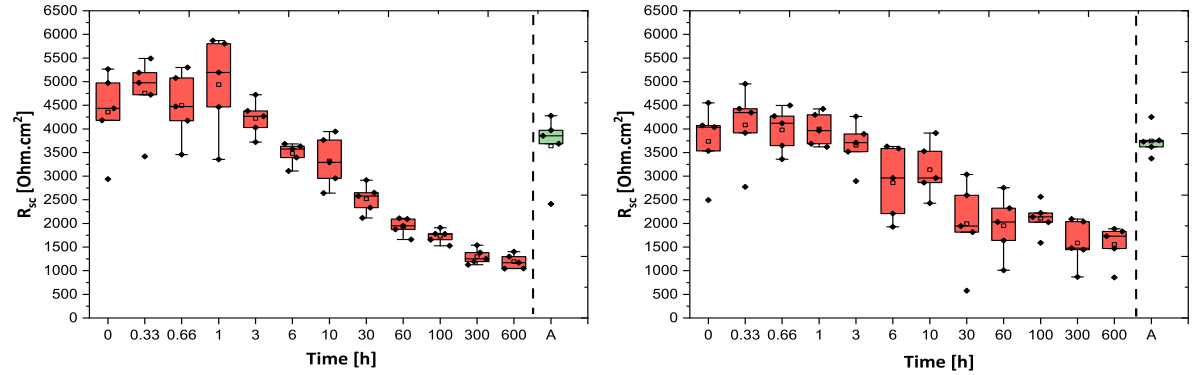

(a) 25 °C **(b)** 50 °C

Figure A.11: Shunt resistance (R_{sc}) plots of high bandgap a-Si:H sample after light soaking at 25 °C and 50 °C

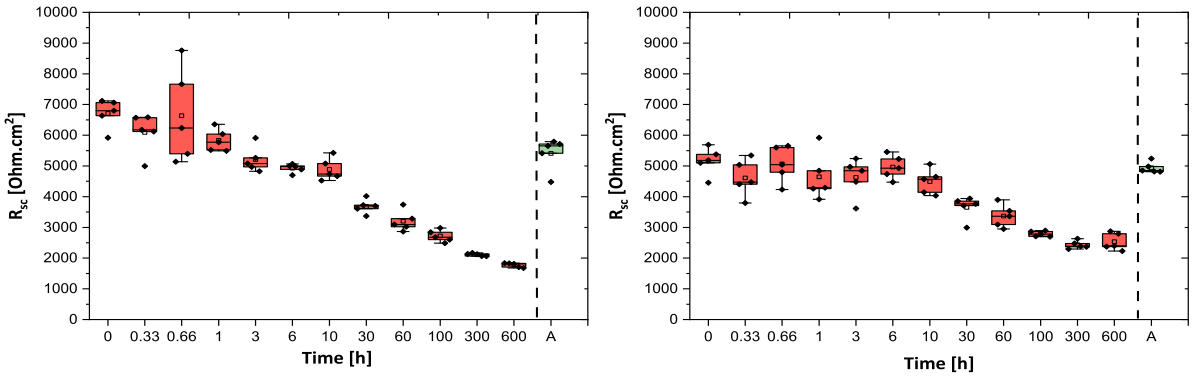

(a) 25 °C

(b) 50 °C

Figure A.12: Shunt resistance (R_{sc}) plots of high/low bandgap a-Si:H sample after light soaking at 25 °C and 50 °C

B

Appendix: The p/i interface degradation study

B.1. Post annealing results

B.1.1. EQE plots: Effects of buffer layer on LID

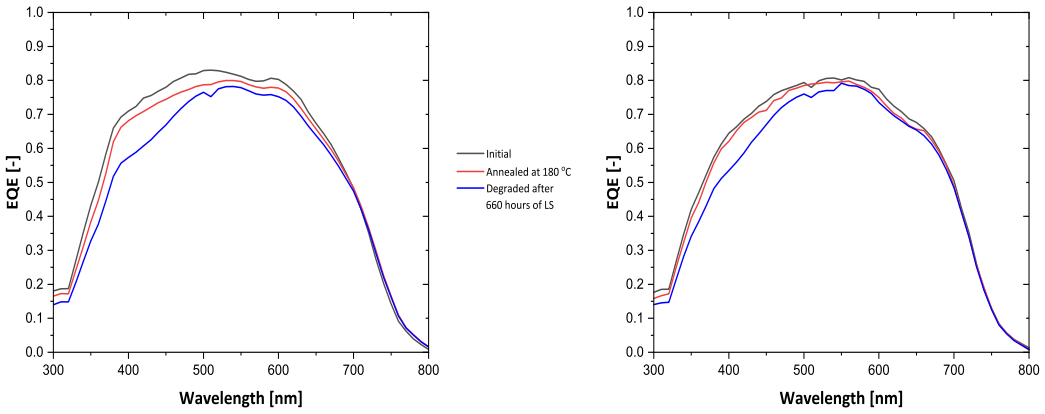

(a) i-SiO$_X$ buffer

(b) i-aSi:H buffer

Figure B.1: EQE plots of single junction a-Si:H samples with iSiOx and i-a-Si:H buffer layers after annealing

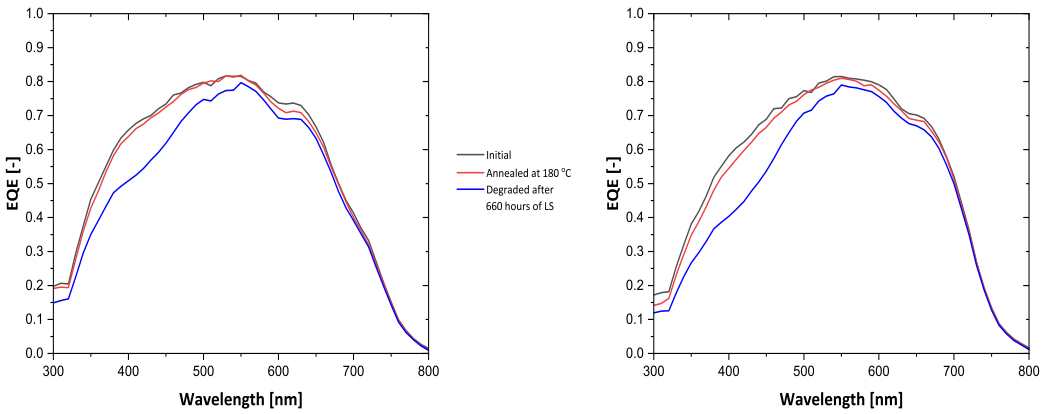

(a) p-aSi:H buffer **(b)** p-ncSi:H buffer

Figure B.2: EQE plots of single junction a-Si:H samples with p-a-Si:H and p-nc-Si:H buffer layers after annealing

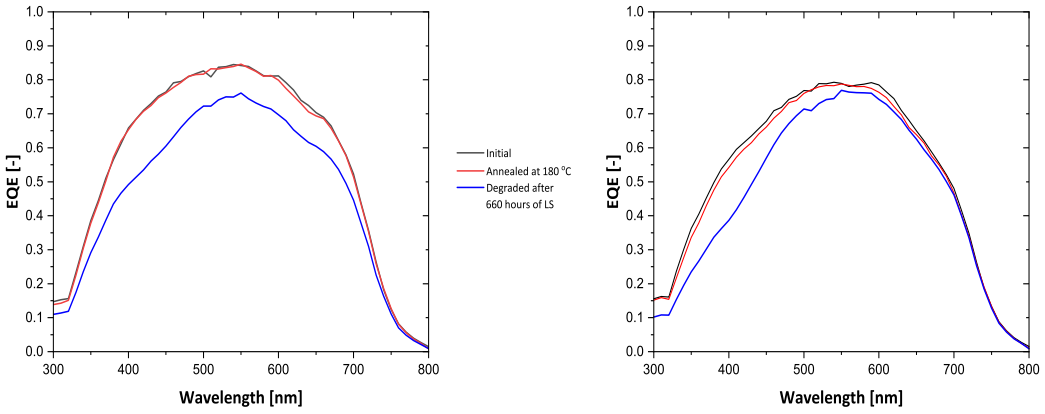

(a) p-ncSiO$_X$:H buffer **(b)** no buffer

Figure B.3: EQE plots of single junction a-Si:H samples with p-ncSiO$_X$:H buffer and no buffer layer after annealing

B.1.2. EQE plots: Effects of window layer (p) doping on LID

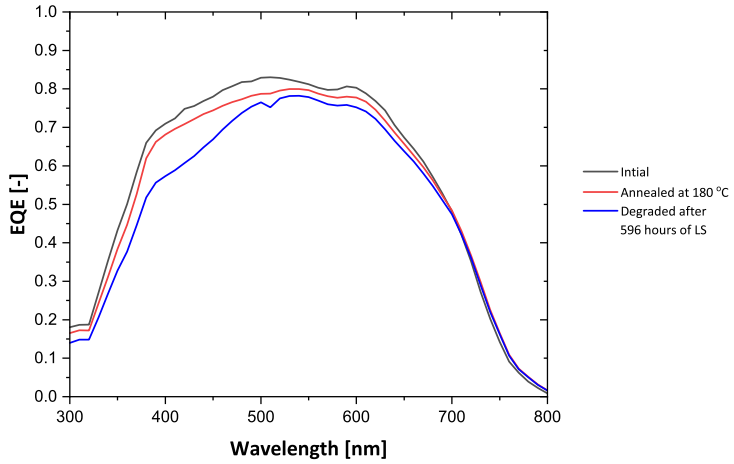

Figure B.4: EQE plots of single junction a-Si:H samples with a window layer B_2H_6 flowrate of 10 sccm after annealing

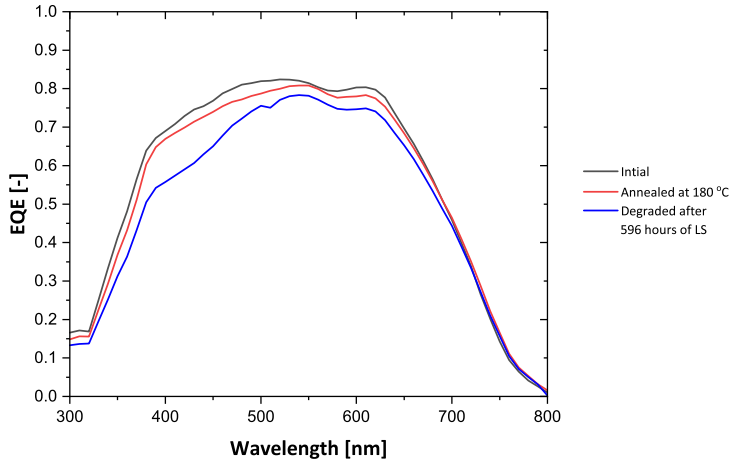

Figure B.5: EQE plots of single junction a-Si:H samples with a window layer B_2H_6 flowrate of 20 sccm after annealing

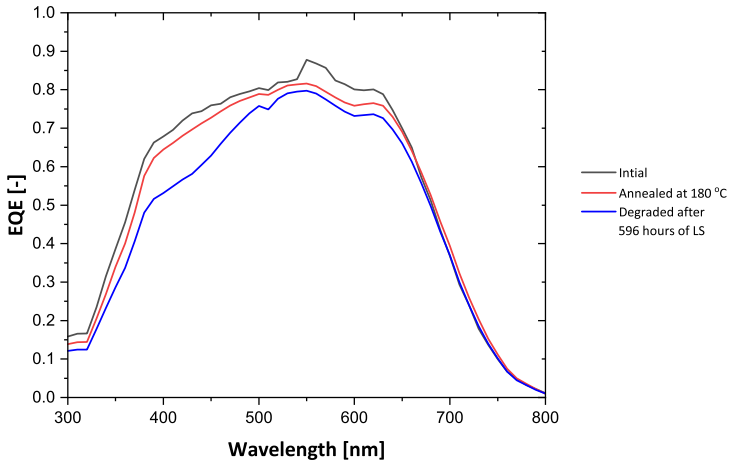

Figure B.6: EQE plots of single junction a-Si:H samples with a window layer B_2H_6 flowrate of 30 sccm after annealing